CZECH TECHNICAL UNIVERSITY IN PRAGUE

Faculty of Nuclear Sciences and Physical Engineering

Department of Physics

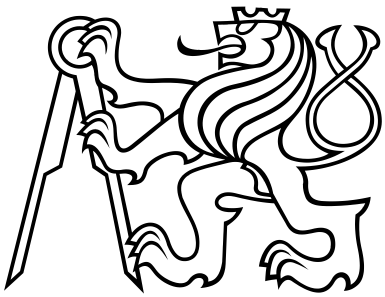

Master's Thesis

Production of J/ψ meson in central U+U collisions at the STAR experiment

Jana Fodorová

Supervisor: RNDr. Petr Chaloupka, Ph.D.

Consultant: Mgr. Jaroslav Bielčík, Ph.D.

Prague, 2016

ČESKÉ VYSOKÉ UČENÍ TECHNICKÉ
V PRAZE
Fakulta jaderná fyzikálně inženýrská
Katedra fyziky

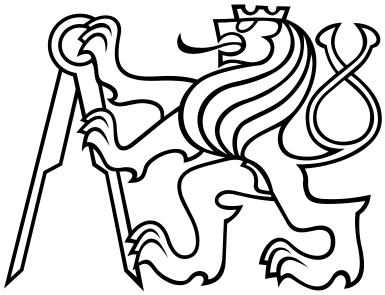

Diplomová práce

Produkce J/ψ v centrálních srážkách U+U na experimentu STAR

Jana Fodorová

Vedoucí práce: RNDr. Petr Chaloupka, Ph.D.

Konzulant: Mgr. Jaroslav Bielčík, Ph.D.

Praha, 2016

Prohlášení:

Prohlašuji, že jsem svou diplomovou práci vypracovala samostatně a použila jsem pouze podklady (literaturu, projekty, software, atd.) uvedené v přiloženém seznamu.

Nemám závažný důvod proti užití tohoto školního díla ve smyslu 60 Zákona č.121/2000 Sb., o právu autorském, o právech souvisejících s právem autorským a o změně některých zákonů (autorský zákon).

V Praze dne

Title:
J/ψ production in central U+U collisions at the STAR experiment

Author: Jana Fodorová

Specialization: Experimental nuclear and particle physics

Sort of project: Master's Thesis

Supervisor: RNDr. Petr Chaloupka, Ph.D.
Consultant: Mgr. Jaroslav Bielčík, Ph.D.

Abstract:

The theory of strong interaction predicts a phase transition at high temperature and energy density from hadronic matter to the state of deconfined quarks and gluons called quark-gluon plasma (QGP). It is expected that heavy-ion collisions at the Relativistic Heavy Ion Collider (RHIC) achieve conditions needed for the QGP formation. The suppression of production of bound states of heavy quarks (c, b) and their antiquarks, heavy quarkonia, due to the color screening of the quark-antiquark potential in the deconfined medium has been proposed as a signature of the QGP. However, other effects such as secondary production in the QGP complicate the suppression picture. In this thesis the analysis of J/ψ production via the di-electron decay channel in 0 - 5 % most central U+U collisions at $\sqrt{s_{\mathrm{NN}}} = 193$ GeV at the STAR experiment at RHIC is described. Preliminary results on invariant yield and nuclear modification factor of J/ψ are presented.

Key words : quark-gluon plasma, heavy-ion collisions, RHIC, heavy quarkonia, J/ψ

Název:

Produkce J/ψ v centrálních srážkách U+U na experimentu STAR

Autor: Jana Fodorová

Obor: Experimentální jadrná a částicová fyzika

Druh práce: Diplomová práce

Vedoucí práce: RNDr. Petr Chaloupka, Ph.D.
Konzultant: Mgr. Jaroslav Bielčík, Ph.D.

Abstrakt:

Podľa teórie silnej interakcie nastáva pri vysokých teplotách a hustotách energie fázový prechod hadrónovej hmoty do stavu asymptoticky voľných kvarkov a gluónov, nazývaného kvarkovo-gluónová plazma (QGP). Predpokladá sa, že pri zrážkach ťažkých jadier na Relativistickom urýchľovači ťažkých iónov (RHIC) sú podmienky potrebné na vytvorenie QGP dosahnuté. Potlačenie producie viazaných stavov ťažkých kvarkov a ich antikvarkov (c, b), ťažkých kvarkóni, v dekonfinovanej hmote je prisudzované efektu farebného tienenia v QGP. Avšak prítomnosť iných efektov, napríklad sekundárnej produkcie kvarkóni QGP, komplikuje obraz o potlačení. V tejto práci popisujeme analýzu produkcie J/ψ z dielektrónového rozpadového kanálu v 0-5% najcentrálnejších zrážkach jadier uránu pri energii $\sqrt{s_{\mathrm{NN}}} = 193$ GeV na experimente STAR na RHICu. Prezentujeme predbežné výsledky invariantného výťažku a jadrového modifikačného faktoru J/ψ.

Klíčová slova : kvarkovo-gluónová plazma, zrážky ťažkých jadier, RHIC, ťažké kvarkóniá, J/ψ

Acknowledgement

I would like to give thanks to RNDr. Petr Chaloupka, Ph.D. for his support, patience, professional help and friendliness. I would also like to thank Mgr. Jaroslav Bielčík, Ph.D. for his good advice, encouragment and interest in my work. Last, but not least, I want to thank my boyfriend, family and friends - they were there for me when I needed them.

Contents

List of Figures

List of Tables

Preface

In 2000 the Relativistic Heavy Ion Collider (RHIC) in Brookhaven National Laboratory began a new era of heavy-ion physics. For the first time, collisions of heavy ions at high energies enabled to study the nuclear matter at extreme conditions. Already the data from the first years of RHIC operation indicated the presence of a novel state of hot and dense matter, the quark-gluon plasma (QGP), during the evolution of the heavy-ion collision. The aim of the physics is to prove the existence of this phase of deconfined quarks and gluons and to study its properties. Different probes which may refer to the presence of the QGP have been suggested, e.g. collective flow, jet quenching or suppression of heavy quarkonium production. The last mentioned is the main object of this thesis.

Heavy quarkonia, bound states of heavy quarks and their antiquarks, have been proposed to be suppressed due to the screening of the quark-antiquark potential in the deconfined medium. However, different other effects may influence the observed quarkonium yields, such as cold nuclear matter effects, feed down effects or secondary production via coalescence of charm quarks. To understand these different mechanisms it is important to study the heavy quarkonium production in different collision systems, at different energies and centralities.

The physics of heavy-ion collisions and experimental probes of the presence of the QGP are briefly introduced in Chapter 1. It deals in more detail with the topic of heavy quarkonia, mainly J/ψ meson. Different mechanisms which may affect heavy quarkonium production in heavy-ion but also in proton+nucleus collisions are discussed and recent results on heavy quarkonium measurements at RHIC are presented.

The STAR experiment at RHIC is one of the foremost experiments in the study of the medium created in heavy-ion collisions. It consists of different subsystems, each of which performs a specific task. The Time Projection Chamber is used for tracking and particle identification, the Time Of Flight detector is used for triggering. Moreover, it improves the particle identification capabilties of TPC by measuring the time-of-flight of particles. The Barrel Electromagnetic Calorimeter measures the electromagnetic showers of high-p_{T} particles. Its fast response allows to trigger on high-p_{T} electrons. For the heavy quarkonium studies the recently installed Heavy Flavor Tracker and Muon Telescope Detector are important. All of the subsystems are described in more detail in Chapter 2.

The next four chapters describe the analysis of the author of this thesis, i.e. the analysis of J/ψ meson in central U+U collisions at $\sqrt{s_{\mathrm{NN}}} = 193$ GeV at mid-rapidity at the STAR experiment. J/ψ signal is reconstructed via the di-electron decay channel. The

selection of events, J/ψ daughter electrons and, finally, the extraction of J/ψ raw yield is described in Chapter 3.

Chapter 4 describes different corrections applied on J/ψ raw signal based on the calculation of detection and identification efficiency of J/ψ daughter electrons either from real or from simulated data.

Systematic uncertainties coming from J/ψ raw yield extraction and efficiency calculation are described and discussed in Chapter 5.

Finally, the main results of this work, J/ψ invariant yield and nuclear modification factor in central U+U collisions, are presented in Chapter 6.

Chapter 1

Heavy quarkonia in heavy-ion collisions

One of the most important and "always up-to-date" challenges of physics is the understanding of the laws of the world and the Universe and finding out what it consists of. In a more fundamental sense, the basis of this study is the determination what the elementary building blocks of matter are and how they interact with each other.

A very successful theory in this field is the Standard Model of particle physics developed during the second half of the 20th century. It is a quantum field theory concerning the electromagnetic, weak and strong interactions, as well as elementary particles classified into quarks (u, d, s, c, b, t), leptons $(e, \nu_{\mathrm{e}}, \mu, \nu_{\mu}, \tau, \nu_{\tau})$ and bosons $(\gamma, W, Z$, gluons and Higgs boson).

The strong interaction is responsible for binding quarks and gluons into hadrons (protons, neutrons) and, on a larger scale, protons and neutrons into nuclei. The theory of Quantum Chromodynamics (QCD) is used to describe the strong force between quarks (antiquarks) mediated by gluons. In this theory each quark (antiquark) carries one of three color charges: red, green, blue (antired, antigreen, antiblue). Quarks bind through the strong interaction to form color-neutral bound states, the already mentioned hadrons. Hadrons are known as mesons if they are made up of a quark of some color and an antiquark with corresponding anticolor, or as baryons if they are formed from three quarks or antiquarks with all three colors or anticolors.

The QCD coupling constant α_{s} which determines the strength of the strong interaction is proportional to [1]

$$\alpha_{\mathrm{s}}(Q^2) \sim \frac{1}{ln(\frac{Q^2}{\Lambda^2_{\mathrm{QCD}}})} \tag{1.1}$$

where Λ_{QCD} is the QCD scale and Q denotes the momentum transfer in the interaction. The summary of α_{s} measurements as a function of Q can be seen in Figure 1.1. At low Q^2 the coupling constant α_{s} is large and the QCD potential can be approximated by [2]

$$V(r) \approx kr \tag{1.2}$$

where k is constant called string tension. Hence the attractive force between quark and

antiquark increases with distance r. This is a major difference compared with electromagnetic interaction which follows an opposite trend.

When the QCD potential is high enough the string breaks and a new quark-antiquark pair is created out of the vacuum. Accordingly, it is not possible to observe free quark or gluon, free color charge. This characteristic feature of the QCD is called color confinement.

On the other hand, with increasing Q^2 and decreasing the interaction distance α_s decreases. Under extreme conditions, at asymptotically small distances or high Q^2 α_s gets very small and quarks can be treated as free particles. This phenomenon is called asymptotic freedom.

The phase of matter consisting of asymptotically free quarks and gluons is called quark-gluon plasma (QGP). It is believed that the Universe was in this state for about few milliseconds after the Big Bang. Currently, there is a large experimental effort to create the QGP and to study its properties. At present, the only way of testing it, is in heavy-ion collisions.

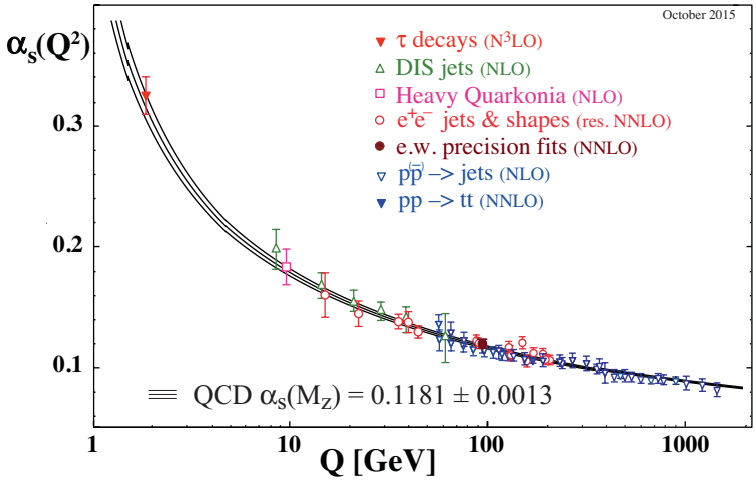

Figure 1.1: Summary of measurements of α_s as a function of the energy scale Q. The respective degree of QCD perturbation theory used in the extraction of α_s is indicated in brackets [3].

1.1 Quark-gluon plasma and heavy-ion collisions

High temperatures and energy densities reached in ultrarelativistic heavy-ion collisions allow to study properties of the nuclear matter at such extreme conditions that the transition of hadronic nuclear matter into the state of asymptotically free quarks and gluons takes part.

Currently, the main goal of colliding ultrarelativistic heavy ions is to precisely study the transition of the hadronic matter into the state of deconfined quarks and gluons as well as properties of the medium formed in the collisions.

1.1.1 Phase diagram of the QCD matter

Figure 1.2 shows the schematic drawing of our current knowledge and theoretical expectations about the the phase diagram of the nuclear matter. It is described by the temperature T and the baryon chemical potential μ_{B}. The baryon chemical potential is the measure of the net baryon density defined as the difference between the density of baryons and anti-baryons. In the early Universe, there was equality between the matter and antimatter resulting in $\mu_{\mathrm{B}} = 0$. In normal nuclear matter there is no much antimatter around and thus the baryon chemical potential $\mu_B \sim 900$ MeV reflects the density of baryons (protons and neutrons). The range of temperature and the baryon chemical potential in which the matter is in the form confined hadron gas is shown in the lower left part of the phase diagram. By increasing the temperature or baryon chemical potential the confinement breaks down. The deconfinement at high μ_{B} is expected to occur in neutron stars where the density in the core can be up-to 10-times larger than the normal nuclear density [4]. The deconfinement at high T can be achieved in ultrarelativistic heavy-ion collisions such as those at RHIC or at the Large Hadron Collider (LHC).

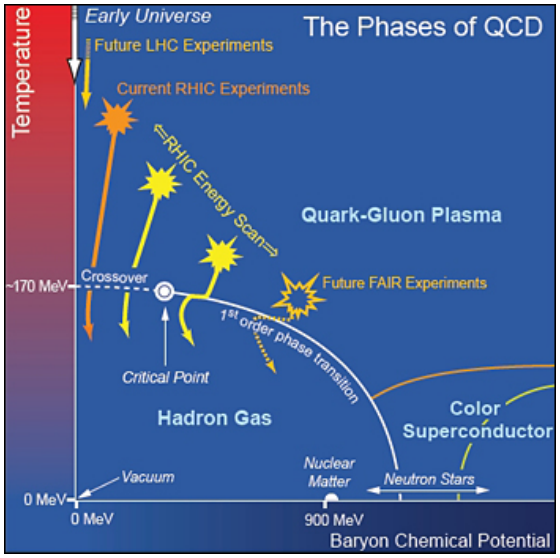

Figure 1.2: The phase diagram of the nuclear matter [5].

The character of the transition between the hadron gas and the deconfined matter is still not explored in detail. Current knowledge suggests that for zero and low μ_{B} the transition is crossover (continual change of the phase) at the critical temperature $T_{\mathrm{C}} \sim 170$ MeV. For higher μ_{B} and lower T it has a nature of the first order phase transition (accompanied by the discontinuity of the first derivative of the free energy). The point where the first order phase transition begins is called critical point. However, the locations of the critical point and the phase boundary remain to be determined experimentally. Proving their existence would be a strong confirmation of our understanding of nuclear matter at extreme conditions. The Beam Energy Scan (BES) program at RHIC [6] is dedicated for the study of the QCD phase diagram, possible QCD phase boundary and QCD critical point.

1.1.2 Space-time evolution of the heavy-ion collision

Nucleus-nucleus collisions have long been the object of study of many physicists, however, even today it is not known exactly how the ultrarelativistic heavy-ion collision occurs. Here, the possible scenario of the heavy-ion collision is briefly described (see Figure 1.3 where also the evolution without the QGP phase is illustrated).

The medium produced in heavy-ion collisions evolves within the proper time range $\tau \sim 10 - 100$ fm/c [7].

Immediately after the collision nuclei traverse each other depositing a large amount of energy in the medium in the form of excited virtual quanta. As a result of their deexcitation quarks and gluons are created and interact with each other.

As the system reaches the thermal equilibrium it can be described by the laws of hydrodynamics. From this moment it is in the quark-gluon plasma phase. The proper time of the system when it enters this phase is estimated to be $\tau_0 \leq 1$ fm/c [7]. The system expands and cools down. When the critical temperature $T_c \simeq 170$ MeV [7] is reached, quarks and gluons can no longer be free within the system and are confined into hadrons. However, it is not clear if the phase transition into the hadron gas happens immediately or if it is proceeded by the mixed phase of quarks, gluons and hadrons.

As the system is in the phase of hadron gas, it cools down and expands until the chemical freeze-out begins.

During the chemical freeze-out inelastic scatterings between the hadrons disappear and the particle identities are set. However, hadrons can still interact elastically. Elastic collisions disappear at thermal freeze-out. At the end, hadrons fly out to the detector.

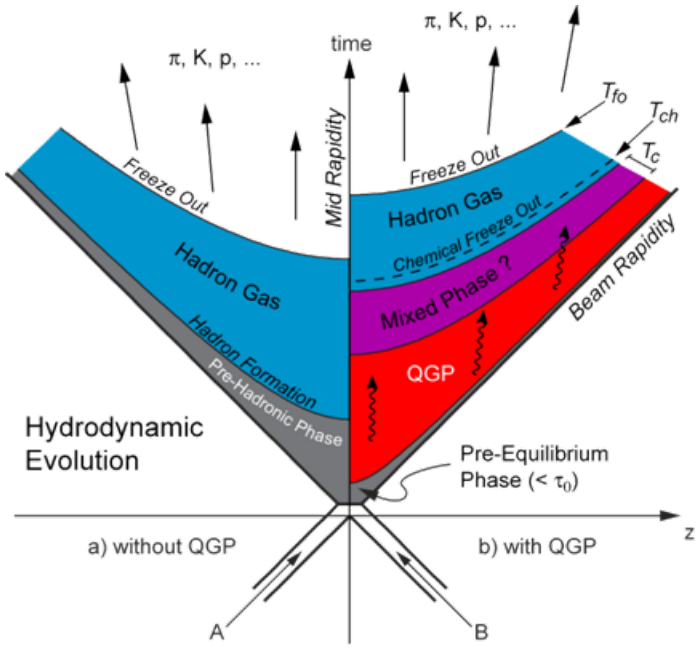

Figure 1.3: Two scenarios of the evolution of the relativistic collision – without and with the presence of the QGP phase [8].

1.1.3 Centrality of the collision

As in every experiment the initial conditions are very important. This applies particularly for collisions of heavy nuclei. They can be classified according to different criteria, such as the size and type of colliding nuclei or the energy of the collision. In order to study effects of the medium created in the ultrarelativistic collisions of heavy-nuclei it is useful to sort collisions according to the size of the overlapping area of the colliding nuclei. As the overlap is larger, there are more nucleons which can participate in interactions thus the energy density of the medium can be higher. This can turn into higher probability of the QGP formation.

Based on the size of the overlapping area the collisions of heavy nuclei can be divided into central, peripheral or ultra-peripheral. The size of the overlap is related to the perpendicular distance between the centers of the nuclei called impact parameter b, see Figure 1.4 for identical nuclei.

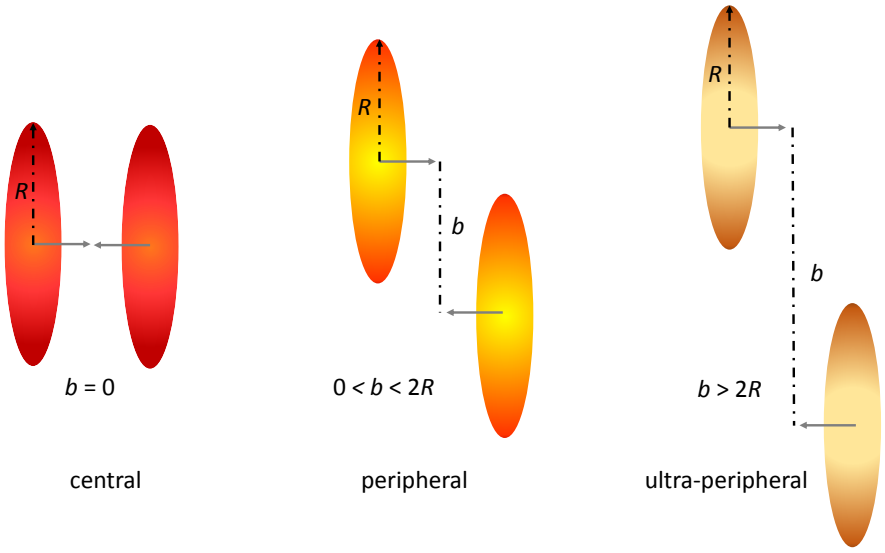

Figure 1.4: Central, peripheral and ultra-peripheral collision.

However, the impact parameter b cannot be measured directly and in collisions of deformed nuclei, in which colliding nuclei can have different orientations and thus different sizes of the overlapping area at the same b, it provides insufficient information about the collisional geometry.

There are two experimental ways which are often used to measure the collisional centrality. The centrality can be determined by measuring the spectators − nucleons which do not participate in interactions. At the STAR experiment, they are measured by the so called Zero Degree Calorimeters (see Section 2.6). One could expect that as the number of spectators decreases the centrality increases. However, not only for the most central but also for the most peripheral collisions the number of spectators is ~ 0 since nucleons of the colliding nuclei are not kicked out of the nuclei and, therefore, not measured by ZDCs. Moreover, different orientations of the deformed nuclei at the same impact parameter can turn into different number of measured spectators. Therefore, this method of centrality

definition is not unambiguous. Another way of accessing the information abot centrality of the collision is by the track multiplicity measurements − more central collisions mean more nucleons participating in the collision which turn to higher multiplicity − more tracks observed in the detector. Figure 1.5 shows the dependence of the charged particle multiplicity N_{ch} distribution on the number of particles participating in the collision N_{part} and the impact parameter b.

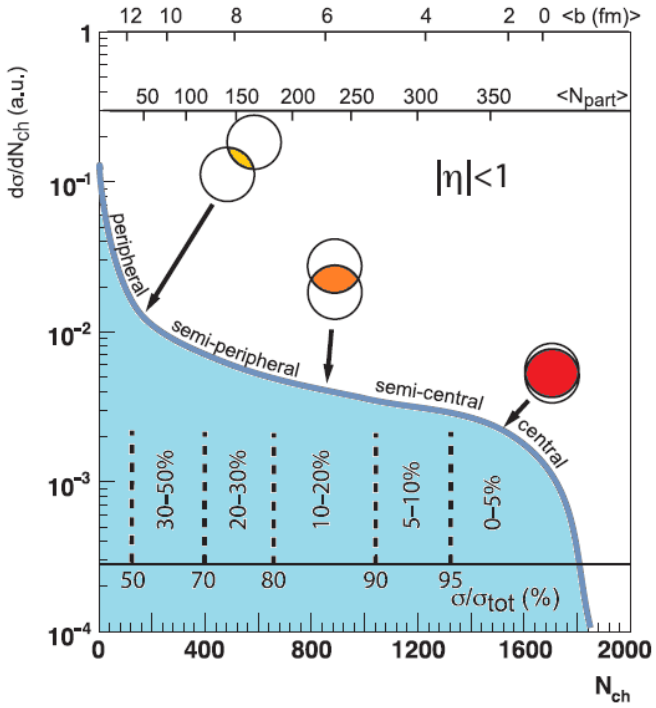

Figure 1.5: Relation between the charged particle multiplicity N_{ch} distribution, the average number of particles participating in the collision $< N_{\mathrm{part}} >$ and the impact parameter b [9].

1.1.4 U+U Collisions

Collisions of deformed nuclei provide an opportunity to study the spatial dependence of various properties and effects of the created. Within the same colliding system, deformed nuclei can have different spatial orientations and, therefore, allow wider variations of energy density of the created medium.

Upper part of Figure 1.6 shows different configurations of deformed prolate nuclei in the collision. In case of "tip+tip"(left) configurations, the major axes of the nuclei are parallel to the beam axis. Consequently, the largest path lengths through the matter and the highest energy densities can be reached. On the other hand, "side+side"(middle) configurations where the minor axes are parallel to the beam provide the shortest paths through the matter. This is illustrated in the lower part of Figure 1.6. It shows theoretical prediction for the density profiles of nucleons participating in collisions of asymmetric U nuclei [10] related to the configurations above. The right panel of Figure 1.6 shows the

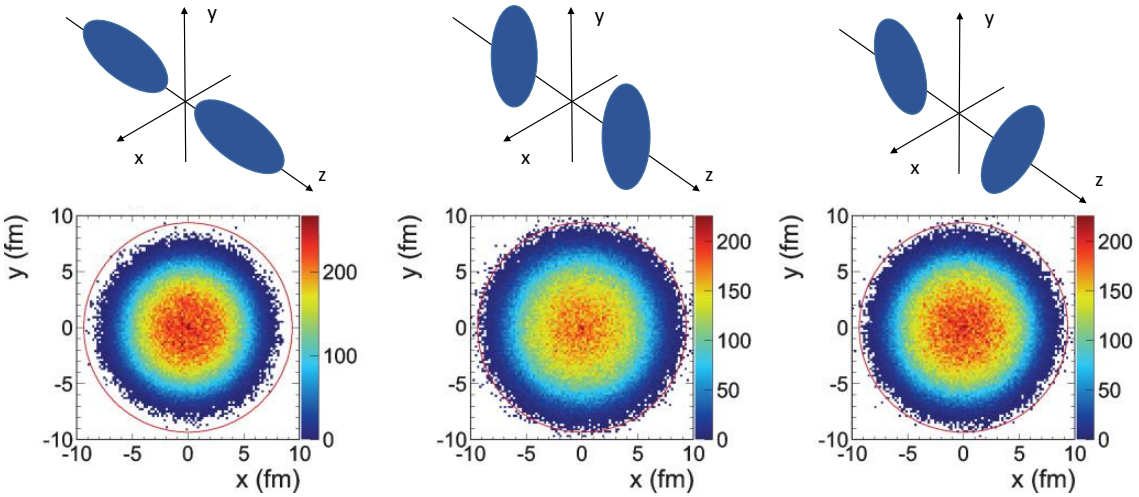

Figure 1.6: Up: Different configurations of collisions of prolate nuclei: tip+tip (left), side+side (middle), random configuration (right). Down: Theoretical prediction for the density profiles of participants in tip+tip (left), side+side (middle), orientation-averaged (right) U+U collisions [10].

orientation-averaged density profile.

The study of deformed nuclei is supported by theoretical expectations of higher energy density reached compared with collisions of spherical nuclei, namely in the case of U+U compared with Pb+Pb collisions [11] and Au+Au collisions [10].

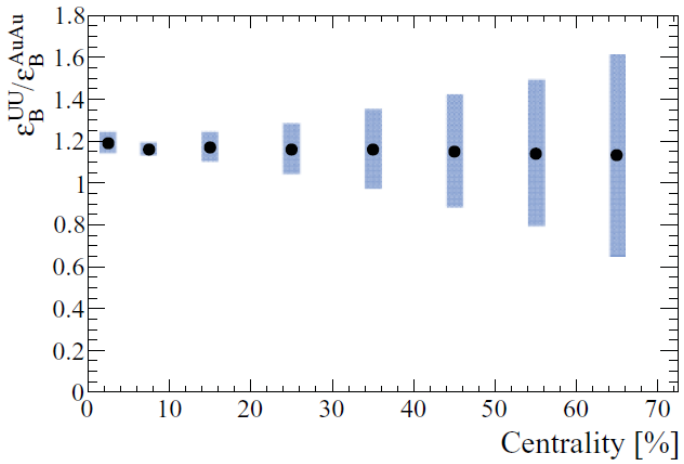

Figure 1.7: Ratio of expected energy density reached in U+U and Au+Au collisions ${\epsilon_B}^{UU}/{\epsilon_B}^{AuAu}$ as a function of centrality [10].

In 2012 prolate U nuclei were collided at RHIC at $\sqrt{s_{NN}} = 193$ GeV. Compared with symmetric Au nuclei being colided at RHIC, the orientation-averaged energy density reached in U+U collisions is expected to be up to 20% higher and for "tip+tip" configurations even more, up to 30% [10]. This is illustrated in the Figure 1.7 which shows the ratio of estimated energy densities in U+U and Au+Au collisions as a function of central-

ity. In the most central U+U collisions, the increase of the energy density is the highest hence in these collisions the most significant effects of the hot medium are expected to be present. Therefore, detailed study of the most central U+U collisions can provide a valuable information about the QGP.

1.1.5 Tools for the QGP studies

Since the QGP cannot be measured directly we have to rely on different observables which may refer to the evidence of the deconfined phase in the evolution of the collision. In this section we turn our attention to probes and observables often considered in the studies of the quark-gluon plasma.

Anisotropic flow

The anisotropic flow is an important probe of the earliest stages of the collision. In non-central collisions the colliding nuclei do not overlap completely, the spatial distributions of participating nucleons forms an almond shape. As the system is thermalized the non-isotropic pressure gradients in the medium lead to different expansion of the volume and, as a result, to the non-isotropic momentum distribution of the final-state particles. The pressure is largest along the reaction plane resulting in a boost in momentum of particles in this direction.

The momentum anisotropy can be determined by performing a Fourier decomposition of the measured momentum distribution of particles

$$E\frac{d^3N}{d^3p} = \frac{d^2N}{2\pi p_T dp_T dy}\left(1 + \sum_{n=1}^{\inf} 2v_n\left(p_T, y\right) cos\left[n\left(\phi - \psi_r\right)\right]\right), \tag{1.3}$$

where ϕ is the azimuthal angle and ψ_r is the raction plane angle (see Figure 1.8). Coefficients v_n can be expressed as

$$v_n\left(p_T, y\right) = \langle cos\left[n\left(\phi - \psi_r\right)\right]\rangle. \tag{1.4}$$

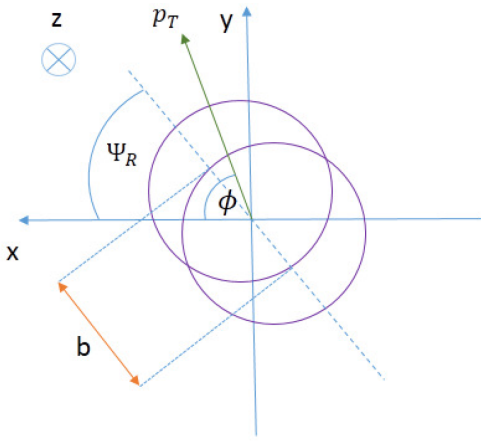

Figure 1.8: Reaction plane and the coordinate system.

The second harmonic coefficient v_2 is known as elliptic flow. It is developed in the early stages of the collision where the pressure gradients are the largest. Hence, v_2 is sensitive to the dynamics of the early collision system and the degree of thermalization of the medium.

The large value of the elliptic flow indicates the presence of the strongly interacting matter in the collision [12]. Figure 1.9 shows results on v_2 of identified hadrons in 200 GeV Au+Au collisions at different collision centralities. v_2 increases towards more peripheral collisions and towards higher p_{T}. Data also show the mass ordering – the heavier the hadron the smaller v_2 and for higher p_{T} they show higher v_2 for mesons than for baryons which is typical for hydrodynamic evolution [13].

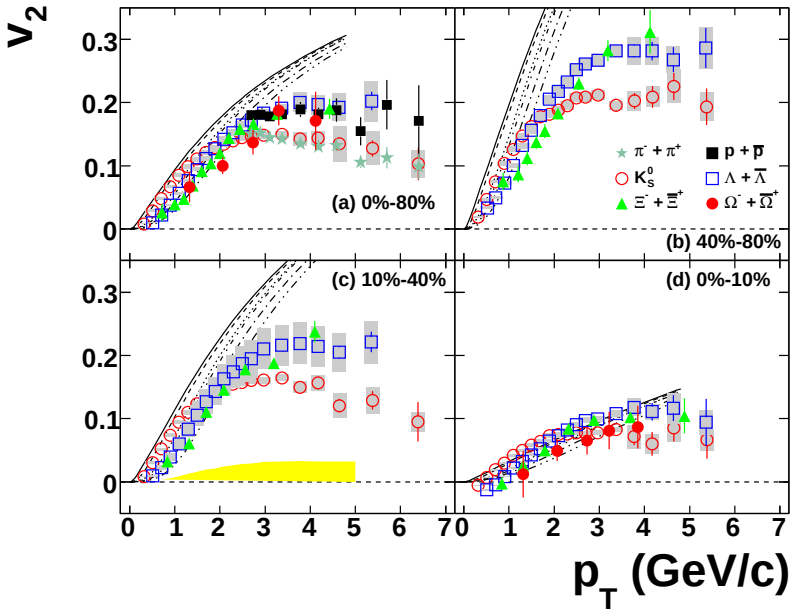

Figure 1.9: v_2 of K^0_{s} (open circles), Λ (open squares), Ξ (filled triangles) and Ω (filled circles) as a function of p_{T} for 0 - 80 %, 40 - 80 %, 10 - 40 % and 0 - 10 % Au+Au collisions at $\sqrt{s_{\mathrm{NN}}} = 200$ GeV at STAR. Compared with results from ideal hydrodynamic calculations [13].

Hard probes

High-p_{T} partons are expected to originate from initial hard scattering processes between nucleons participating in the collision. Due to the high p_{T} of the initial partons, they are able to pull new pairs of quarks and antiquarks out of the vacuum to form hadrons which are highly colinear. Such fragmentations of hard partons in a spray of correlated hadrons are known as jets, see left panel of Figure 1.10. Thus, jets are proxies of high-p_{T} partons.

As high-p_{T} partons traverse the QGP medium they suffer energy loss from elastic

parton scatterings and, more significantly, gluon radiation. This results in softening and broadening of the observed jet structure, known as jet quenching [14]. When two high-p_{T} partons scatter near the boundary of the QGP, one parton can immediately hadronize in the vacuum to form a jet whereas the other parton must traverse the QGP, losing energy in the process and leading to a jet-energy imbalance, see right panel of Figure 1.10.

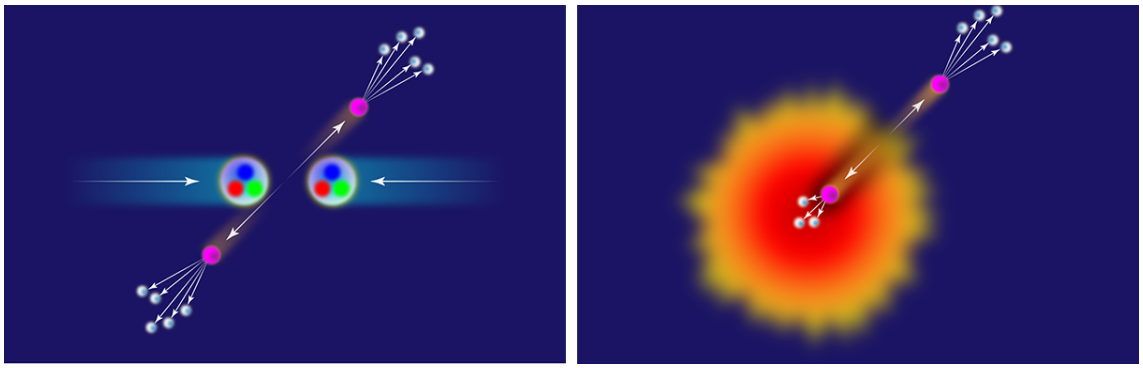

Figure 1.10: Illustration of jets in elementary (left) and A+A (right) collisions where the QGP presence is expected [15].

There are two main experimental observations which support the jet quenching in the QGP: results on nuclear modification factor (see next Section) and correlated di-hadron distributions.

Figure 1.11 shows the di-hadron azimuthal distribution as a function of $\Delta\phi = \phi_{\mathrm{trig}} - \phi_{asoc}$ denoting the azimuthal angle between the triggered high-p_{T} (4 GeV/c < p_{T}(trig.) < 6 GeV/c) hadron and the assocciated hadron (2 GeV/c < p_{T} (asoc.) < p_{T}(trig.)) [16]. As can be seen, in p+p and d+Au similar distribution with near-side peak from jet fragmentation pairs at $\Delta\phi \approx 0$ and away-side peak from back-to-back pairs at $\Delta\phi \approx \pi$ can be seen. A slight broadening of the away-side peak observed in d+Au collisions is probably caused by the Cronin Effect (see Section 1.2.3). On the other hand, in Au+Au collisions the back-to-back peak is not observed - this is consistent with the scenario of jet quenching or, in other words, energy loss of hard partons traversing the strongly interacting medium.

Nuclear modification factor

Nuclear modification factor R_{AB} compares experimental observables such as particle yields in collision systems A+B N_{AB} with respect to the reference p+p measurements σ_{pp}. Expressed as the function of p_{T} and rapidity y it can be defined as

$$R_{\mathrm{AB}}(p_{\mathrm{T}}, y) = \frac{1}{T_{\mathrm{AB}}} \frac{d^2 N_{\mathrm{AA}}/dp_{\mathrm{T}}dy}{d^2\sigma_{\mathrm{pp}}/dp_{\mathrm{T}}dy} \tag{1.5}$$

where T_{AB} is the nuclear overlap function given as the ratio of the average number of binary nucleon+nucleon collisions $< N_{\mathrm{bin}} >$ and the inelastic p+p cross section $\sigma^{\mathrm{pp}}_{\mathrm{inel}}$.

With no medium effects the particle yield in A+B heavy ion collisions should scale with the number of elementary binary collisions and resulting R_{AB} should be equal to unity. As it turns out the medium produced in heavy ion collisions can modify this scaling resulting in the effect of suppression $R_{\mathrm{AB}} < 1$ or enhancement $R_{\mathrm{AB}} > 1$ of the production.

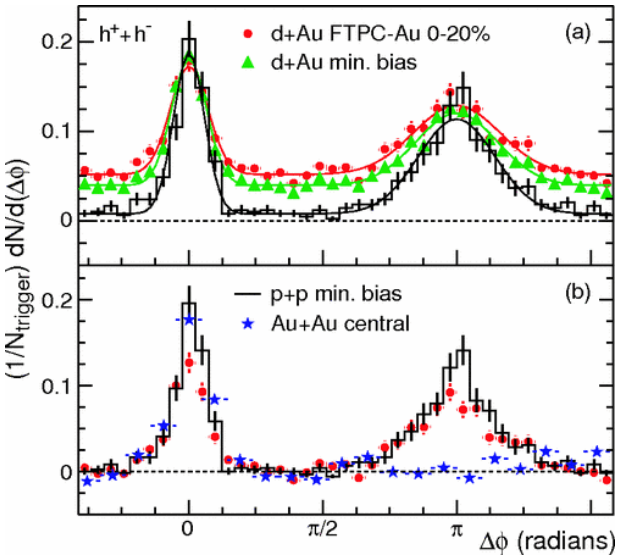

Figure 1.11: Upper panel: Two-particle azimuthal distributions for minimum bias and 0–20% most central d+Au and p+p collisions at STAR [16]. Lower panel: Comparison of two-particle azimuthal distributions for central d+Au collisions compared with p+p collisions and central Au+Au collisions [16].

Figure 1.12 shows the R_{AB} for inclusive spectra of charged hadrons as a function of p_{T} in minimum bias d+Au and central d+Au and Au+Au collisions at RHIC. d+Au data show modification towards higher $R_{\mathrm{AB}} > 1$ at mid p_{T} probably due to the presence of the nuclear matter in the collision (Cronin effect). Data from Au+Au show strong suppression towards higher p_{T} which is expected to be caused due to the interactions with the dense system generated in the collision.

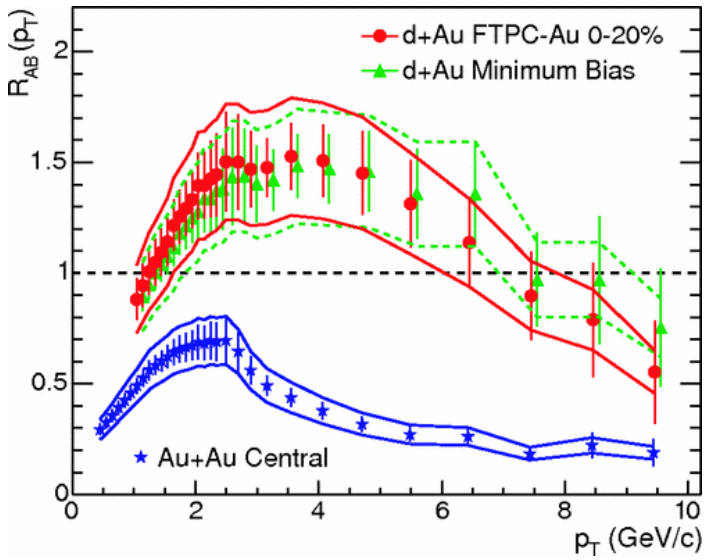

Figure 1.12: R_{AB} as a function of p_{T} for minimum bias d+Au and central d+Au and Au+Au collisions [16].

Heavy quarks

Due to their large masses heavy quarks (c, b) are produced in the initial hard interactions of partons in the earliest stages of the collisions. Since they experience the whole evolution of the system the information about the heavy quark production, its modification and collective flow can provide an insight into the thermodynamic properties and dynamics of the hot medium.

Heavy quarks can be investigated via heavy quarkonia (discussed in more detail in the following section) or open heavy flavor mesons (presented below).

At STAR, there are two main experimental ways how to study open heavy flavor mesons, i.e. mesons composed from single heavy quark and a light antiquark or vice-versa - via the direct reconstruction from hadronic decays or through the non-photonic electrons from semileptonic decays.

Left panel of Figure 1.13 shows preliminary nuclear modification factor of open charm D^0 mesons as a function of p_{T} measured at STAR in central 200 GeV Au+Au collisions compared with D mesons at LHC and π^0 mesons. D^0 low p_{T} data show the enhancement of the production while the strong suppression of D mesons at high p_{T} is observed and is comparable to the R_{AA} of light mesons indicating significant energy loss of charm quarks in interactions with the medium. This observation is supported by the v_2 results. Right panel of Figure 1.13 shows results on D^0 v_2 in 0-80% Au+Au collisions at STAR compared to v_2 of light K_{s} mesons. The non-zero flow of D^0 mesons for p_{T} above 2 GeV/c is observed and for $p_{\mathrm{T}} < 3$ GeV/c is lower than that of light K_{s} mesons. Both, R_{AA} and v_2, can be described simultaneously by models with coalescence of charm and light quarks at mid-p_{T} [17, 18].

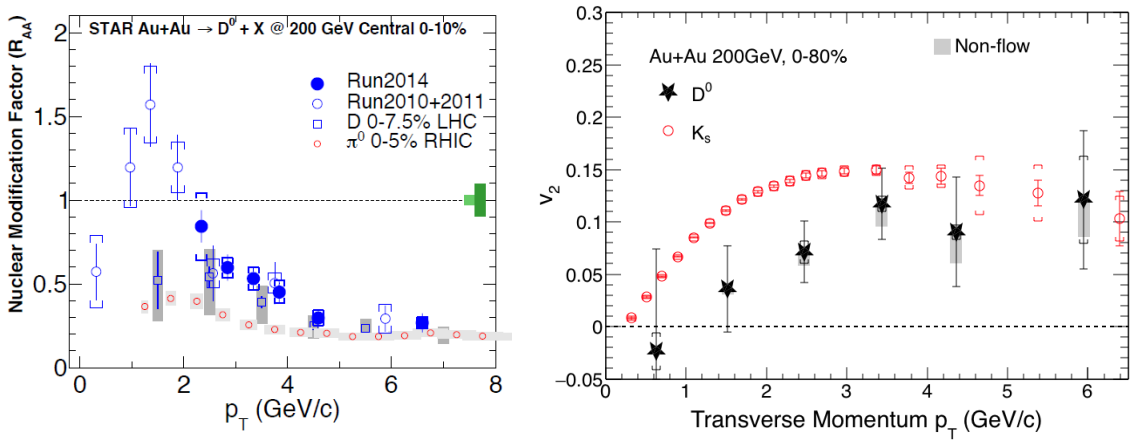

Figure 1.13: Left: Nuclear modification factor R_{AA} as a function of p_{T} of D mesons in central collisions at RHIC and LHC compared to pions [17]. Right: Elliptic flow of D mesons as a function of p_{T} compared to K_{s} mesons [18].

When the mesons containing heavy quarks cannot be directly reconstructed we can resort to the measurements of R_{AA} and v_2 of non-photonic electrons. Such measurements are important in the study of heavy quark energy loss as well as thermalization of the medium in heavy-ion collisions. Compared with previous method of reconstruction the

branching ratio is higher and also a small signal of heavy flavor can be easily separated from the background. On the other hand, up to the present time the contributions of hadrons containing c and b quark have not been clearly separated. Recently, using the newly installed Heavy Flavor Tracker (Section 2.4) the first attempts to separately measure charm and bottom quarks have been performed.

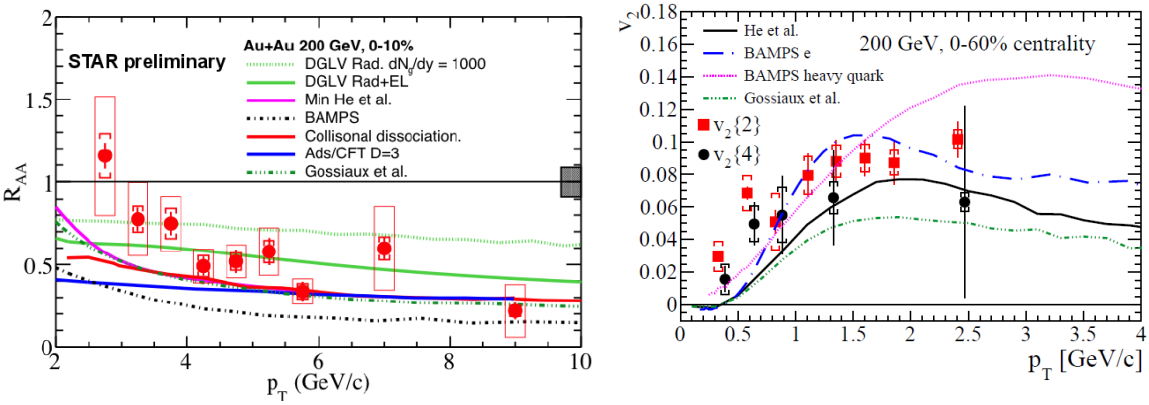

Figure 1.14: Left: Nuclear modification factor R_{AA} as a function of p_{T} of non-photonic electrons in central Au+Au collisions at RHIC compared to different model calculations described more in [19]. Right: Elliptic flow of non-photonic electrons as a function of p_{T} compared to model calculations [19].

Left panel of Figure 1.14 shows preliminary results on R_{AA} of non-photonic electrons in 0–10% most central Au+Au collisions at STAR. R_{AA} decreases towards higher p_{T} and is compared to various model calculations (for more information see [19]). Right panel of Figure 1.14 shows elliptic flow of NPE in 0–60% Au+Au data at 200 GeV. The data show non-zero v_2 at low p_{T} and significant increase for $p_{\mathrm{T}} > 4$ GeV/c possibly caused by non-flow jet-like correlations. Results on v_2 are also compared to various model calculations. Despite different mechanisms all the models assume that charm quarks are strongly coupled with the medium and predict a finite v_2 [19]. They reproduce the trend in data well, however those models that are better in describing v_2 are missing NPE R_{AA}.

1.2 Heavy quarkonia

Opposite to open heavy flavor mesons containing one heavy quark, heavy quarkonia are often called hidden flavor as they are bound states of heavy quark (c, b) and its antiquark $(\bar{c}, \bar{b})$. According to the flavor content they are called charmonia $(c\bar{c})$ or bottomonia $(b\bar{b})$. The overview of familiar examples of quarkonium states and their properties can be seen in the Table 1.1.

Suppression of heavy quarkonium production in ultrarelativistic heavy-ion collisions compared with p+p collisions due to the color screening of quark-antiquark potential was proposed as one of the most prominent predictions about the QGP formation [20]. However, different other processes may contribute to the observed quarkonium yields and complicate the suppression picture. Moreover, the production mechanism of quarkonium

production in elementary collisions is still not completely understood. For these reasons it is necessary to study heavy quarkonia in different colliding systems, at different centralities and collision energies.

State	J/ψ	χ_c	ψ'	Υ	χ_b	Υ'	χ_b'	Υ''
m_{inv} [GeV/c^2]	3.10	3.53	3.68	9.46	9.99	10.02	10.36	10.36
E_{binding} [GeV]	0.64	0.20	0.05	1.10	0.67	0.54	0.31	0.20
r [fm]	0.25	0.36	0.45	0.14	0.22	0.28	0.34	0.39

Table 1.1: Mass m_{inv}, binding energy E_{binding} and radius r of selected quarkonium states [21].

In following sections the basic ideas related to the heavy-quarkonium production and its modification as well as recent results on heavy quarkonium measurements are discussed.

1.2.1 Production mechanism in p+p collisions

The knowledge of quarkonium production mechanism in elementary collisions is important for interpretation of the results in heavy-ion collisions. However, it is still object of intensive studies.

Heavy quark-antiquark pairs $Q\bar{Q}$ are mainly produced in the interactions of partons in the initial phase of high energy collisions. Since these are hard processes total $c\bar{c}$ or $b\bar{b}$ production cross section can be calculated using tools of perturbative QCD. However, the color neutralization process, when $Q\bar{Q}$ pair forms the colorless bound state, e.g. J/ψ or Υ cannot be treated perturbatively due to the large mass of c quark compared with the scale Λ_{QCD}. Therefore, this process is studied through model calculations. The most often considered models in this topic are Color Evaporation Model (CEM), Color Singlet Model (CSM) or non-relativistic QCD (NRQCD) calculations.

In Color Evaporation Model proposed at the end of 70's [22, 23], the total quarkonium cross section is calculated as a fraction of all heavy quark-antiquark $Q\bar{Q}$ pairs with the mass less than threshold for producing a pair of open heavy flavor mesons. CEM does not make predictions on quantum numbers (color, spin) of $Q\bar{Q}$ pairs and produced quarkonium. The quarkonium is formed from $Q\bar{Q}$ pair through the radiation of soft gluons (left panel of Figure 1.15) [24].

In Color Singlet Model [25, 26] J/ψ are formed from heavy quark-antiquark $Q\bar{Q}$ pairs which are born as color singlet states. Spin and color of $Q\bar{Q}$ state remain the same as of the resulting quarkonium (middle panel of Figure 1.15).

In NRQCD approach [27] $Q\bar{Q}$ color-octet intermediate state, in addition to a color-singlet state, can bind to form a charmonium. Color-neutral state is reached through soft gluon radiation (right panel of Figure 1.15).

Different model calculations can be seen in the comparison with data. Figure 1.16 shows the measured inclusive J/ψ invariant cross section in p+p collisions at STAR and

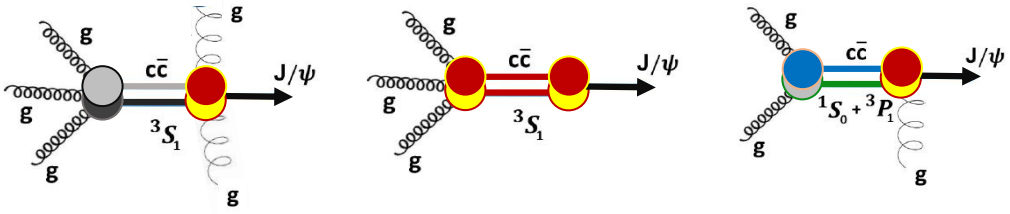

Figure 1.15: Illustration of color neutralization process in different models. From left to right: Color Evaporation Model, Color Singlet Model and Color Octet Model.

PHENIX. As can be seen, CEM overpredicts the mid-p_{T} data around 3 GeV/c while direct NNLO* CS underpredicts high-p_{T} J/ψ. In general, different model calculations describe the measured quarkonium production cross section in p+p collisions well (but not on the whole p_{T} range) although they predict different production mechanisms.

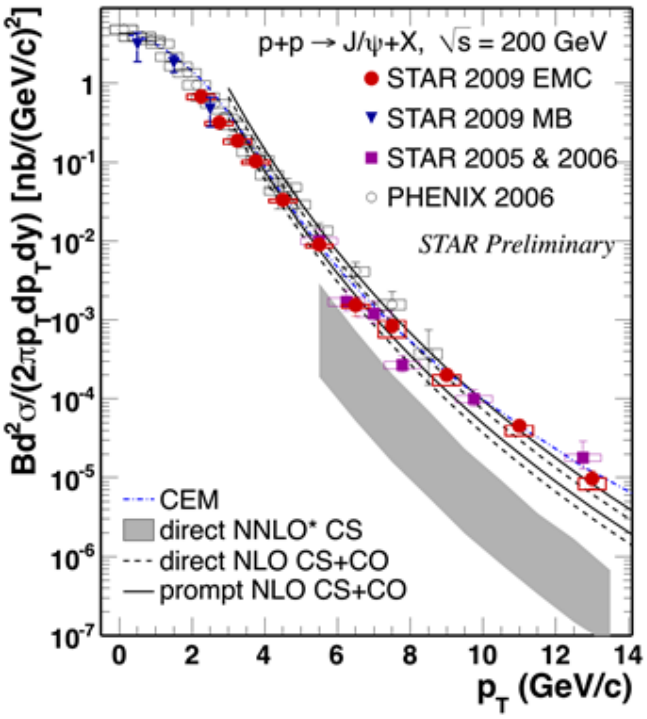

Figure 1.16: Inclusive J/ψ p_{T} spectrum in p+p collisions at 200 GeV at RHIC. Data from STAR [28, 29, 30] and PHENIX [31] are compared to different model calculations: CEM [24, 32, 33].

Therefore, for further information about the quarkonium production and to discriminate between J/ψ production models another observable is needed. An example of such observable is polarization (spin alignment) of J/ψ. CEM has no predictive power on J/ψ polarization, whereas the other model calculations give different predictions on polarization (discussed later).

The polarization of J/ψ can be measured via the angular distribution of the decay

lepton pair:

$$\frac{d^2N}{d(cos\theta)d\phi} \propto 1 + \lambda_\theta cos^2\theta + \lambda_\phi sin^2\theta + cos(2\phi) + \lambda_{\theta\phi} sin2\theta cos\phi \tag{1.6}$$

where θ is the polar angle, ϕ the azimuthal angle, λ_θ,λ_ϕ,$\lambda_{\theta\phi}$ are polarization parameters. Values of these parameters depend on a chosen reference frame. In helicity frame (HX) the polarization axis is along the J/ψ momentum in the center-of-mass frame of colliding beams (left panel of Figure 1.17) while in Collins-Soper frame (CS) the polarization axis is a bisector of the angle formed by one beam direction and the opposite direction of the other beam, in the J/ψ rest frame (right panel of Figure 1.17) [34]. Since values of polarization parameters depend on chosen reference frame it is useful to define quantity [34]

$$\lambda_{\text{inv}} = \frac{\lambda_\theta + 3\lambda_\phi}{1 - \lambda_\phi} \tag{1.7}$$

which is frame-invariant.

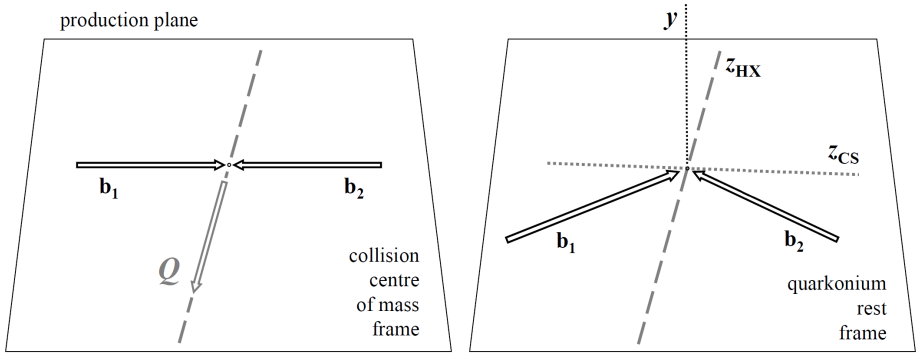

Figure 1.17: Illustration of two different definitions of polarization axis z: in helicity frame z_{XS} and Collins-Soper frame z_{CS} depending on the direction of the colliding beams b_1 and b_2 and quarkonium Q [34].

J/ψ polarization measurements at STAR, specifically measurements of λ_θ in HX frame, were performed in 200 GeV p+p collisions [35]. Results are shown in the left panel of Figure 1.18 compared with PHENIX data [36] and two model predictions (NLO$^+$ Color Singlet Model [37]) and LO NRQCD calculations with color-octet contributions [38]). NLO$^+$ CSM predicts longitudinal polarization at low and mid p_{T} while LO NRQCD (COM) predicts transverse polarization at high p_{T}. Due to the limited statistics only the λ_θ parameter was extracted. Data show decreasing trend of λ_θ towards higher p_{T} ($>$ 3 GeV/c) indicating the longitudinal polarization of J/ψ. The RHIC results are consistent with NLO$^+$ CSM prediction [35].

500 GeV p+p collisions at STAR enabled to extended the polarization measurements to higher p_{T} as can be seen from the right panel of Figure 1.18. It was also possible to extract the λ_ϕ parameter as can be seen in the left panel of Figure 1.19 where λ_ϕ is shown as a function of p_{T}. The λ_θ parameter in HX frame shows similar trend as in 200 GeV p+p collisions towards longitudinal polarization while λ_ϕ in HX frame is consistent with zero indicating no azimuthal anisotropy of J/ψ. Although λ_θ and λ_ϕ differ in HX and CS frame, the the frame invariant quantity λ_{inv} shows agreement in both frames.

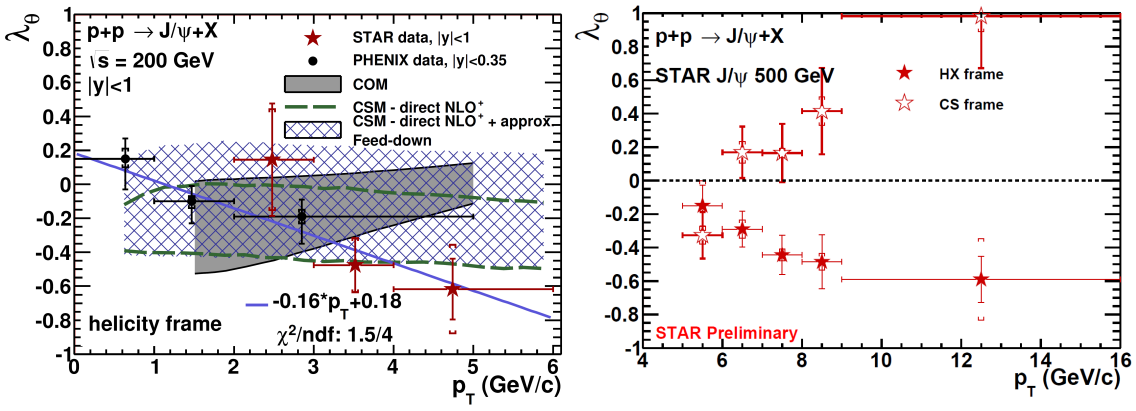

Figure 1.18: Left: λ_θ as a function of p_{T} in 200 GeV p+p collisions at STAR [35] and PHENIX [36] compared with model calculations([38], [37]). Right:λ_θ as a function of p_{T} in HX and CS frames in 500 GeV p+p collisions [39].

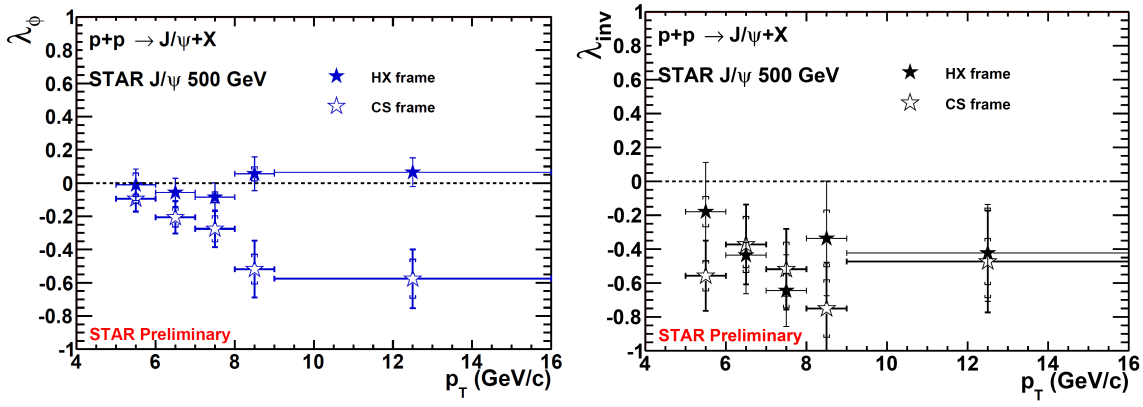

Figure 1.19: λ_ϕ (left panel) and λ_{inv}(right panel) as a function of p_{T} in HX and CS frames in 500 GeV p+p collisions [39].

1.2.2 Heavy quarkonium suppression in heavy ion collisions - melting

As indicated at the beginning of the section, the suppression of heavy quarkonium production in heavy-ion collisions compared with proton-proton collisions has been predicted as a signature of the QGP [20].

The prediction is based on the idea that if the quarkonium is placed in the quark-gluon plasma of sufficient temperature $T > T_{\mathrm{C}}$, deconfined quarks and gluons will shield the color charge, effectively weaken the interaction between heavy quarks, string tension between them will vanish and they will no longer form a bound state.

At $T = 0$ the quarkonium potential can be effectively described by the so called Cornell potential [2]:

$$V(r) = -\frac{a}{r} + kr \tag{1.8}$$

where a and k are parameters. In the QGP of the temperature T the potential can be approximately expressed by the formula [20] :

$$V(r,T) = -\frac{\alpha}{r} exp\left[-r/r_D(T)\right], \tag{1.9}$$

where r is the radius of quarkonium and r_{D} is the Debye screening radius which sets the distance outside of which the color charge of heavy quark is screened. This is illustrated in Figure 1.20. The Debye screening radius goes down with the increase of the temperature of the medium (approximately as $\sim 1/\sqrt{T}$ [40]). The temperature at which r_{D} decreases

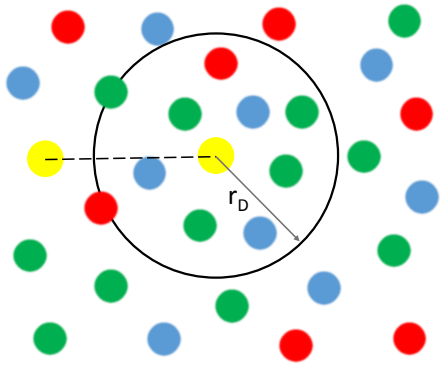

Figure 1.20: The schematic drawing of the Debye screening radius r_{D} in QGP. Heavy quarks from quarkonium (yellow) effectively do not see each other.

to the quarkonium radius r is the dissociation temperature T_{D} at which the quarkonium can no longer form a bound state. Since the radii of quarkonium states differ they are expected to dissociate at different temperatures. Therefore, it has been predicted that by measuring the states that survived in the QGP the information about the temperature of the medium could be obtained [40]. However, formula presented above is very approximate and there are different potential models (some of them were proposed also in [40]) and lattice QCD calculations which try to describe quarkonium dissociation mechanism.

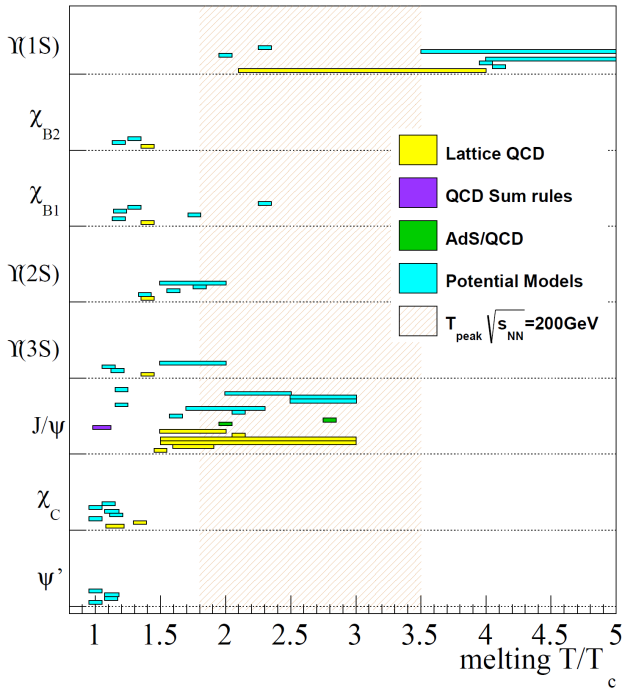

Figure 1.21: The dissociation temperatures of different quarkonium states relative to critical temperature T/T_c – different models calculations (Lattice QCD, QCD sum rules, Ads/QCD, potential models) were used. The shaded band denotes the hydrodynamic estimation for the highest temperature reached in 200 GeV Au+Au collisions. Estimations were performed using different T_c values. Horizontal bars denote the range in which the quarkonium state undergoes modifications until it completely melts [41].

Figure 1.21 shows a compilation of various model predictions of dissociation temperatures of different quarkonium states.

1.2.3 Other effects on heavy quarkonium production

Suppression of heavy quarkonium production due to the dissociation in QGP is not the only effect which is expected to modify the quarkonium production in heavy-ion collisions. Moreover, some of these effects are expected to modify quarkonium production also in e.g. d+Au collisions in which the QGP is not expected to be formed. This modification of quarkonium production needs to be taken into account before any conclusions on modification in heavy-ion collisions are drawn.

Recombination

Suppression of heavy quarkonium production in QGP due to the melting can be compensated by the recombination of single thermalized heavy quarks. At sufficiently high energy the recombination mechanism takes part and leads to J/ψ production enhance-

ment. J/ψs produced from dissociated charm quarks are, in comparison to initially produced J/ψs from hard processes, distributed in the low-p_{T} region. This is illustrated in the Figure 1.22 which shows model [42] predictions of modification of J/ψ production in Cu+Cu and Au+Au collisions. As shown, both effects, dissociation and recombination are more intensive in Au+Au collisions where the energy density of the created medium is higher. The evidence of recombination effect can be observed from comparison of mod-

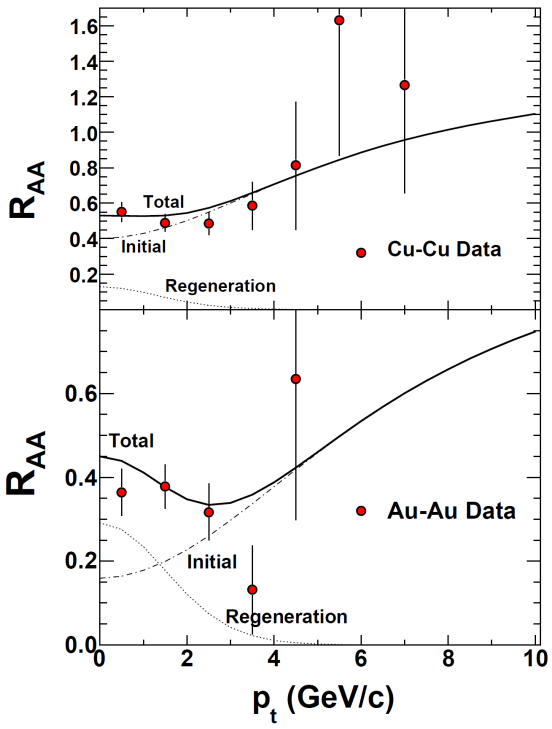

Figure 1.22: Model predictions on modification of J/ψ production in Cu+Cu and Au+Au collisions compared with STAR and PHENIX data [42].

ification of J/ψ production at RHIC and LHC. This is illustrated in Figure 1.23 which shows J/ψ R_{AA} measured at PHENIX and ALICE at forward rapidity. At LHC where much higher energy of the collisions are reached the suppression of J/ψ as a function of N_{part} is lower than at RHIC and does not depend very much on centrality [43]. This result favors the scenario of more significant effect of recombination compared with melting at LHC energies than at RHIC.

Leakage effect

One would expect that low-p_{T} J/ψ are easy to be eaten by the medium created in the collision. On the other hand, the high-p_{T} J/ψ can escape the anomalous hot matter region and thus are not object to dissociate anymore. Therefore, their production is expected to be less suppressed. This is called the leakage effect [44].

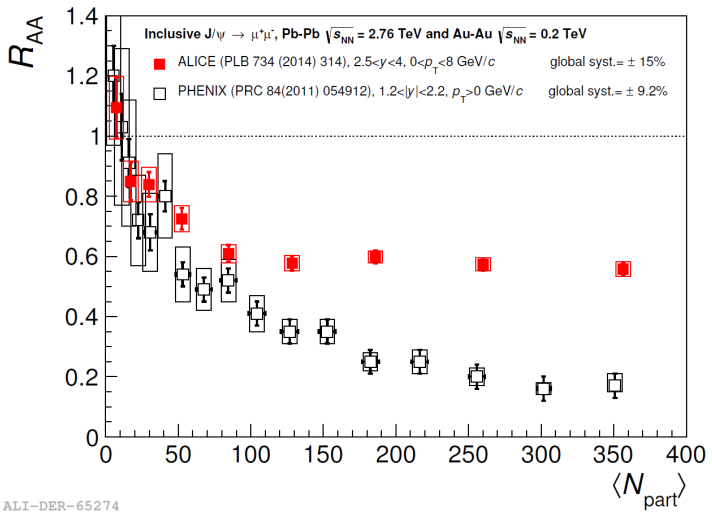

Figure 1.23: J/ψ R_{AA} as a function of N_{part} at PHENIX and ALICE at forward rapidity [43].

Cold-nuclear-matter (CNM) effects

As indicated above, to distinguish between effects of QGP and cold medium, CNM effects need to be studied. Under the term CNM effects nuclear shadowing, Cronin effect and nuclear absorption are often understood.

- **Nuclear shadowing** denotes modification of nuclear parton distribution functions (nPDFs) relative to PDFs in a proton taking into account the fact that nucleus cannot be simply considered as a superposition of nucleons, i.e. parton densities in a nucleon bound in nucleus are different from those in a free nucleon. It is often expressed as the ratio of nuclear parton distribution function (for each flavor i) divided by the PDF in proton [45]:

$$R_i^A(x, Q^2) = \frac{f_i^A(x, Q^2)}{f_i^{nucleon}(x, Q^2)} \tag{1.10}$$

  where x is the fraction of the momentum of the nucleon in nucleus carried by the parton and Q^2 is $-q^2$ which denotes the transferred four-momenta of incident nucleon [45].

  An illustration of $R_{\mathrm{i}}^{\mathrm{A}}$ dependence on x for fixed Q^2 can be seen in the Figure 1.24. At $x < 0.1$ the value of $R_{\mathrm{i}}^{\mathrm{A}}$ is less than one while for $0.1 < x < 0.3$ it is above 1. This is called nuclear shadowing or antishadowing, respectively. These effects come from the gluon fusion and recombination between different nucleons in a nucleus, which change the distributions of gluon and quarks but not their total momentum. Consequently, the loss of gluon momentum in the shadowing range should be compensated by the momentum of new gluons at larger x (antishadowing) [45]. Since gluon fusion is one of the dominant processes of heavy quark and antiquark pair $Q\bar{Q}$ production the nuclear shadowing or gluon shadowing, is important effect in the quarkonium

production and is expected to affect the quarkonium production in nuclear collisions compared with p+p collisions.

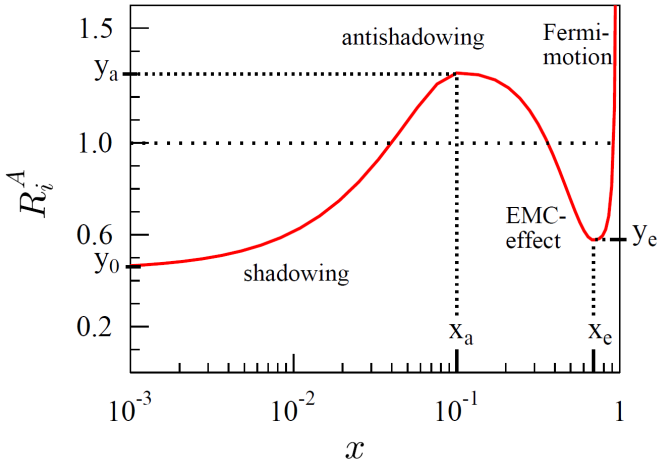

Figure 1.24: An illustration of nuclear ratio R_i^A dependence on momentum fraction x [45].

- **Cronin effect** is often interpreted as "transverse momentum kick" which partons (quarks and gluons) acquire in multiple scatterings of partons from the proton off partons from the nucleus in the initial state of the collision resulting in higher p_T of produced quarkonia in p+A (A+A) collisions relative to p+p collisions [46].

- **Nuclear absorption** refers to the dissociation of heavy quark-antiquark pairs before they form quarkonium in the initial states of the collision [46]. As these prequarkonium states pass by and scatter on nucleons they can be absorbed by these nucleons. Nuclear absorption is then expressed by the specific absorption cross section.

Interactions with comovers

In general the quarkonium (or prequarkonium state) can be dissociated through interactions with the constituents of any medium present in the collision. In a comover scenario the suppression of quarkonium states arises from scattering of quarkonia with particles produced in collision travelling along with $Q\bar{Q}$ pair [47]. The comover suppression is stronger in more central collisions (higher density of comovers) and in asymmetric collisions such as p+A in the direction of the nucleus. Due to its larger size the effect is also more significant for ψ (2S) than J/ψ. Left panel of Figure 1.25 shows recent results on R_{pPb} of J/ψ and ψ (2S) at 5.02 TeV at LHC. A significant suppression of ψ (2S) compared with J/ψ can be seen. This trend is seen also in PHENIX 200 GeV d+Au data show in the right panel of Figure 1.25. Similar observations at lower energies were easily explained by nuclear absorption. However, such explanation fails at higher energies. It can be seen from Figure 1.25 that calculation [48] which includes interactions of quarkonia with comoving particles describes the observed behavior well.

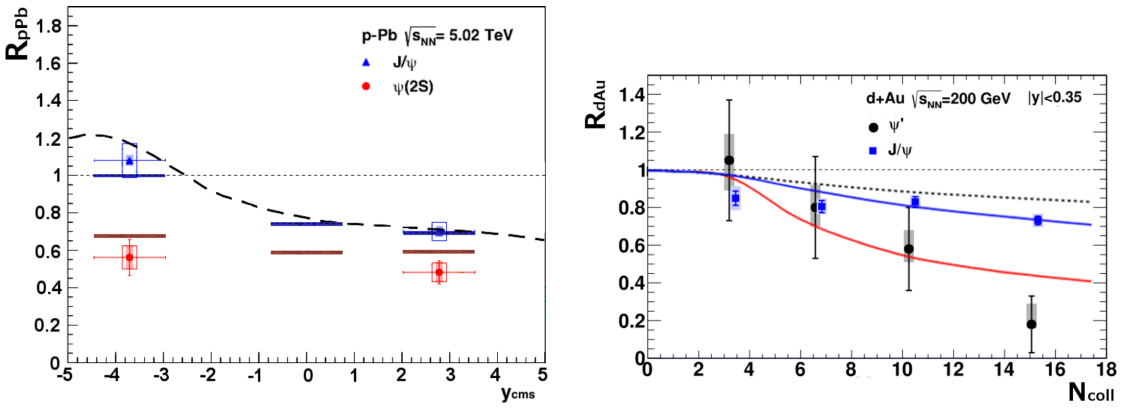

Figure 1.25: Left: R_{pPb} as a function of rapidity y for J/ψ and ψ (2S) at LHC. The data are compared to model calculation (blue line for J/ψ and red for ψ (2S)) including comover interactions. Right: Calculated R_{dAu} as a function of N_{coll} for J/ψ(blue line) and ψ (2S) (red line) compared with RHIC data. The suppression due to the shadowing corrections (discontinuous line) is also shown [48].

Feed-down effects

The inclusive production of J/ψ mesons contains several cotributions. In addition to the directly produced J/ψ there are also those coming from decays of heavier charmonium states (ψ', χ_c). The directly produced J/ψ and those from higher charmonium states are called prompt J/ψ. Contributions to inclusive J/ψ from higher excited states account for about 30% from χ_c and 10% from ψ' in p+p collisions. There is also non-prompt contribution to inclusive J/ψ production coming from the decays of beauty hadrons which accounts for 10-25 % in p+p collisions [21]. Similarly, in the case of Υ 30% come from $\chi_b(1P)$ states, 10% from direct Υ' states and 10% from $\chi_b(2P)$ states [21]. Since higher excited states are expected to dissociate in QGP easier (at lower temperature) than J/ψ or Υ the production of ground states can be suppressed even if the system does not reach their dissociation temperature.

1.2.4 Heavy quarkonium measurements in nuclear collisions at RHIC

At RHIC the heavy quarkonium studies focus on a variety of measurements of J/ψ and Υ mesons in collisions of different nuclei such as Cu+Au, Au+Au and U+U. These colliding systems allow to study the QGP effects and their dependence on the energy density of the medium created in the evolution of the collision. To distinguish the effects of cold nuclear matter from those caused by the hot plasma, heavy quarkonia have been studied in d+Au and Cu+Au collisions.

Results from Au+Au collisions

Figure 1.26 shows the nuclear modification factor R_{AA} as a function of number of participating nucleons N_{part} in the collision of high-p_{T} J/ψ together with low-p_{T} data. As can be seen, low-p_{T} J/ψ are more suppressed than high-p_{T} J/ψ over the whole N_{part}

range. However, suppression of high-p_{T} J/ψ in central collisions is also significant. These results are consistent with model predictions [42] which include suppression of J/ψ production due to the color screening and statistical regeneration as a secondary production mechanism. Since regeneration is more significant at low-p_{T} high-p_{T} J/ψ can serve as a cleaner probe of suppression effects of the hot medium.

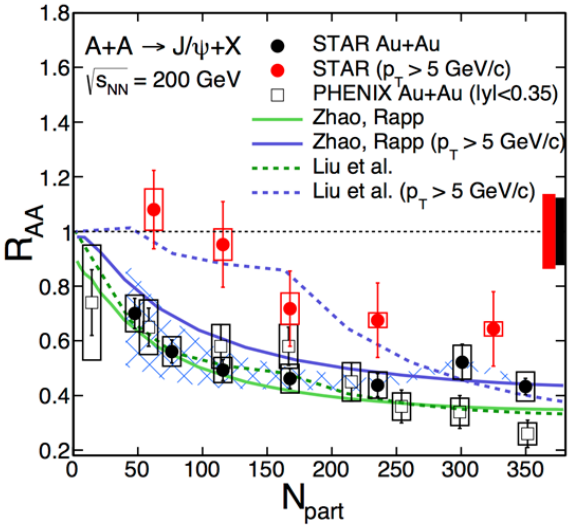

Figure 1.26: J/ψ nuclear modification factor R_{AA} in 200 GeV Au+Au collisions as a function of number of participant nucleons N_{part}. Data are from STAR [49, 28] and PHENIX [50] and compared to model calculations [42, 46].

To study the energy dependence of medium effects STAR has measured the dependence of J/ψ nuclear modification factor R_{AA} in Au+Au collisions at $\sqrt{s_{\mathrm{NN}}} = 39,\ 62.4,\ 200$ GeV. Results can be seen in Figure 1.27 which shows N_{part} (left panel) and p_{T} (right panel) dependence of R_{AA}. As can be seen, suppression is similar at all energies and is consistent with theoretical calculations [46] indicating interplay between the suppression due to the melting and regeneration.

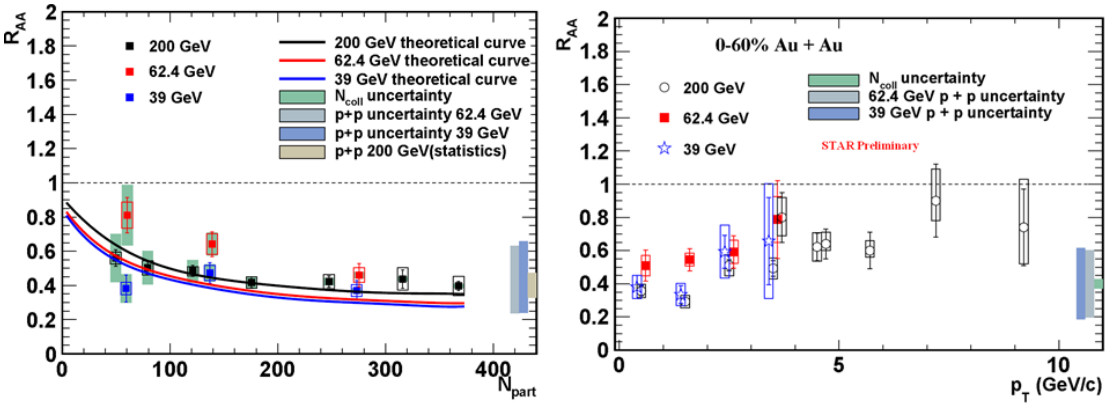

Figure 1.27: J/ψ nuclear modification factor R_{AA} in 39, 62.4, 200 GeV Au+Au collisions as a function of number of participant nucleons N_{part} compared to model calculations [46] (left panel) and as a function of p_{T} (right panel).

However, the recombination of J/ψ from thermalized charm quarks has not been unambiguously confirmed experimentally at RHIC. Azimuthal flow is found to be an appropriate observable to further distinguish the coalescence of dissociated charm quarks from other effects which modify J/ψ production. Directly produced J/ψ come from hard processes which do not have initial collective motion. Thus they are expected to gain only a small azimuthal anisotropy in non-central collisions which may come from azimuthally different absorption due to the different path lengths in azimuth [51]. On the other hand, J/ψ from recombination of thermalized charm quarks are expected to gain the flow of charm quarks [51]. Both panels of Figure 1.28 show the elliptic flow v_2 of J/ψ in Au+Au collisions at STAR. In the left panel v_2 is shown as a function of p_{T} for different centrality bins, the right panel shows J/ψ v_2 for integrated centrality 0 - 80 % and compared to charged hadrons, ϕ meson and model calculations. As can be seen, v_2 is similar in all centrality bins and for $p_{\mathrm{T}} > 2$ GeV/c consistent with zero. Results thus disfavor the scenario that J/ψs with $p_{\mathrm{T}} > 2$ GeV/c are produced dominantly by coalescence from thermalized (anti)charm quarks.

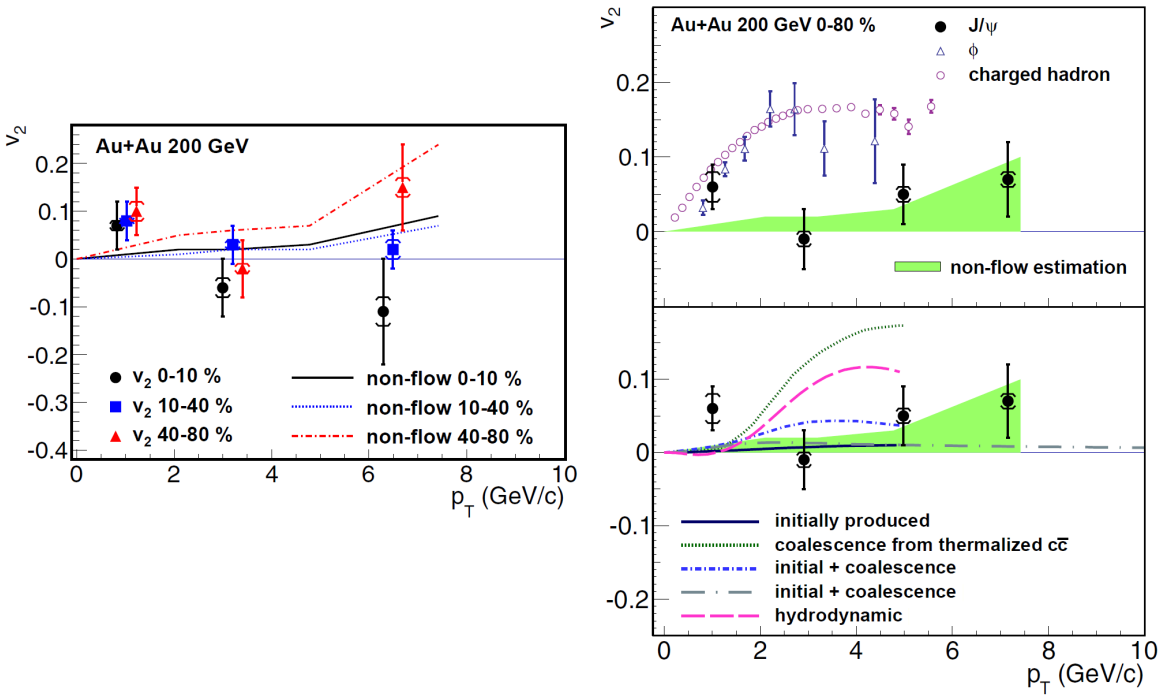

Figure 1.28: J/ψ elliptic flow v_2 as a function of p_{T} in 200 GeV Au+Au collisions in different centrality bins (left panel) and for 0 - 80 % most central Au+Au collisions(right panel) compared to charged hadrons and ϕ meson (upper panel) and various model predictions (lower panel) [51].

Results from U+U collisions

Measurements of J/ψ in U+U collisions at $\sqrt{s_{\mathrm{NN}}} = 193$ GeV provide an opportunity to prove the expected increase of the energy density of the medium up to above 20 % compared with Au+Au collisions at 200 GeV (section 1.1.4). Increase of the energy

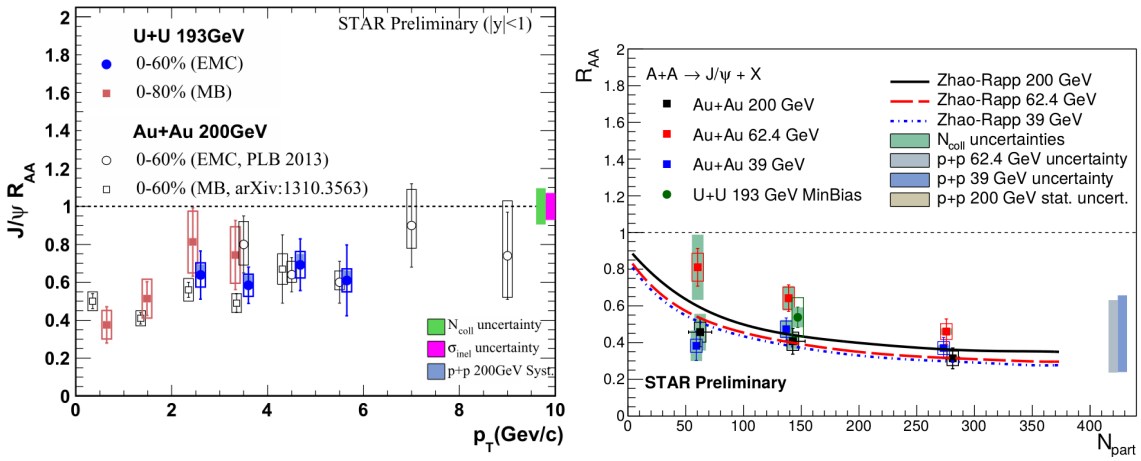

Figure 1.29: Left: J/ψ $R_{\rm AA}$ as a function of $p_{\rm T}$ in minimum-bias U+U collisions at mid-rapidity at $\sqrt{s_{\rm NN}} = 193$ GeV at STAR [52]. Right: $N_{\rm part}$ dependence of $R_{\rm AA}$ in Au+Au collisions at different energies, minimum bias U+U point included.

density can affect resulting $R_{\rm AA}$ in several ways: on one hand, it can intensify the effect of color screening on the other hand, higher energy density means higher probability of J/ψ production via the coalescence of unbound $c\bar{c}$ pairs. Results on modification of J/ψ production in Au+Au collisions at various energies indicated possible interplay of melting and recombination. Thus, the question is how the interplay evolves in the high energy density reached in U+U collisions.

Figure 1.29 shows preliminary results on J/ψ nuclear modification factor in minimum-bias and HT triggered U+U collisions at mid-rapidity at $\sqrt{s_{\rm NN}} = 193$ GeV at STAR. In the left panel U+U data are compared to 200 GeV Au+Au $R_{\rm AA}$ as a function of $p_{\rm T}$ while the right panel shows $N_{\rm part}$ dependence of $R_{\rm AA}$ Au+Au collisions at different energies with U+U point added. Data show that U+U and Au+Au results with similar $N_{\rm part}$ are also similar. However, the hot matter effects are expected to be the most significant in central collisions, therefore, study of $N_{\rm part}$-dependence of J/ψ nuclear modification factor is important.

PHENIX has measured $N_{\rm part}$-dependence of J/ψ $R_{\rm AA}$ in U+U and Au+Au collisions at forward rapidity as shown in the panels of Figure 1.30. It is important to note how the interpretation of results depends on the parametrization of the number of binary collisions $N_{\rm bin}$ in U+U collisions. $N_{\rm bin}$ is calculated from Glauber model [53] using the Woods-Saxon distribution for deformed nuclei [54]. Two sets of results were obtained using different values of parameters in Woods-Saxon distribution : set 1 in the left panel [55] and set 2 in the right panel [56]. It is also interesting to look at the centrality dependence of $R^{\rm UU}_{\rm AuAu}$ which is defined as

$$R^{\rm UU}_{\rm AuAu} = \frac{dN^{\rm UU}/dy}{dN^{\rm UU}/dy} \left(\frac{N^{\rm AuAu}_{\rm bin}}{0.964 \times N^{\rm UU}_{\rm bin}} \right)^2 \tag{1.11}$$

where the first fraction denotes the ratio of invariant yields in U+U and Au+Au collisions, $N_{\rm bin}$ is the average value of binary collisions in a given collision system and centrality class. The quadratic dependence of the $N_{\rm bin}$ ratio is based on the expected scaling of

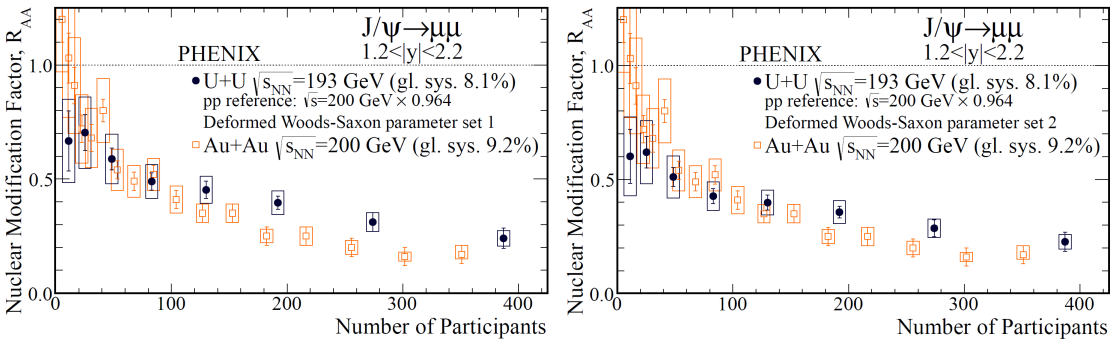

Figure 1.30: J/ψ nuclear modification factor R_{AA} in U+U and Au+Au collisions as a function of N_{part} at PHENIX [54]obtained using different parametrizations of N_{bin}: set 1 in the left panel [55] and set 2 in the right panel [56] .

J/ψ cross section in the case of $c\bar{c}$ coalescence, and, finally the factor of 0.964 is based on the difference between the charm cross section in p+p collisions at $\sqrt{s} = 200$ GeV and $\sqrt{s} = 193$ GeV. Resulting $R^{\mathrm{UU}}_{\mathrm{AuAu}}$ is shown in the Figure 1.31.

Moving back to Figure 1.30 and looking at both sets of N_{bin} the J/ψ production in U+U collisions is found to be less suppressed than in Au+Au collisions in central collisions that have a similar number of participants. These results are consistent with observation from Figure 1.31 for set 1 of N_{bin}, however for N_{bin} from set 2 the results suggest that in the 40–60% centrality range the suppression observed in U+U compared to Au+Au due to the higher energy density is more important than recombination effect due to the higher charm production.

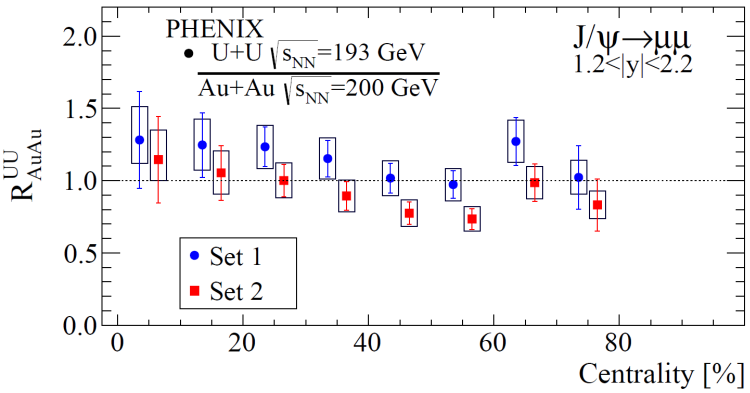

Figure 1.31: Modification of J/ψ production in U+U collisions compared to Au+Au collisions $R^{\mathrm{UU}}_{\mathrm{AuAu}}$ as a function of centrality in U+U and Au+Au collisions at PHENIX [54].

Υ in Au+Au and U+U collisions at STAR

To obtain more information about the hot medium effects in heavy-ion collisions Υ was studied at STAR in U+U and Au+Au collisions. Compared with J/ψ meson Υ is more tightly bound state which is expected to be less affected by the effects of recombination

and comover absorption [57]. Accordingly, it has been proposed as a cleaner probe of the suppression in the hot medium. However, measurements of Υ at STAR are challenging due to the low production rate and complicated triggering.

Figure 1.32 shows R_{AA} of Υ(1S+2S+3S) states (left panel) and Υ(1S) state (right panel) separately as a function of number of participating nucleons in the collision N_{part} in 193 GeV U+U and 200 GeV Au+Au collisions at STAR, Au+Au collisions at PHENIX and compares them with data from Pb+Pb collisions at CMS at 2.76 TeV. As can be seen, for all three experiments Υ(1S+2S+3S) are more suppressed than Υ(1S) state as one would expect from sequential melting of different quarkonium states. STAR and PHENIX data show similar trend, i.e. no suppression in peripheral collisions and significant suppression towards the most central collisions. Also CMS data show significant suppression even in peripheral collisions which slightly depends on N_{part}. In the most central collisions, STAR U+U data are consistent with CMS Pb+Pb results. The presented data indicate energy density dependence of Υ suppression. Compared with J/ψ which show less suppression at LHC than at RHIC Υ results do not indicate significant role of recombination as the production process.

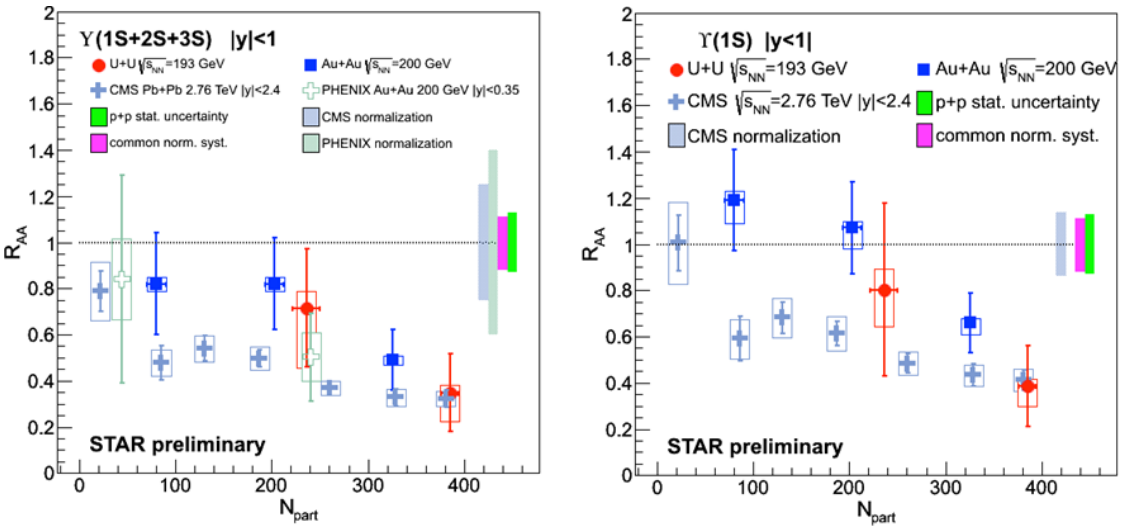

Figure 1.32: Modification of Υ(1S+2S+3S) states (left panel) and Υ(1S) state (right panel) production in U+U collisions and Au+Au collisions R_{AA} as a function of number of participating nucleons N_{part} in U+U and Au+Au collisions at STAR compared to PHENIX [58] and CMS [59] results.

Measurements of CNM effects

To distinguish the modification of quarkonium production due to the non-QGP effects from the effects present only in the hot medium, J/ψ and Υ have been studied in d+Au collisions at STAR.

Left panel of Figure 1.33 illustrates R_{dAu} of J/ψ as a function of p_{T}. Data from STAR at $|y| < 1.0$ are shown together with PHENIX data $|y| < 0.35$ and model calculations. These include nuclear shadowing or nuclear shadowing with J/ψ nuclear absorption as

a free parameter (its upper limit was found to be 8.7 mb) [60]. J/ψ R_{dAu} measured at STAR is consistent with no suppression.

Right panel of Figure 1.33 shows R_{dAu} of $\Upsilon(1S+2S+3S)$ states as a function of rapidity y. Models of Υ production in cold-nuclear-matter which include nuclear shadowing and initial-state partonic energy loss, are consistent with data. On the other hand, the suppression observed at mid-rapidity $|y| < 0.5$ is beyond model calculations. Higher statistics is needed to further investigate this deviation [61].

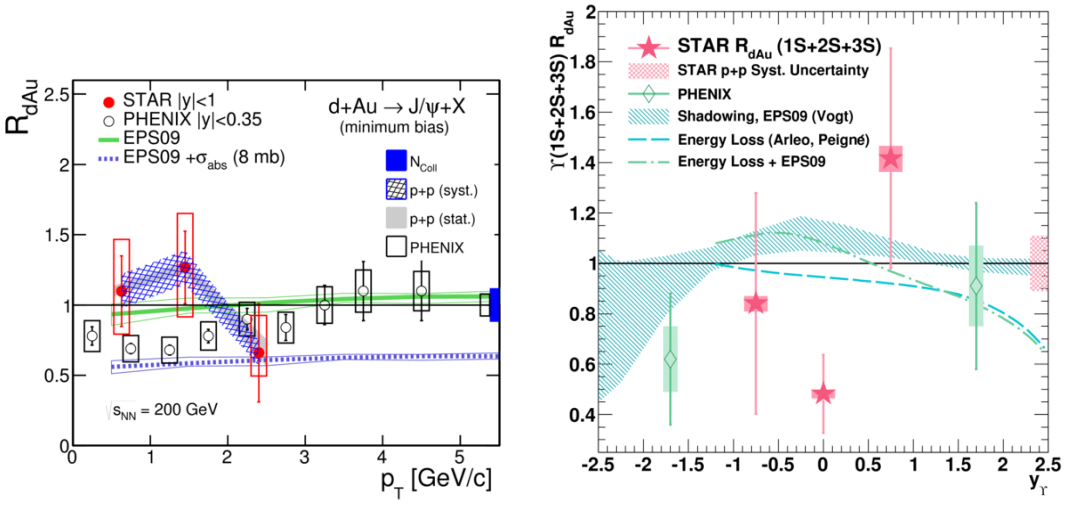

Figure 1.33: Left: R_{dAu} of J/ψ as a function of p_{T} [30]. Data from STAR at $|y| < 1.0$ are shown together with PHENIX data $|y| < 0.35$ [58] and model calculations including only nuclear shadowing (green line) [45] and nuclear shadowing with J/ψ nuclear absorption (dotted line) [60]. Right: R_{dAu} of Υ as a function of rapidity y [61]. The shaded band shows the prediction for RdAu from EPS09 nuclear shadowing calculations and its uncertainty. The dashed curve shows suppression due to initial-state parton energy loss and the dot-dashed curve shows the same model with EPS09 included [62].

Collisions of of Cu+Au nuclei can also help to understand and distinguish hot and cold nuclear matter effects. Due to the asymmetry of this system Cu-going versus Au-going production of J/ψ will contain different contributions from hot and CNM effects. The comparison of modification of J/ψ production in d+Au, Cu+Au and Au+Au can provide a new insight on the interplay of the contributions and determine if the hot and cold nuclear matter effects are factorizable. PHENIX has measured J/ψ R_{AA} as a function of N_{part} in Cu+Au collisions at $\sqrt{s_{\mathrm{NN}}} = 200$ GeV. PHENIX results can be seen in the left panel of Figure 1.34. In Au direction the energy density of the medium is expected to be higher than in Cu direction (up to 20 %) due to the higher particle multiplicity. This can turn into the stronger effect of J/ψ suppression but also recombination. Looking at the data the modification of J/ψ production observed in backward rapidity (Au-going) is similar to that observed in Au+Au collisions while in forward rapidity (Cu-going) it shows stronger suppression [63].Results indicate that the melting in the hot matter is not the only effect present in Au direction (in that case R_{AA} would be lower in backward

rapidity) and Au+Au collisions but mixture of different effects (melting, recombination, CNM effects, ...).

It is also interesting to look at the forward-to-backward ratio of J/ψ yields shown in the right panel of Figure 1.34. The data are shown together with theoretical calculation which reflects the difference of the shadowing effects in forward and backward direction. The data in are comparable in magnitude and of the same sign as the difference from the shadowing effects [63].

These results shed new light on the interplay of hot and cold nuclear matter effects at RHIC.

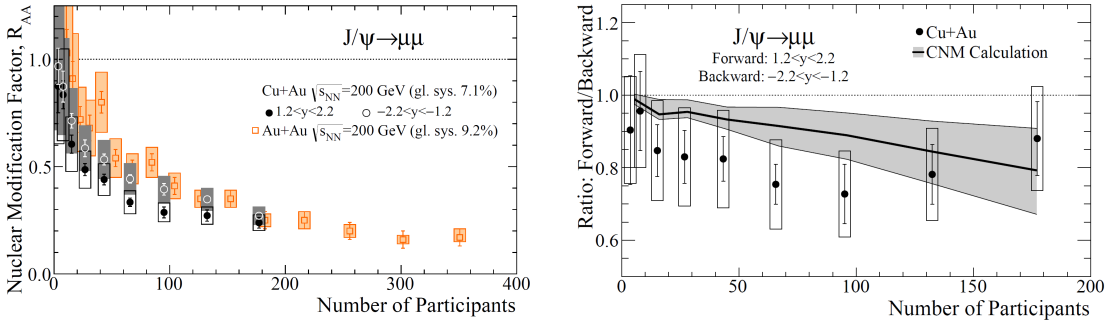

Figure 1.34: Left: Nuclear modification factor R_{AA} as a function of number of participat nucleons N_{part}. Data at forward rapidity (Cu-going) are shown as closed circles and at backward rapidity (Au-going) as open circles. Au+Au data (red squares) are also shown, averaged over forward and backward rapidities [63]. Right: Forward-to-backward ratio of J/ψ yields in Cu+Au collisions. Theoretical calculation of shadowing effects is also shown [63].

Chapter 2

The STAR experiment

The STAR (Solenoidal Tracker at RHIC) experiment [64] is a multi-purpose detector dedicated to study the strongly interacting matter at high temperature and high energy density. Its main purpose is detection, tracking and identification of charged particles at mid-rapidity.

STAR is located at the Relativistic Heavy Ion Collider (RHIC) in Brookhaven National Laboratory in New York, USA. The layout of the RHIC complex can be seen in the Figure 2.1. RHIC is able to collide ions of different masses and at different energies. Moreover, RHIC is the only device in the world capable of colliding polarized protons. Until now collisions of p+p, p+Au, p+Al, d+Au, h+Au, Cu+Cu, Cu+Au, Au+Au and U+U at energies from 62.4 GeV to 500 GeV for protons and from 7.7 GeV to 200 GeV for heavy ions have been performed at RHIC [65].

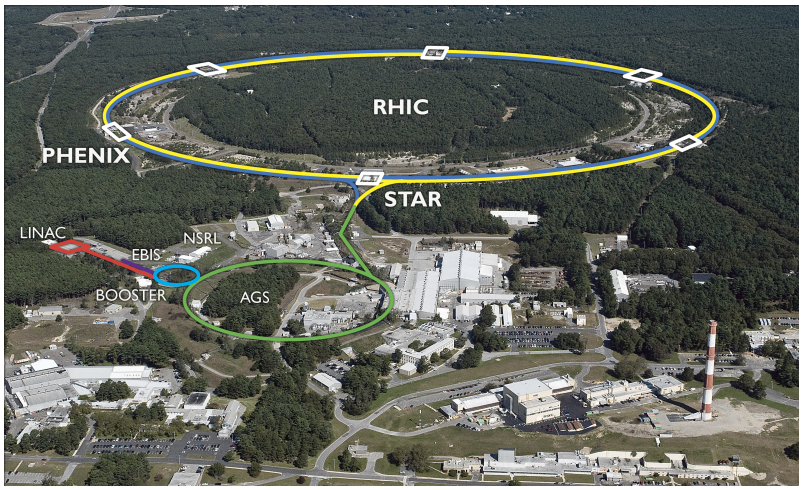

Figure 2.1: The layout of the RHIC complex [66].

As can be seen in the Figure 2.1 RHIC consists of a chain of particle accelerators. Heavy ions start their journey in the Electron Beam Ion Source (EBIS) while protons are supplied by Linac. Heavy ions as well as protons are then transferred to the Booster synchrotron where they are accelerated to 37 % of the speed of light. Afterwards they get even more energy in Alternating Gradient Synchrotron (AGS). As the ions exit AGS they

are travelling at 99.7 % of the speed of light. Afterwards the relativistic beams of ions are transferred through the AGS-to-RHIC (AtR) transfer line to one of two RHIC concentric storage rings. There is a switching magnet at the end of AtR which sends the bunches of ions either to blue or yellow ring. Beams are further accelerated in counter-rotating rings and can be collided in six intersection points [67]. Currently, experiments STAR and PHENIX [68] are located at two of these points.

The massive 1200 tons weighting STAR detector located at 6 o'clock of RHIC shares its z-axis with the beam-line. It is cylindrical in shape and covers 2π in azimuth and two units of rapidity around the mid-rapidity.

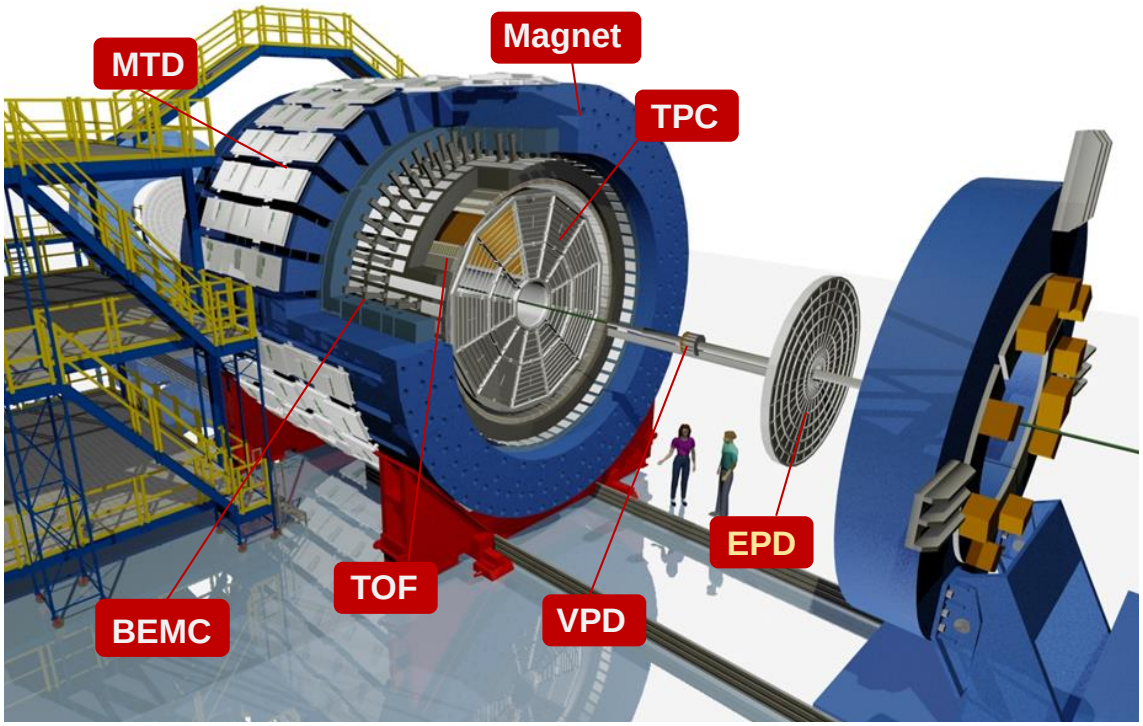

Figure 2.2: The layout of the STAR detector. Picture by Alex Schmah.

STAR consists of various subsystems, schematically shown in the Figure 2.2. These subsystems perform different tasks: they can be used for triggering, particle identification or tracking. Following sections are dedicated to detectors important for the purpose of the analysis of J/ψ presented in this thesis the Time Projection Chamber (TPC), the Time of Flight (TOF) detector and the Barrel Electromagnetic Calorimeter (BEMC). Other detectors important for open heavy flavor and heavy quarkonium studies are also described, namely the Heavy Flavor Tracker (HFT) which sits inside the TPC and the Muon Telescope Detector (MTD) located behind the STAR magnet.

The triggering system of the STAR detector which performs the primary selection of the data from events is also presented.

2.1 Time Projection Chamber

The heart of the STAR detector, the Time Projection Chamber (TPC), is the main tracking device of STAR. It provides identification of charged particles according to their specific ionization energy loss in the material.

The layout of the TPC can be seen in the Figure 2.3. It is cylindrical in shape and surrounds the inner tracking system of the STAR detector located around the beam-pipe. TPC is 4.2 m long and has an inner diameter of the drift volume 1 m and outer diameter 4 m [69]. It covers pseudorapidity $|\eta| < 1.8$ and full azimuthal angle.

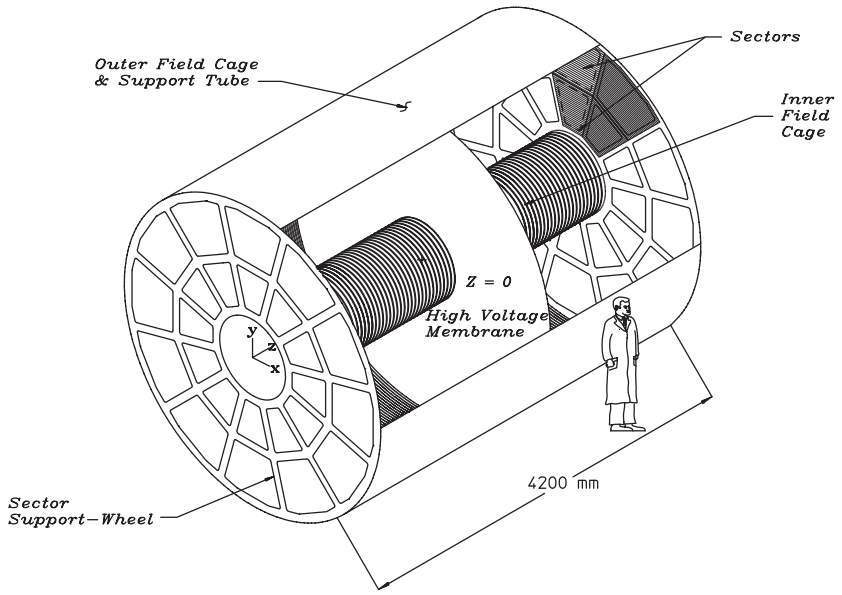

Figure 2.3: The Time Projection Chamber [69].

TPC sits in a uniform electric and magnetic field. The electric field of ca. 135 V/cm is generated by Central Membrane (cathode membrane) held at the voltage -28 kV and grounded anode end caps. The 0.5 T magnetic field is generated by the solenoidal STAR magnet [69].

TPC is filled with P10 gas (90% Argon, 10% Methane) operating at 2 mbar above the atmospheric pressure. In the operating electric field of TPC the drift velocity in the P10 gas is stable and insensitive to small variations in temperature and pressure and this is required.

TPC has anode read out system located on the end caps of the chamber consisting of 136 560 read-out modules based on Multi Wire Proportional Chambers technology [69]. Read-out pads are connected into pad rows and these are divided into 12 sectors. In each sector there are 13 inner and 32 outer pad rows. The inner sectors, located in the area of the highest track density, are equipped with smaller pads than the outer sectors to provide necessary better resolution. Figure 2.4 shows the schematic drawing of one pad plane.

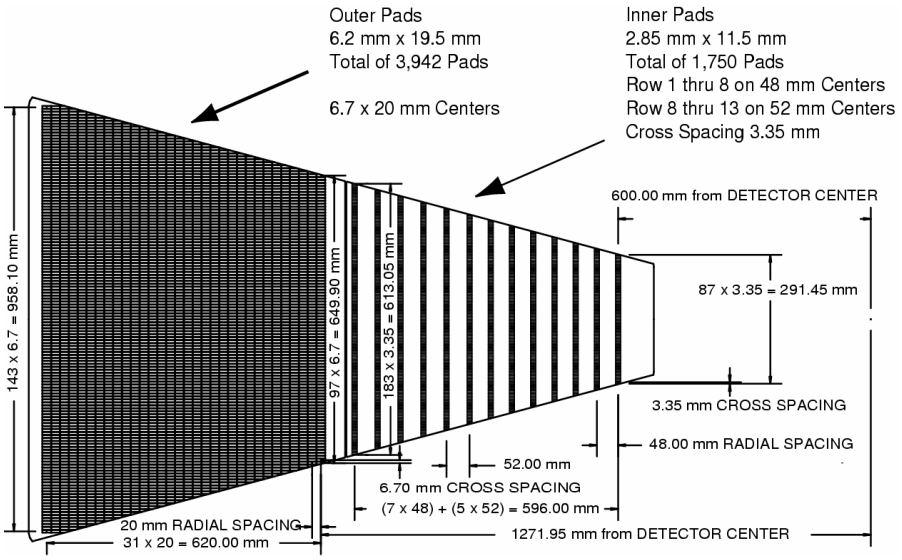

Figure 2.4: The anode pad plane of the read out system of the TPC [69].

2.1.1 Particle identification using TPC

As the primary ionizing particle emerging from collision traverses the volume of the TPC it ionizes the atoms of the gas. The electric field of the TPC causes that positive ions travel to the Central Membrane while the (secondary) electrons drift with a constant velocity ≈ 5.45 cm/μs [69] towards the end caps resulting in the drift time of $\lessapprox 40$ μs.

Since TPC has anode read-out system the path of the primary particle is reconstructed from the secondary electrons measured on pads on the end caps.

Magnetic field in which the TPC sits curves the trajectories of charged particles. Since the momentum of the particle is proportional to the radius of its curvature, tracking of the particles can determine their momenta. TPC enables to measure momenta over a range of 100 MeV/c to 30 GeV/c [70]. The relative momentum resolution of TPC was found to be $\sim 2\%$ for the majority of the tracks [69]. It is improved as the number of hit points along the track increases and as the momentum of particle decreases.

As the primary particles ionize the atoms of the gas they loose the energy which turns out into the charge of secondary electrons collected in the TPC pads. The ionization energy loss of particle per unit of length dE/dx in a given medium (TPC gas) can be calculated for different particle species using the Bichsel functions [71] and compared with measured values. The relative resolution of energy loss in TPC was established to be 7% [72]. Figure 2.5 shows the measured and calculated energy loss of charged particles in the TPC as a function of the particle momentum. As can be seen from the figure, pions, kaons and protons can be well separated in the low p region (for $p < 1$ GeV/c). However, towards higher p_{T} energy loss bands of different particles overlap. In general, using the TPC, particles are identified over a momentum range from 100 MeV/c to ~ 1 GeV/c. To extend particle identification capabilities towards higher p_{T} other detectors (e.g. TOF, BEMC) are needed.

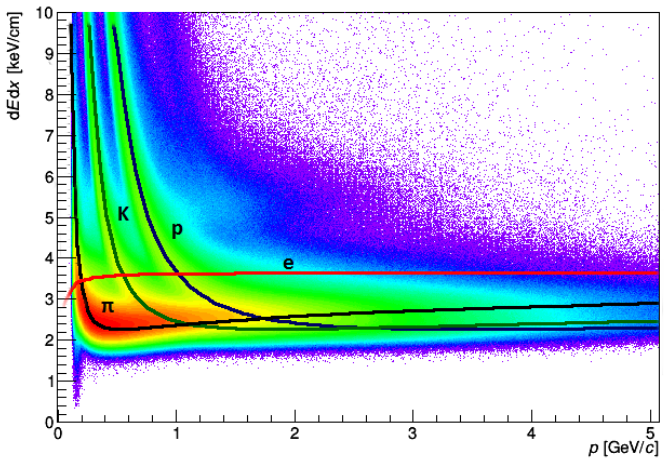

Figure 2.5: The energy loss of charged particles as a function of their momentum in 0-5% most central U+U collisions. Expected values for electrons e, pions π, kaons K and protons p obtained from Bichsel functions [71] are shown as colored curves.

2.1.2 iTPC

TPC is absolutely key component of the STAR detector which has been running since 2001. One of the most important near-term (2015-2020) upgrades of STAR is the STAR Inner Sector TPC Upgrade (iTPC). It will increase the segmentation on the inner pad plane, renew the inner sector wires and improve the boundary between inner and outer sectors. As a consequence, iTPC will provide better momentum and $\mathrm{d}E/\mathrm{d}x$ resolution as TPC in the present, e.g. kaons will be separated from protons at higher momenta and the reconstruction efficiency for strange hadrons for $p_{\mathrm{T}} < 1\mathrm{GeV}/c$ will be increased by a factor of magnitude. Figure 2.6 shows the study of reduced hadron contamination in electron

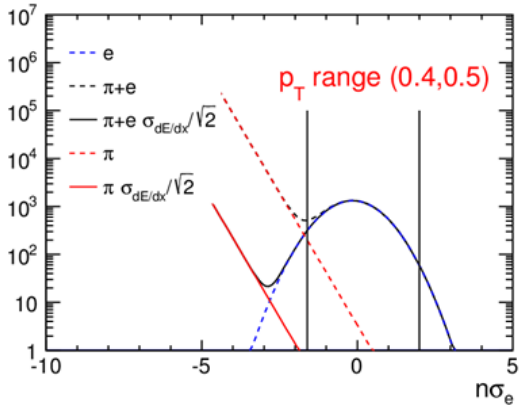

Figure 2.6: The study of reduced hadron contamination in electron selection using iTPC. $\mathrm{d}E/\mathrm{d}x$ of electrons and hadron background, as a function of $n\sigma_{\mathrm{e}}$ for $0.4 < p_{\mathrm{T}} < 0.5$ GeV/c. The blue Gaussian curve is the electron $\mathrm{d}E/\mathrm{d}x$ while the red dashed line is a fit to the measured hadron $\mathrm{d}E/\mathrm{d}x$ tail. The solid red line is the expected hadron contamination with the improved tracking of the iTPC [70].

selection using iTPC. What is also very important, iTPC will improve acceptance of

pseudorapidity to 1.5 which will turn into the increase of the measured number of charged particles and enhancement of the particle identification capabilities towards lower p_{T} to 60 MeV/c. The broadened pseudorapidity coverage could also lead to new opportunities for looking into new physics which has not been studied at STAR before [70].

2.2 Time of Flight Detector

The Time of Flight (TOF) detector extends the particle identification capabilities of the TPC. Moreover, it is also very important triggering device of the STAR detector.

TOF is in the shape of cylindrical shell around the TPC (see Figure 2.2) and covers the pseudorapidity $|\eta| < 0.9$ and full azimuthal angle.

Detector is based on Multi-gap Resistive Plate Chamber (MRPC) technology with excellent timing resolution. The same technology was later used also for the MTD detector and is briefly described in Section 1.5. TOF enables to measure the time of flight of the particle. In fact, TOF measures the "stop time" when the signal of the particle in any TOF detection pad is detected. In order to obtain the time of flight the information from STAR Vertex Position Detectors which measure the "start time" of the collision is used. Then, the time of flight is given as the difference between the stop time and start time. The TOF identification capabilities are often expressed in the words of the average value of the inverse velocity $1/\beta$ given as the ratio of the time of flight and the length s of associated track from the TPC.

Using the information from TPC about momentum p of the particle and its $1/\beta$, the mass m of the particle can be calculated according to:

$$m = \frac{p}{c}\sqrt{\left(\frac{1}{\beta}\right)^2 - 1}. \tag{2.1}$$

In the left panel of Figure 2.7 the momentum dependence of the mass resolution based on the TOF timing resolution 100 ps for protons, kaons, pions and deuterons is illustrated [73]. The right panel of Figure 2.7 shows measured $1/\beta$ as a function of particle momentum for electrons, pions, kaons, protons and deuterons. The theoretical curves are obtained using the particle masses [3] and Equation 2.1.

Together with the TPC the TOF can improve the identification of low momentum particles. It is effective in separation of electrons from heavier hadrons at low momenta to $\sim$ 1.4 GeV/c, pions and (anti)protons are identified for p up to 7-8 GeV/c, kaons to $\sim$ 3 GeV/c and electrons from 150 MeV/c to 4 GeV/c [74]. However, as can be seen from the Figure 2.7 towards the intermediate momenta the capabilities of TOF are not sufficient for particle identification – the mass bands and $1/\beta$ of different particle species overlap. For this reason information from Barrel Electromagnetic Calorimeter has to be used at higher momenta.

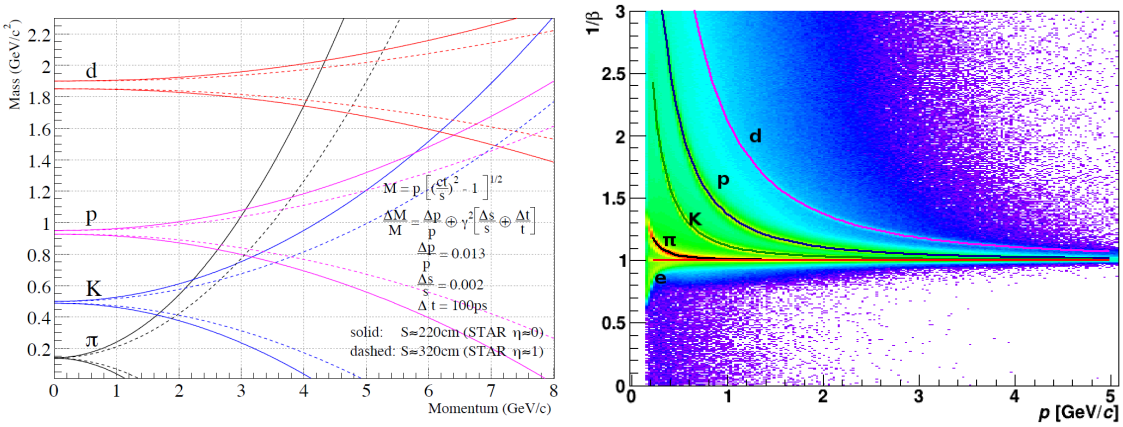

Figure 2.7: Left: The momentum dependence of the mass resolution for the total TOF resolution 100 ps for protons, kaons, pions and deuterons [73]. Right:$1/\beta$ of charged particles as a function of their momentum in 0-5% most central U+U collisions. Calculated values for electrons e, pions π, kaons K, protons p and deuterons d according to 2.1 are shown as colored curves.

2.3 Barrel Electromagnetic Calorimeter

The Barrel Electromagnetic Calorimeter (BEMC) measures energy of electromagnetic showers produced by high momentum particles. It is also used as the so called high-tower (HT) trigger.

BEMC is barrel of diameter ca. 4.4 m. It is located between the TOF detector and the STAR magnet. It covers pseudorapidity $|\eta| < 1$ and full azimuthal angle ϕ. It consists of 120 calorimeter modules of the size $\Delta\eta \times \Delta\phi \simeq 1 \times 0.1$, each of each of which is segmented into 40 towers, 2 in ϕ and 20 in η, with each tower being 0.05 in $\Delta\phi$ by 0.05 in $\Delta\eta$. The schematic drawing of the BEMC module is illustrated in the Figure 2.8. Each module consists of a lead-scintillator stack and Barrel Shower Maximum Detectors (BSMD) [75]. As high energy particles pass the layers of lead and scintillator. Lead plates are absorbers in which the particles lose energy and as a result the electromagnetic showers develop. while the role of the scintillator layers is to transform the energy of particles from shower to energy of photons and to sample this energy.

Since BEMC has a total radiation length $\sim$ 20 X_0 [75] electrons are expected to deposit their whole energy in the calorimeter while hadrons do not. Therefore, for high momentum electrons energy-to-momentum ratio E/pc (where E is energy deposited in the BEMC towers and p is momentum from TPC) is ~ 1 while for hadrons it is less than 1. So, at high momentum the BEMC towers provide electron-hadron separation via E/pc.

The role of the BSMD is to provide spatial resolution of the position and the shape of the shower. Therefore, they are located at the depth of 5 radiation lengths where the electromagnetic showers are expected to be fully developed.

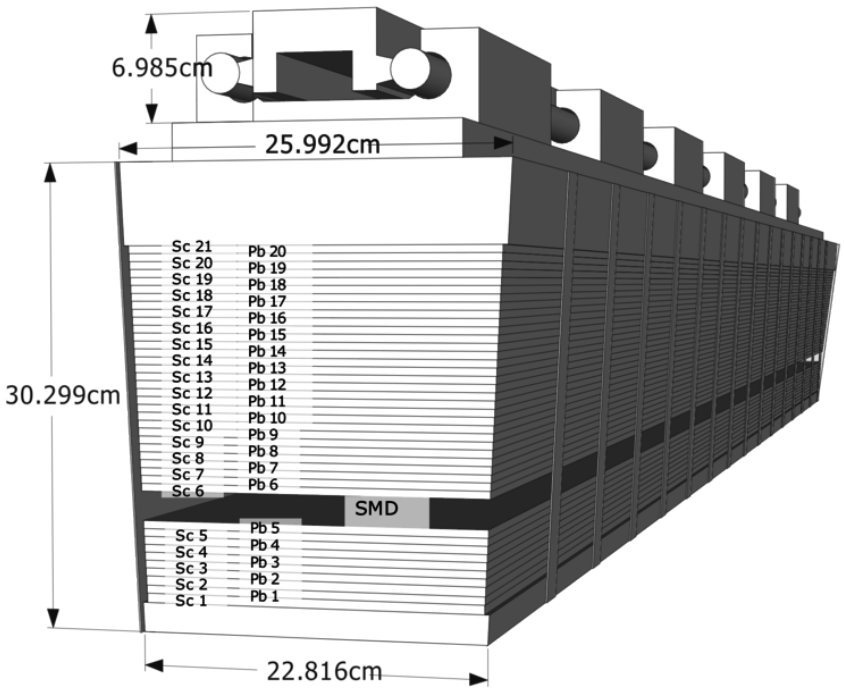

Figure 2.8: Schematic drawing of the BEMC module [76].

2.4 Heavy Flavor Tracker

The Heavy Flavor Tracker (HFT) is a key upgrade for the current STAR physics program fully installed in 2014. It significantly improves and extends capabilities of heavy flavor production measurements at STAR by measuring of displaced vertices with excellent pointing resolution. It provides the direct topological identification of open heavy flavor hadrons and enables distinguish between charm and bottom contributions [77]. In J/ψ analysis the role of HFT is in separating of contributions to the production from B-meson feed-down using the displaced vertices.

HFT is the innermost detector of STAR. It is located around the beam-pipe in the central part of the STAR detector. It consists of different subsystems: two layers of the silicon pixel detector (PIXEL) which surround the beam pipe at the distance of 2.5 cm and 7 cm respectively and the intermediate silicon tracker (IST) which consist of two barrel layers with radii of 12 cm (IST1) and 17 cm (IST2)[77]. In order to connect tracks from TPC to the HFT with good pointing resolution the STAR detector includes also the Silicon Strip Detector (SSD) located between the HFT and TPC at the distance of 22 cm from the center of the detector. The schematic drawing of the Heavy Flavor Tracker subsystems and its photograph can be seen in the Figure 2.9. The resolution of HFT's layers is also shown.

As mentioned earlier, HFT is an important upgrade of STAR for open heavy flavor measurements. Figure 2.10 shows preliminary results on reconstructed D-meson invariant mass spectrum in 2014 Au+Au collisions using HFT. With HFT the combinatorial

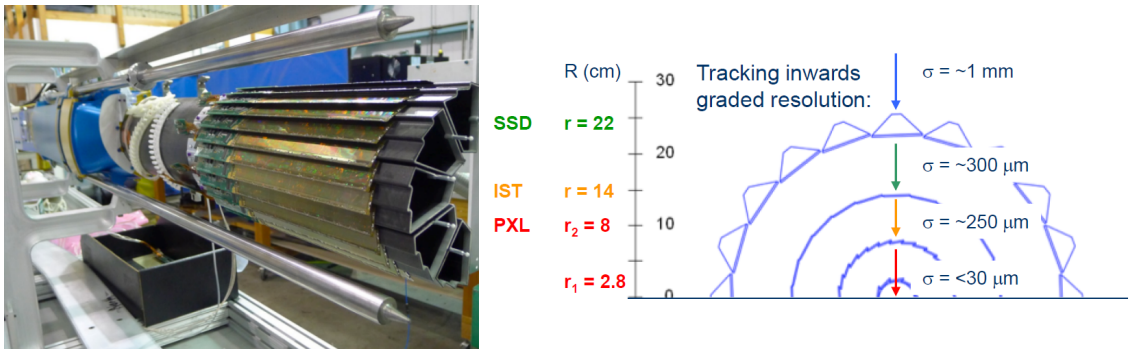

Figure 2.9: The Heavy Flavor Tracker. Left: The photograph of the HFT [78]. Right: Subsystems of the HFT and their resolution [79].

background was reduced by 4 orders of magnitude. The very first preliminary results on D^0 R_{AA} are shown in Figure 1.13. As can be seen, thanks to HFT improved precision of high p_{T} data has been achieved. Hence, HFT offers new possibilities for the STAR experiment.

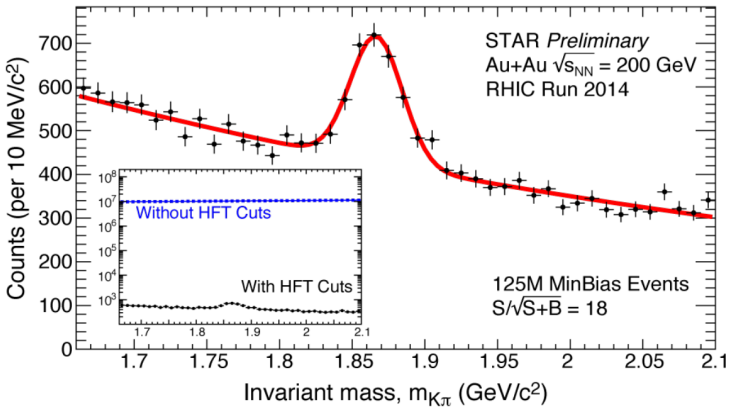

Figure 2.10: D^0 reconstruction: Invariant mass spectrum of $K\pi$ pairs from 2014 Au+Au collisions at $\sqrt{s_{\mathrm{NN}}} = 200$ GeV. For comparison the invariant mass spectrum with and without using HFT is shown.

2.5 Muon Telescope Detector

The Muon Telescope Detector (MTD) is used for triggering and identification of muons at mid-rapidity.

It is located behind the STAR magnet in the distance of ca. 400 cm from the beam pipe (see Figure 2.2). The STAR magnet, used as an hadron absorber, provides background shielding. Drawing of the MTD detector can be seen in the Figure 2.11. MTD covers 45% of the azimuth angle and the pseudorapidity $|\eta| < 0.5$.

MTD modules, basic detection blocks of MTD, are based on the Multi-gap Resistive Plate Chambers (MRPC) technology [81]. "Body" of the MRPC module consists of 6

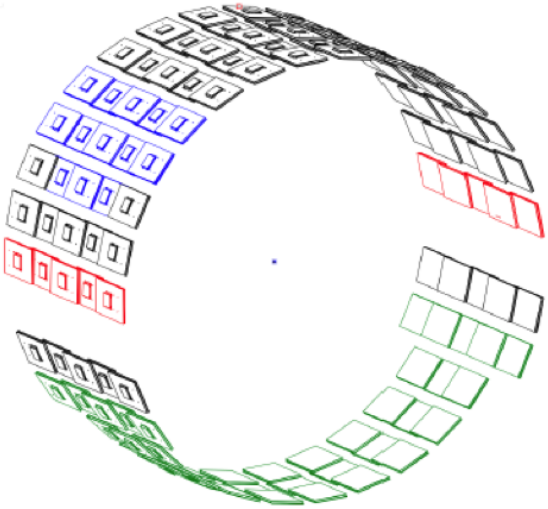

Figure 2.11: The schematic drawing of the Muon Telescope Detector [80].

resistive glass plates resulting in a total of 5 gas gaps. Gas gaps are filled with a mixture of 95% Freon and 5% Isobutane [81]. MTD MRPC module can be seen in the Figure 2.12. However, Compared to the TOF modules the MTD MRPCs are larger and have double-ended read-out strips for better resolution.

Charged particles traversing the volume of the MTD modules ionize molecules of the gas and create electron avalanches which are then detected on the anode strips. The role of the resistive glass plates is to absorb some electrons from avalanche to improve spatial resolution of the modules.

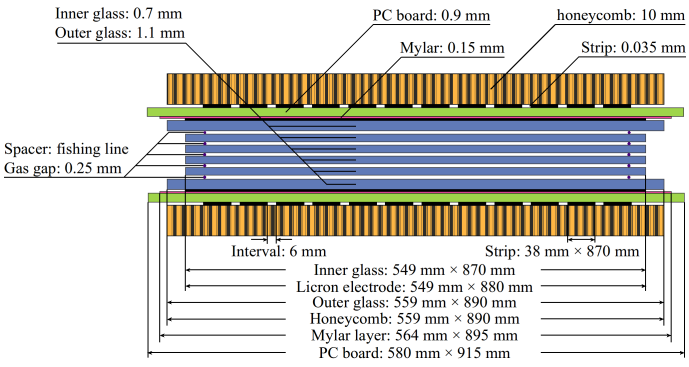

Figure 2.12: Schematic drawing of the MTD MRPC module [81].

Muons do not participate in strong interactions and, therefore, are interesting probes of the strongly-interacting quark-gluon plasma. The MTD enables detection of di-muon pairs from QGP thermal radiation, quarkonia decays or light vector meson decays. It also allows open heavy flavor measurements using semileptonic decays and electron-muon correlations. Although some of these topics can be studied through electrons or photons, the use of muons has significant advantages. Electrons have larger background from hadrons than muons. Another advantage of muons is that unlike the electrons, they are not so affected by bremsstrahlung radiation and thus can provide better mass resolution of vector mesons

and quarkonia. This is especially important for Υ since good mass resolution and low background allow to separate different Υ states [82].

Left panel of Figure 2.13 shows new preliminary results on J/ψ signal in Au+Au collisions at $\sqrt{s_{\mathrm{NN}}}$ = 200 GeV from Run 2014. reconstructed via the decay channel $J/\psi \to \mu^{-}\mu^{+}$ using MTD. Significant J/ψ peak at ~ 3.1 GeV/c^2 is observed. Left panel of Figure 2.13 shows projection on signal shapes of Υ (1S, 2S and 3S) states measured by MTD in Au+Au collisions.

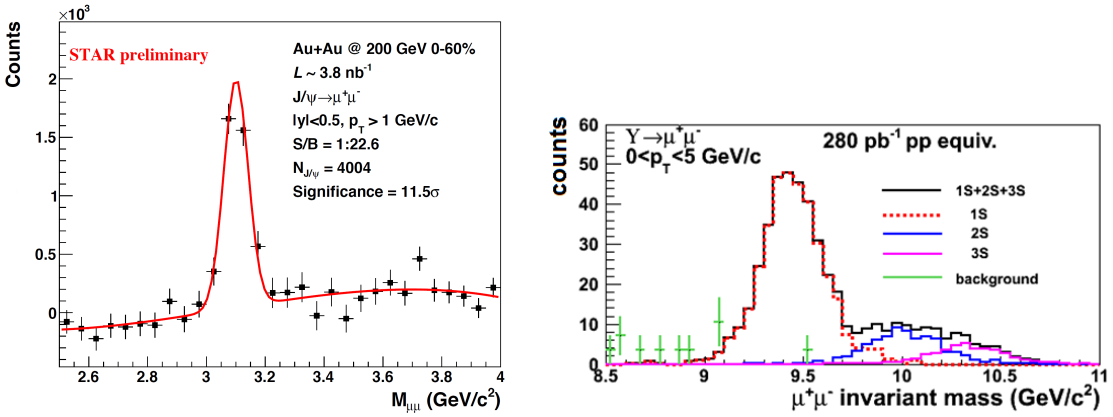

Figure 2.13: Left: J/ψ signal reconstructed using MTD [83]. Right: Projection on signal shapes of Υ (1S,2S and 3S) states measured by MTD in Au+Au collisions [84].

2.6 STAR Triggers

Triggering system of the STAR detector is a complicated system consisting of different levels of logic. In this system the signals from the fast detectors (VPD, ZDC, BBC, TOF, BEMC) are processed in bunch crossing rate 1 MHz [85] and decisions which events should be recorded and whether to "switch on" read-out of slow detectors (required primarily for tracking and particle identification, e.g. TPC) are made.

Below some important functions of selected fast detectors of the STAR triggering system are presented.

- The two lead-scintillator assemblies of **Vertex Position Detectors** (VPDs) [86] are located very close to the beam pipe ca. 5.7 m from the intersection point. Each assembly depicted in the right panel of Figure 2.14 consists of 19 detectors. A schematic side view of the detector can be seen in the right panel of Figure 2.14. The number and species of particles producing signal in the VPD depend strongly on the collision system. In Au+Au collisiosns at 200 GeV the signal is produced by fotons from π^0 decays and charged pions. In the lowest energy Au+Au collisions at 7.7 GeV a VPD hit results from one or two spectator protons [86]. The time difference between the signals of the East and the West VPD determines the primary vertex position of the collision, the time average determines the start time of the collision needed for TOF. In 200 GeV Au+Au collisions the start time resolution is few tens

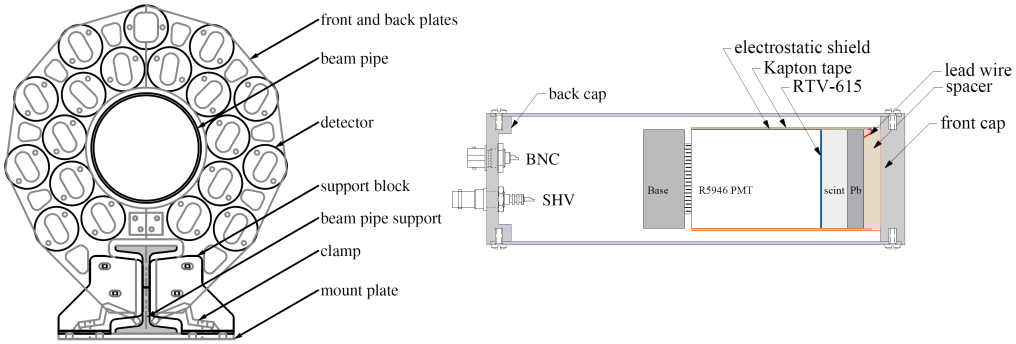

Figure 2.14: Left: A schematic view of the VPD assembly [86]. Right: A side view of the VPD detector [86].

picoseconds and the resolution of the primary vertex is 1 cm. [86]. VPDs are used as a primary minimum-bias (MB) trigger.

- The two **Beam Beam Counters** (BBCs) are located ca. 3.5 m from the intersection point of the STAR detector. They consist of two layers of hexagonal scintillator triplet blocks which surround the beam pipe. BBCs can determine the collisional vertex position and centrality, however primarily they are are used to monitor beam conditions.

- The two **Zero Degree Calorimeters** (ZDCs) are situated at 18.25 m from the intersection point outside of the RHIC magnets as illustrated in Figure 2.15. Each ZDC assembly consists of three modules. Each module consists of a series of tungsten plates alternating with layers of wavelength shifting fibers that route Čerenkov light to a photo-multiplier tube. By detecting the Čerenkov radiation the ZDCs measure the number of spectator neutrons from collisions. They are used for triggering on central collisions and for beam monitoring [87, 88].

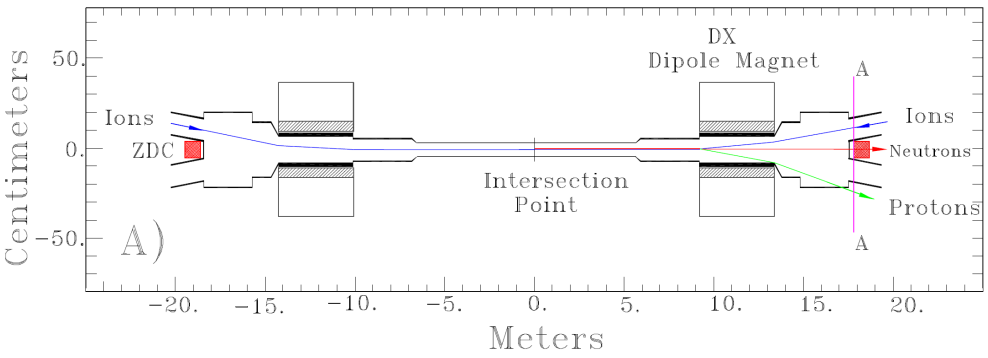

Figure 2.15: Plan view of the collision region with the location of ZDC detectors illustrated. Deflection of charged fragments and protons is indicated [87].

- The **Time Of Flight** detector is used to trigger on central collisions by requiring a high occupancy of hits.

- The **Barrel Electromagnetic Calorimeter** triggers on events with a large deposit of energy in BEMC tower or tower cluster, corresponding to the production of a jet or high p_{T} particle (HT trigger).
- The **Muon Telescope Detector** triggers on events with $\mu - \mu$ requiring at least two hits on MTD. In coincidence with TOF MTD triggers on cosmic rays [81] and in coincidence with VPDs and BEMC towers it triggers on minimum bias and $e - \mu$ events [89].

Chapter 3

Data analysis

U+U collisions are important tools for investigating hot-matter effects. It is expected that the energy density reached in central U+U collisions is the highest achievable at RHIC. Thus they provide unique conditions to study the interplay of effects of the hot medium. Information about J/ψ production modification in central U+U data can help to distinguish these different effects.

The current and following chapters describe the analysis of the author of the thesis. The work was discussed in Heavy flavor physics working group at STAR. Approved results were presented at international conferences listed in Appendix A.

This chapter focuses on the data analysis leading to the extraction of raw J/ψ signal in 0-5% most central U+U collisions at the STAR experiment is described. J/ψ was reconstructed via the electron-positron decay channel $J/\psi \rightarrow e^+e^-$ with branching ratio B.R. = (5.971 $\pm$ 0.032) % [3]). The method of J/ψ signal extraction is described as a sequence of different criteria applied on analyzed events, tracks and J/ψ daughter electron (positron) candidates.

3.1 Data and triggers

In this analysis the data taken from U+U collisions recorded at RHIC at the center-of-mass energy $\sqrt{s_{\rm NN}}$ = 193 GeV in Run 12 in year 2012 were used. Since the aim of the analysis was to study the J/ψ in central U+U collisions, only the events satisfying the 0-5% centrality triggers, namely those labeled central-5 and central-5-protected, were analyzed.

The labeling "central-5" denotes the centrality class of events which are the subject to selection. In general, the 0 - 5 % centrality triggers select the events by requiring a small signal deposited in the ZDC detectors as well as a large multiplicity from the barrel TOF.

Attribute "protected" means that there is an algorithm that looks at the past and future history of information in the trigger detectors (BBC hits, ZDC energy, TOF hits) to reduce (but not able to completely remove) additional occupancy in the TPC caused by pile-up of other events in the 40 μs readout time. Pile-ups originate from the processes when there is higher frequency of collisions than TPC read-out frequency. As a result,

tracks from multiple events are read out at the same time and considered as single event. The information that we deal with the multiple event can be obtained when multiple vertices of seemingly single collision are reconstructed.

Using the central triggers ca. 115 M events were selected and these were used for further studies. Figure 3.1 shows the multiplicity distribution of events used in this analysis.

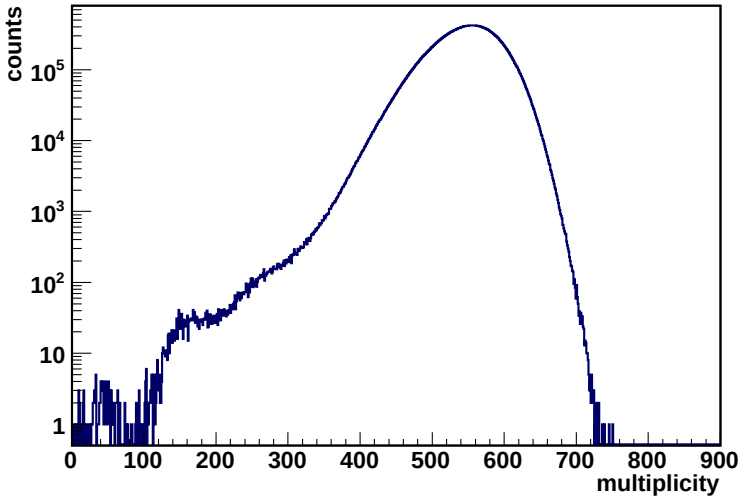

Figure 3.1: Multiplicity distribution of 0-5% most central events according to TOF+ZDC central triggers.

3.2 Centrality determination

Since the overlap of the colliding nuclei cannot be measured directly the centrality selection of the collisions is determined from a Monte Carlo Glauber simulation [53]. Each collision is simulated as a function of nuclear overlap (centrality) to which a number of nucleons participating in collisions N_{part} and a number of binary nucleon-nucleon collisions N_{bin} and charged particle multiplicity are related. Results of such study in minimum-bias U+U collisions can be seen in Table 3.1. In minimum-bias U+U collisions, the measured particle multiplicities in the TPC are compared to the values from the Glauber model in the second column of Table 3.1 and the centralities, N_{part} and N_{bin} of analyzed events are determined.

However, in the analysis presented in this work, the central triggered 0 - 5 % most central U+U collisions are selected by a different detector, i.e. ZDC+TOF, as opposed to the minimum-bias data where the centrality is based on the measured particle multiplicity in TPC. Consequently, the multiplicity distribution of central triggered U+U data shown in Figure 3.1 does not fully match the distribution of multiplicity based 0 - 5 % most central minimum-bias U+U collisions. There is a fraction of central triggered events which, based on their multiplicity and the data in Table 3.1, belong to other centralities (5 - 10 %, 10 - 15 %, ...).

Therefore, analogous study of relation between centrality, measured particle multiplic-

Centrality boundary	**Multiplicity**	$N_{\mathbf{bin}}$	$N_{\mathbf{part}}$
5%	> 535	1281.26	414.873
10%	> 466	1010.97	355.421
15%	> 399	798.527	300.918
20%	> 339	628.011	253.662
25%	> 283	490.596	212.842
30%	> 233	379.861	177.481
35%	> 189	290.308	146.781
40%	> 151	217.353	119.633
45%	> 118	160.027	96.3434
50%	> 91	115.689	76.4301
55%	> 68	81.7581	59.5496
60%	> 50	56.9773	45.7347
65%	> 35	38.3629	34.0142
70%	> 24	25.0591	24.5462
75%	> 16	16.2799	17.4621
80%	> 10	10.2311	11.9753

Table 3.1: Centrality classes and corresponding multiplicity ranges, number of binary nucleon-nucleon collisions N_{bin} and number of participant nucleons N_{part} in minimum-bias U+U collisions [90].

ity, N_{bin} and N_{part} in ZDC+TOF triggered data as for minimum-bias events is needed for precise interpretation of results. Unfortunately, it has not been performed yet and its realization is beyond the scope of this thesis.

Temporarily, N_{bin} in central triggered data was determined by weighting

$$N_{\text{bin}} \approx N_{\text{bin}}^{0-5\ \%}\omega^{0-5\ \%} + N_{\text{bin}}^{5-10\ \%}\omega^{5-10\ \%} + ... \tag{3.1}$$

where $N_{\text{bin}}^{i-j\ \%}$ denotes the number of binary nucleon-nucleon collisions for centrality i - j % according to Table 3.1 and $\omega^{i-j\ \%}$ gives the number of ZDC+TOF triggered events in multiplicity based centrality bin i - j % from Table 3.1. Approximation of N_{part} was derived in a similar way. The approach led to $N_{\text{bin}} \approx 1172$ and $N_{\text{part}} \approx 390$. Systematic uncertainty of N_{bin} and N_{part} was taken as a difference between weighted values and the values from Table 3.1.

3.3 Event selection

In further analysis only those events for which the longitudinal distance (i.e. the distance in the direction of the z-axis) between the z-coordinate of their primary vertex reconstructed as an intersection point of the TPC tracks ${v_Z}^{\mathrm{TPC}}$ and the center of the detector (${v_Z}^{\mathrm{TPC}}$) was lower than 30 cm were selected (shown in the left panel of Figure 3.2). This requirement was used to ensure that the efficiency of reconstruction will not depend on v_Z. Thus, only collisions in the center of the detector were analyzed.

As described in Section 2.6 the primary vertex can be determined also by the VPDs (v_Z^{VPD}). To remove the pile-ups only the events for which $|v_Z^{\mathrm{TPC}} - v_Z^{\mathrm{VPD}}| < 3$ cm (see right panel of Figure 3.2) were analyzed. Applying the event cuts the number of analyzed events was reduced to ~ 56 M.

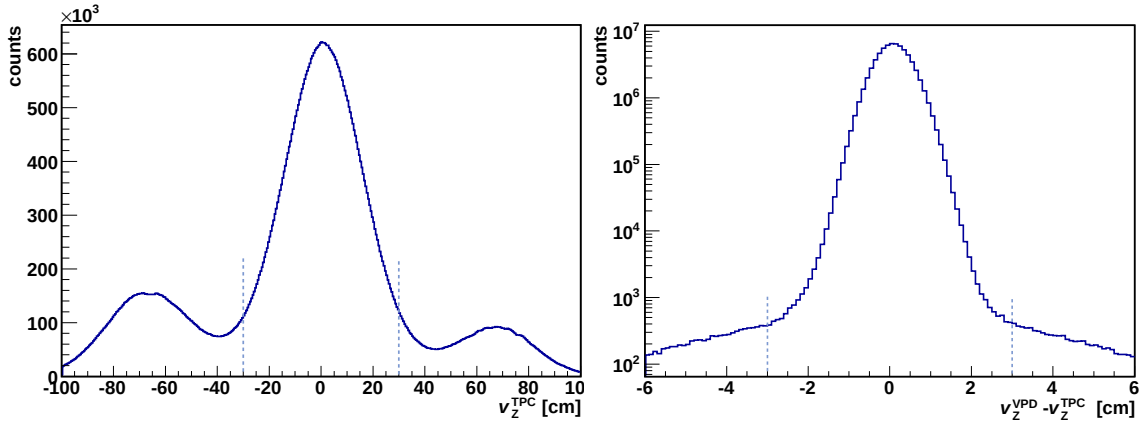

Figure 3.2: Left: ${v_Z}^{\mathrm{TPC}}$ distribution of analyzed events before the v_Z^{TPC} cut. Dashed lines denote the applied cut. Right: $v_Z^{\mathrm{TPC}} - v_Z^{\mathrm{VPD}}$ distribution of analyzed events after v_Z^{TPC} cut. Dashed lines denote the $v_Z^{\mathrm{TPC}} - v_Z^{\mathrm{VPD}}$ cut.

3.4 Track selection

In the analyzed events J/ψ daughter electrons (positrons) were selected from the so-called primary tracks.

In addition to global tracks which are obtained from fitting the hits in the TPC, the primary tracks are reconstructed by refitting the hits in the TPC taking also the collision vertex into account as a fit point. In other words we require the track to originate in (or very close to) the primary vertex. This requirement comes from the very short lifetime of J/ψ which is $\approx 7.10^{-20}$ s [3] so J/ψ is not expected to travel far from the primary vertex before it decays into e.g. daughter electrons. Hence, the primary tracks are considered to perform good description of J/ψ daughter electrons (positrons). All requirements on primary tracks are summarized in Table 3.2 in Section 1.7.

3.4.1 Track quality requirements

In this analysis the primary tracks were selected according to the following quality requirements:

- The distance of the closest approach (DCA) of the track to the primary vertex of the event had to be less than 3 cm.
- Particle trajectories are reconstructed by fitting the hits on the TPC pads. To ensure good quality of reconstructed tracks the minimum number of reconstructed hits in TPC was required to be 20.
- The ratio of fitted hits to all possible hits (maximum number of hit points) on the TPC pads had to be larger than 0.51. This requirement was used to remove split tracks (misidentified as different tracks) which decrease the considered ratio.

3.4.2 Kinematic requirements - p_{T} cut

Following kinematic requirements on electron candidates were also used:

- Only tracks with pseudorapidity $\eta < 1.0$ were accepted. This requirement is based on the acceptance of the TPC.

- We required the p_{T} of the primary tracks to be above 0.2 GeV/c in order to reach the outer radius of the TPC.

- In addition to the previously mentioned requirements on primary tracks only the electrons (positrons) with transverse momenta above 1.0 GeV/c were accepted for the analysis of J/ψ signal. For the analysis of photonic electrons described in Section 4.1.2 this requirement was not used.

  The p_{T} cut was motivated by the shape of the p_{T} distribution of J/ψ daughter electrons (positrons) illustrated in the Figure 3.3 for Monte Carlo simulated events. From the left panel of Figure 3.3 it can be seen that there is only a small fraction of J/ψ decays into electrons (positrons) with p_{T} below $\sim$ 0.8 GeV/c. Moreover, this low-p_{T} fraction is often "hidden" in the bakground contribution of electrons (positrons) originating from different processes than J/ψ decay. The exact value of the p_{T} cut > 1.0 GeV/c was chosen according to the J/ψ signal significance studies using different p_{T} cuts in the range $(0.6 - 1.4)$ GeV/c. The chosen p_{T} cut is also shown on Monte Carlo simulated events $J/\psi \to e^+e^-$ in the right panel of Figure 3.3. It illustrates the fraction of electrons (positrons) lost by the p_{T} cut. In the overall effect the p_{T} cut greatly improves the significance of the signal.

3.5 Electron identification

From the primary tracks satisfying criteria described above J/ψ daughter electron (positron) candidates were selected. The electron (positron) candidates had to fulfill cuts on TPC, TOF and BEMC signal described in following sections.

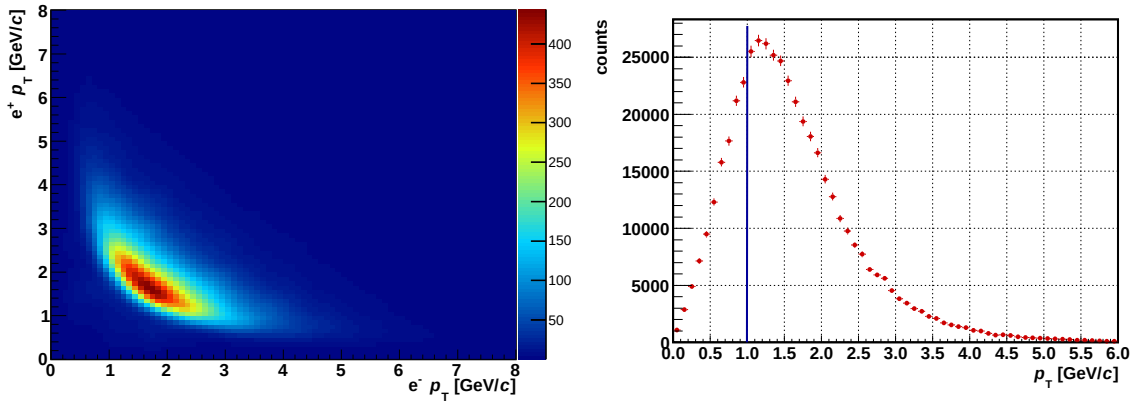

Figure 3.3: Left: Monte Carlo simulated p_{T} distribution of electrons and positrons from J/ψ decay integrated over J/ψ $p_{\mathrm{T}} = (0-10)$ GeV/c. Right: p_{T} distribution of electrons from J/ψ decay integrated over J/ψ $p_{\mathrm{T}} = (0-10)$ GeV/c. The used p_{T} cut is shown as a red line.

3.5.1 TPC cut

TPC provides identification of charged particles according to their specific energy loss dE/dx in the TPC gas. Figure 2.5 shows measured energy loss of different particle species and their expected mean energy loss given by Bichsel functions [71]. The electron (positron) data sample was selected using only those tracks for which their dE/dx fluctuates around the corresponding theoretical value dE/dx_{Bichsel}. This method of selection is connected with the variable $n\sigma_{\mathrm{e}}$ which gives dE/dx normalized to dE/dx_{Bichsel} for electrons in the logarithm and scaled by the dE/dx resolution $\sigma_{dE/dx}$:

$$n\sigma_{\mathrm{e}} = ln\left(\frac{dE/dx}{dE/dx_{\mathrm{Bichsel}}}\right)/\sigma_{dE/dx} \tag{3.2}$$

In the J/ψ analysis $n\sigma_{\mathrm{e}}$ was required to be in the range between -1.5 and 2.0. The asymmetric cut was applied in order to decrease the contamination from pions at negative $n\sigma_{\mathrm{e}}$ which can be seen in Figure 3.4. TPC $n\sigma_{\mathrm{e}}$ cut was required for all electron (positron) candidates.

3.5.2 TOF cut

As can be seen in the Figure 2.5 areas of specific energy loss of electrons, pions and protons overlap towards intermediate momenta and particle identification using only TPC is not efficient anymore. Therefore, the TOF detector is used to distinguish different particle species in this region. For low momenta particles $1/\beta$ measured by TOF is ~ 1 for electrons while it is > 1 for hadrons. Towards higher momenta ($p > 1.4$ GeV/c) $1/\beta$ of e, π, p, K, d approaches to 1 and it is not possible to select the electrons only with the TOF detector. The information from BEMC has to be used.

In our analysis the TOF cut was applied as follows: if $p < 1.4$ GeV/c we required electron candidates to have a valid TOF signal, i.e. we required TOFMatchFlag > 0 and $|y_{\mathrm{local}}| < 1.8$ cm where y_{local} is distance of the track projection and the center of TOF pad

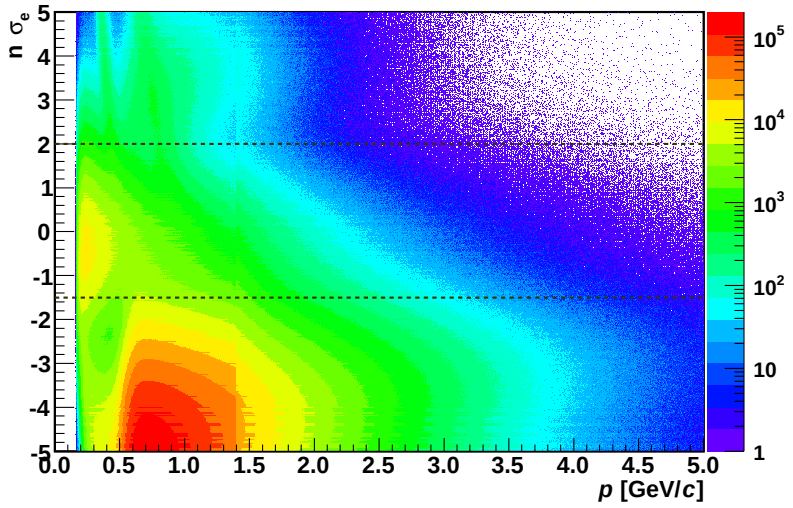

Figure 3.4: $n\sigma_{\mathrm{e}}$ of tracks satisfying primary track quality requirements, TOF and BEMC cuts. Black dashed lines denote the $n\sigma_{\mathrm{e}}$ cut.

and $1/\beta$ to be in the range from 0.970 to 1.025.

For particles with momenta higher than 1.4 GeV/c TOF was used as veto. Particle was accepted if it did not have the signal in TOF. On the other hand, if particle had a good signal in TOF but $1/\beta$ was not in the required range it was not accepted.

Figure 3.5 shows $1/\beta$ of tracks which satisfy primary track quality requirements, TPC and BEMC cut. The lines on the plot illustrate the TOF cut.

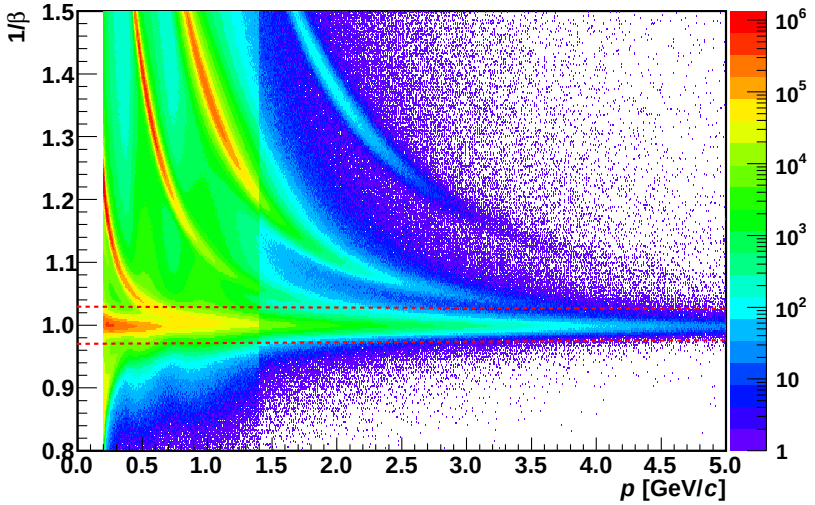

Figure 3.5: $1/\beta$ of particles which satisfy TPC and BEMC cuts. Red dashed lines on the plot illustrate the TOF cut.

3.5.3 BEMC cut

To identify particles of momenta higher than 1.4GeV/c the BEMC is needed. BEMC can distinguish between electrons and hadrons with higher momenta according to the ratio pc/E (E is deposited energy in the BEMC tower, p is the momentum of the particle required by TPC) which should be ~ 1 for electrons and > 1 for hadrons. However, different effects (leakage/gain of the energy to/from neighboring towers) modify this ratio. Thus the electron candidates were required to deposit energy $E > 0.15$ GeV in the highest energy BEMC tower and satisfy the criterion: $0.7 < pc/E < 2.0$. The distribution of pc/E of electron candidates satisfying track quality, TPC and TOF cuts is shown in Figure 3.6.

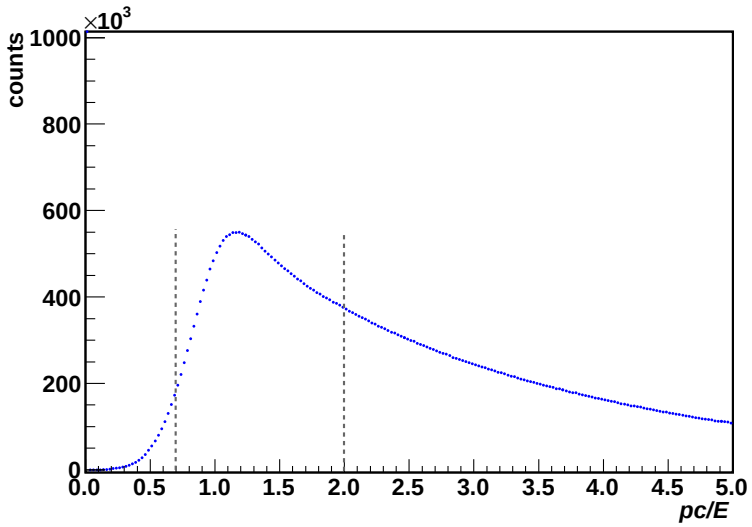

Figure 3.6: pc/E of particles which satisfy track quality requirements, TPC and TOF cuts. Dashed lines illustrate the BEMC cut.

3.6 Summary of selection criteria in J/ψ analysis in 0–5% central U+U collisions

All the selection criteria on events, primary tracks and electron(positron) candidates from J/ψ decays which were described in more detail in previous sections are summarized in Table 3.2.

3.7 Raw J/ψ yield

J/ψ signal was reconstructed from the decay of J/ψ mesons into e^-e^+ pairs. To find the J/ψ signal each electron candidate was combined with each positron candidate satisfying electron cuts described in previous sections. The invariant mass of electron-positron pairs was calculated according to the formula

$$M_{\text{inv}} = \sqrt{2p_1p_2(1 - \cos\,\alpha)} \tag{3.3}$$

Event cuts		$\lvert v_{\mathrm{Z}}^{\mathrm{TPC}}\rvert < 30$ cm
		$\lvert v_{\mathrm{Z}}^{\mathrm{TPC}} - v_{\mathrm{Z}}^{\mathrm{VPD}}\rvert < 3$ cm
Track quality requirements		$\lvert DCA\rvert < 3$ cm
		nHitsFit > 19
		$\frac{\mathrm{nHitsFit}}{\mathrm{nPossibleHits}} > 51$
Kinematic requirements		$\lvert\eta\rvert < 1$
		$p_{\mathrm{T}} > 0.2$ GeV/c
	(J/ψ signal extraction)	$p_{\mathrm{T}} > 1.0$ GeV/c
Electron cuts		$-1.5 < n\,\sigma_{\mathrm{e}} < 2.0$
	for $p < 1.4$ GeV/c:	$0.970 < 1/\beta < 1.025$
	for $p > 1.4$ GeV/c:	$E > 0.15$ GeV
		$0.7 < pc/E < 2.0$
		if $\mathrm{TOF}_{\mathrm{MatchFlag}} > 0$ and $\lvert y_{\mathrm{local}}\rvert < 1.8$ cm:
		$0.970 < 1/\beta < 1.025$

Table 3.2: Event, track and electron selection criteria in J/ψ analysis in 0–5% central U+U collisions.

where p_1 and p_2 are momenta of electron(positron) candidates and α is the angle between p_1 and p_2. We used cut on J/ψ rapidity: $-1 < y < 1$ to analyze the signal only at mid-rapidity.

However, the created e^-e^+ pairs contain not only the pairs coming from J/ψ decay but also randomly paired e^-e^+. These represent significant combinatorial background needed to be subtracted. Two methods of combinatorial background estimation were used in this analysis:

- **Like-sign background** - the like-sign pairs (e^-e^- and e^+e^+) were combined within the same events and invariant mass of these pairs was calculated.
- **Mixed event background** - we combined electrons and positrons from different events with similar event conditions which were multiplicity and primary vertex position. Events were divided into 10 multiplicity and 20 v_{Z} bins. For each multiplicity and v_{Z} bin the combinatorial background was calculated combining each e^+ from one event with each e^- from the other event always at least 10 events were mixed. Mixed event background was then normalized to the like-sign background in the invariant mass region (2.0, 3.6) GeV/c^2 around J/ψ invariant mass peak. This method of combinatorial background subtraction enables us to increase the statistics (decrease the statistical error of the background) compared with like-sign method.

Both methods of combinatorial background subtraction were tested in studied J/ψ p_{T} bins. Figure 3.7 shows the invariant mass spectra of e^-e^+ unlike-sign pairs, mixed events pairs and e^-e^-, e^+e^+ like-sign pairs used in the J/ψ signal studies in 0-5% most central U+U collisions for J/ψ p_{T} integrated. As can be seen, there is a visible peak in the region

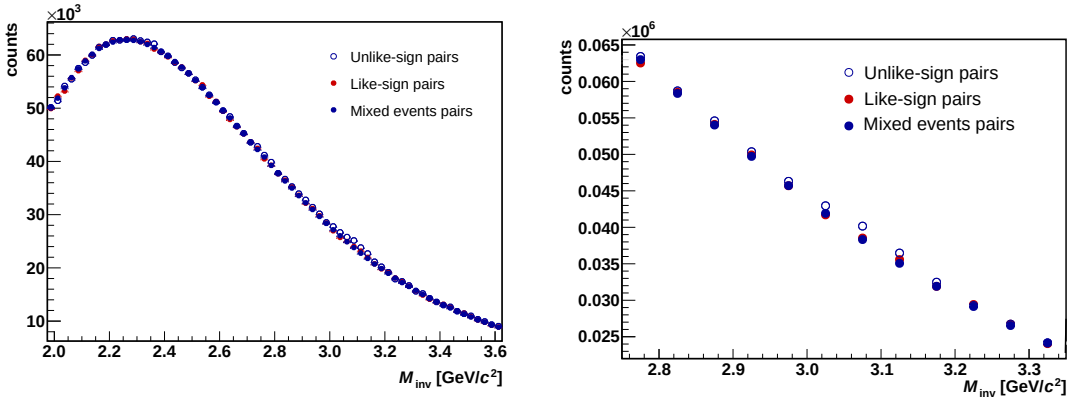

Figure 3.7: Left: The invariant mass spectra of e^+e^- unlike-sign pairs, mixed events pairs and like-sign pairs in 0 - 5 % most central U+U collisions. Right: Zoom on the region around J/ψ mass peak.

around J/ψ invariant mass.

Four panels of Figure 3.8 show the invariant mass spectra of e^+e^- pairs after like-sign and mixed events background subtraction in different J/ψ p_{T} bins. As can be seen, the invariant mass spectra obtained from mixed events method are similar to the like-sign subtracted spectra. However, compared with the like-sign subtracted spectra, they show smaller fluctuations in the mass window outside the mass peak and, as already mentioned, have smaller statistical errors.

Due to its advantages mentioned above only the mixed event background was used for the description of the combinatorial background for the rest of the analysis. However, even after the subtraction of the combinatorial background the so called residual background still remains. Therefore the invariant mass shape was fitted with the Crystal ball function [91] to describe the signal shape and the linear function (in notation used here with the constant term P_0 and slope P_1) to describe the residual background. Other functions such as second and third degree polynomials and exponential function were also used for residual background fitting (as illustrated in Figure 5.1). However, the best agreement with data was achieved with the linear function. The Crystal ball function is similar to a Gaussian function but it has a power-low tail which is used to describe the asymmetry of the peak. This can be caused by the bremsstrahlung of J/ψ daughter electrons (positrons) which are reconstructed with lower invariant mass. The Crystal ball function can be expressed as [91]:

$$f_{CB}(m) = \begin{cases} \frac{N}{\sqrt{2\pi}\sigma} \exp\left(-\frac{(m-m_0)^2}{2\sigma^2}\right), & \text{for } \frac{m-m_0}{\sigma} > -\alpha; \\ \frac{N}{\sqrt{2\pi}\sigma} \left(\frac{n}{|\alpha|}\right)^n \exp\left(-\frac{|\alpha|^2}{2}\right) \left(\frac{n}{|\alpha|} - |\alpha| - \frac{m-m_0}{\sigma}\right)^{-n}, & \text{for } \frac{m-m_0}{\sigma} \leq -\alpha. \end{cases} \tag{3.4}$$

N is the normalization constant, m_0 is common mean (in this case J/ψ invariant mass), σ is variance, α defines the transition between the Gaussian and the power-law functions and n describes an exponent of the power law tail [91].

Figure 3.9 shows the J/ψ invariant mass peaks and fitting functions for three J/ψ p_{T} bins: 0 - 1 GeV/c, 1 - 3 GeV/c, 3 - 7 GeV/c and for J/ψ p_{T} integrated in 0 - 5 %

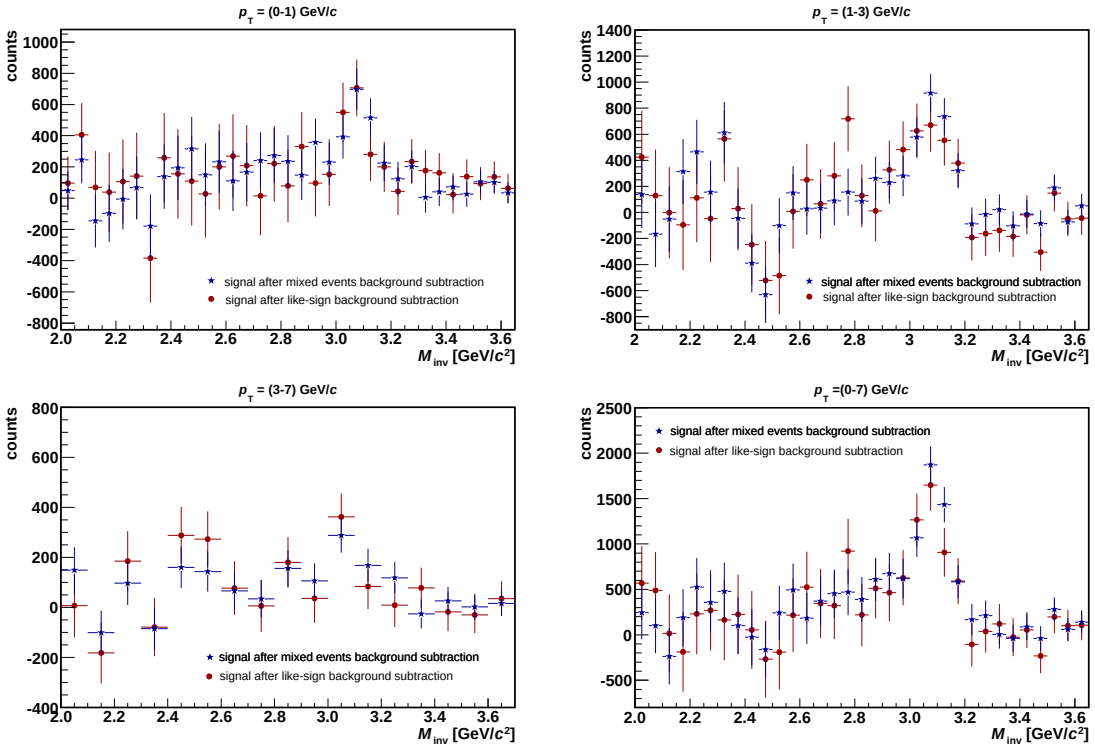

Figure 3.8: J/ψ signal after mixed events background (blue stars) and like-sign background (red circles) subtraction for J/ψ p_{T} 0 - 1 GeV/c, 1 - 3 GeV/c, 3 - 7 GeV/c and for J/ψ p_{T} 0 - 7 GeV/c integrated.

most central U+U collisions. While at lower transverse momenta clear J/ψ peak can be observed for p_{T} = 3 - 7 GeV/c the signal peak is small. In general, the data points have large statistical errors, significant fluctuations of the residual are observed and this affects the quality of the fit. The fitting of the peak serves mainly to estimate the residual background.

Raw J/ψ yield was calculated by the bin counting in the invariant mass region (2.9-3.2) GeV/c^2 after subtracting the residual background obtained from the fit. This range was used in order to include substantial part of the yield smeared towards lower invariant mass.

Significance s of the J/ψ signal can be calculated as

$$s = \frac{S}{\sqrt{S+B}} = \frac{S}{\sigma_{\mathrm{S}}} \tag{3.5}$$

where S is the number of J/ψs in given invariant mass range, σ_{S} its error and B is the background (combinatorial+residual) in the same region.

Table 3.3 shows an overview of J/ψ raw yields in different J/ψ p_{T} bins and for J/ψ p_{T} integrated, its error and corresponding significance. J/ψ raw yield error was calculated as the error of the bin counting combined with the integral error of residual background.

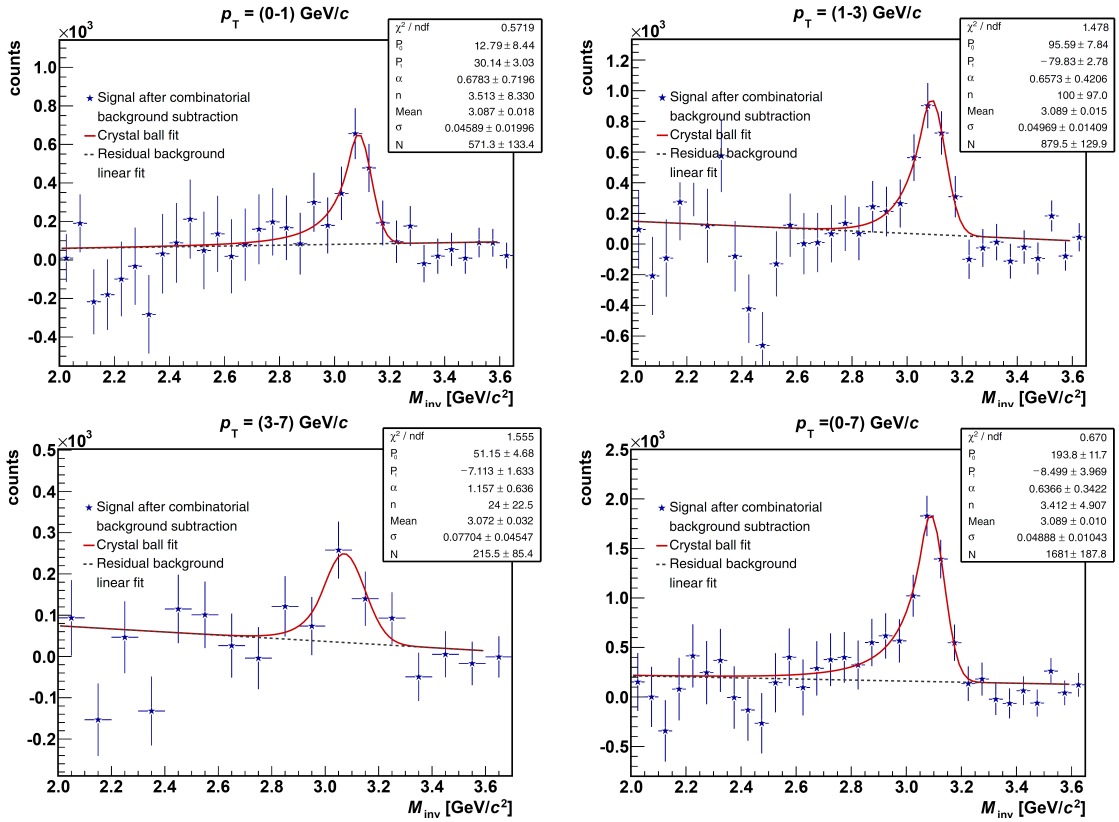

Figure 3.9: J/ψ signal after combinatorial background subtraction for for J/ψ p_{T} 0 - 1 GeV/c, 1 - 3 GeV/c, 3 - 7 GeV/c and for J/ψ p_{T} 0 - 7 GeV/c integrated. Signal is fitted with the Crystal Ball function, residual background with the linear function.

p_{T} [GeV/c]	Raw yield	Error	Significance
0–1	1660	370	4.5
1–3	2750	400	6.8
3–7	450	140	3.2
0–7	4790	560	8.6

Table 3.3: Raw yield, error of the raw yield and significance of the J/ψ signal for different J/ψ p_{T} bins.

Chapter 4

Signal corrections

By setting the requirements on electron (positron) signal in TPC, TOF and BEMC and the cut on J/ψ invariant mass window only a fraction of J/ψ produced in central U+U collisions is reconstructed.

Therefore, to calculate the J/ψ invariant yield in central U+U collisions the correction of J/ψ raw yield on the number of J/ψ which did not fulfill the different signal requirements is needed.

In this chapter J/ψ signal corrections are described and quantified by corresponding acceptance and efficiency factors.

4.1 J/ψ reconstruction efficiency

J/ψ reconstruction efficiency ϵ_{reco} quantifies the estimated fraction of J/ψ raw yield reconstructed in this analysis out of the number of J/ψ produced in studied U+U collisions. ϵ_{reco} can be expressed as function of J/ψ p_{T} by the formula:

$$\epsilon_{\text{reco}}(p_{\text{T}}) = \epsilon_{\text{folded}}(p_{\text{T}}) \times \epsilon_{\text{count}}(p_{\text{T}}) \tag{4.1}$$

where given terms denote contributions to signal corrections: J/ψ folded reconstruction efficiency ϵ_{folded} and signal counting correction ϵ_{count} which includes correction on the number of J/ψ reconstructed outside the range of the J/ψ invariant mass cut and the correction on bremsstrahlung of electrons (positrons).

J/ψ folded reconstruction efficiency can be further expressed as:

$$\epsilon_{\text{folded}}(p_{\text{T}}) = \epsilon_{\text{geom} \times \text{acc}}(p_{\text{T}}) \times \sum_{p_1,p_2} \epsilon_{\text{e}^-}(p_1) \times \epsilon_{\text{e}^+}(p_2) \times \omega(p_{\text{T}}, p_1, p_2) \tag{4.2}$$

where $\epsilon_{\text{geom} \times \text{acc}}$ is the J/ψ TPC tracking efficiency and geometrical acceptance, and ϵ_{e^-} (ϵ_{e^+}) is the efficiency of J/ψ decay electron (positron) identification and $\omega(p_{\text{T}}, p_1, p_2)$ is the weighting factor. $\omega(p_{\text{T}}, p_1, p_2)$ denotes the ratio of J/ψs with transverse momenta in given p_{T} bin with daughter electrons and positrons with momenta in bins p_1 and p_2 to all of J/ψ. $\omega(p_{\text{T}}, p_1, p_2)$ was estimated from the simulation which is described in following section. It was not estimated from data since J/ψ were analyzed using the requirement

$p_T > 1.0$ GeV/c on daughter electrons (positrons) which was included in calculation of $\epsilon_{\text{geom} \times \text{acc}}$ (it could not be counted twice).

All the contributions to J/ψ reconstruction efficiency mentioned above are described in more detail in following sections.

4.1.1 TPC tracking efficiency and geometrical acceptance

TPC tracking efficiency and geometrical acceptance was determined from simulation. Monte Carlo simulated J/ψ were embedded into real events and the interaction of daughter electrons (positrons) with detector material was studied using the GEANT simulation. Then the same TPC track quality and acceptance requirements were used on simulated sample as on real tracks described in Section 1.4.

Since the embedding for J/ψ in central U+U collisions was not produced at the time when this thesis was finalized, temporarily, the embedding for J/ψ in Run 11 0 - 5 % most central Au+Au collisions at 200 GeV was used in the analysis. The corresponding systematic uncertainty coming from using Au+Au embedding in U+U analysis is discussed in Chapter 5.

In order to shorten the computing time, p_T and rapidity spectra of simulated J/ψ were produced as flat. To make the shape of these distributions more realistic the p_T spectrum was weighted by experimentally obtained function [31]

$$\frac{dN}{dp_T} = \frac{A}{(1 + (p_T/b)^2)^n}. \tag{4.3}$$

This shape was used for the description of J/ψ p_T spectrum in 200 GeV p+p collisions at PHENIX [31]. A is normalization factor, b and n are parameters from [31]. In addition, J/ψ y spectrum was weighted with the analyzed J/ψ y distribution from real data. Figure 4.1 shows the comparison of flat input and weighted p_T and y spectra. The weighted spectra are normalized to the input spectra.

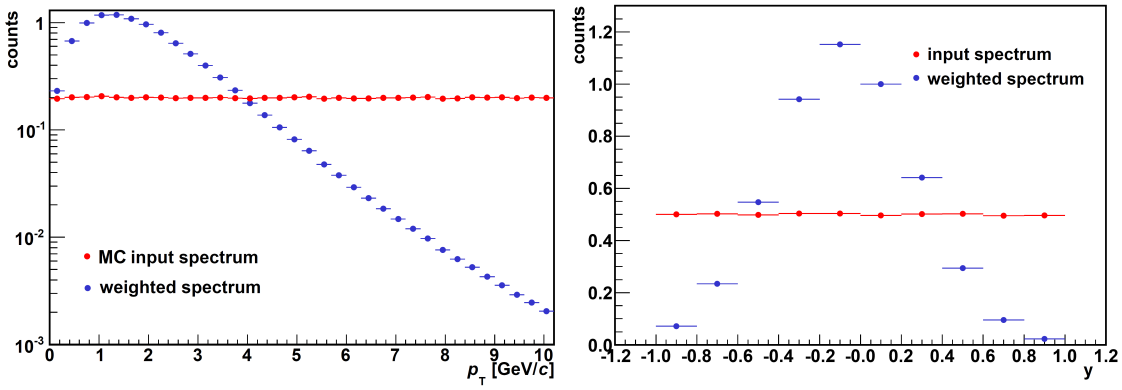

Figure 4.1: Left: Flat input and weighted simulated J/ψ p_T spectra (left panel) and y spectra. Weighted spectra are normalized to flat spectra.

As mentioned above the simulated electron (positron) daughters of the embedded J/ψ that were accepted by the TPC geometry were reconstructed using the same track quality

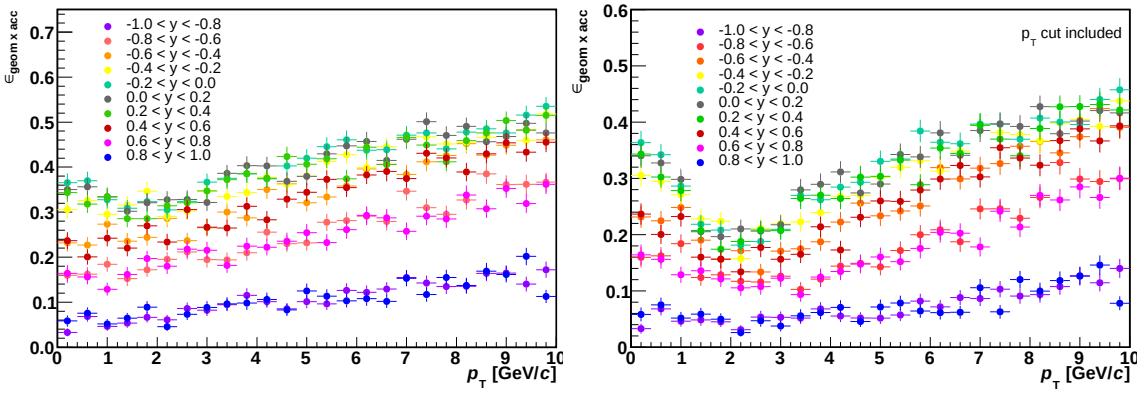

Figure 4.2: TPC tracking efficiency $\epsilon_{\text{geom}\times\text{acc}}$ as a function of J/ψ p_{T} in different rapidity bins before (left) and after (right) p_{T} cut on daughter electrons.

requirements as the real data. TPC tracking efficiency and geometrical acceptance was then calculated as the ratio of the number of reconstructed embedded J/ψ to the number of Monte Carlo simulated J/ψ. Two panels of Figure 4.2 show the TPC tracking efficiency as a function of J/ψ p_{T} in different rapidity bins. To illustrate the effect of $p_{\text{T}} > 1$ GeV/c cut applied on daughter electrons (positrons) the left panel of Figure 4.2 shows $\epsilon_{\text{geom}\times\text{acc}}$ before the p_{T} cut applied while the right panel shows $\epsilon_{\text{geom}\times\text{acc}}$ with the p_{T} cut included. As can be seen p_{T} cut systematically decreased $\epsilon_{\text{geom}\times\text{acc}}$. The effect is the most significant for J/ψ with $p_{\text{T}} \approx 1 - 3$ GeV/c and $-0.4 < y < 0.4$.

4.1.2 Single electron identification efficiency

The efficiency of single electron identification covers detector cut efficiency − since different cuts on TPC, TOF and BEMC signal were used only some fraction of electrons was accepted − and matching efficiency − which represents probability that the track leaves signal in the detector (TOF or BEMC).

Resulting efficiency of single electron identification ϵ_{e} includes all mentioned efficiencies and can be expressed as

$$\epsilon_{\text{e}} = \begin{cases} \epsilon_{\text{TPCcut}} \times \epsilon_{\text{TOFcut}} \times \epsilon_{\text{TOFmatch}} & \text{for } p \leq 1.4\text{GeV}/c; \\ \epsilon_{\text{TPCcut}} \times [\epsilon_{\text{TOFcut}} \times \epsilon_{\text{TOFmatch}} + (1 - \epsilon_{\text{TOFmatch}})] \times \epsilon_{\text{BEMCcut}} \times \epsilon_{\text{BEMCmatch}} & \text{for } p > 1.4\text{GeV}/c. \end{cases} \tag{4.4}$$

Since different selection criteria depending on momentum of electrons were used in J/ψ signal extraction two formulas in Equation 4.4 according to which ϵ_{e} was calculated.

In order to calculate single electron identification efficiency from data we need to select pure electron data sample without hadron contamination (in an ideal case). For this purpose pairs of photonic electrons (which come from γ conversions, π^0 and η decays) with low invariant mass $m_{\text{inv}} < 12.5$ MeV/c^2 are selected. The photonic electron candidates

are required to satisfy all track quality and kinematic cuts (as summarized in Table 3.2). Moreover, all electron identification cuts, i.e. TPC, TOF and BEMC cuts, are applied on the first photonic electron candidate from the pair while the second one, not biased by the studied detector, is used for efficiency studies. Overview of requirements put on studied electron candidates is in Table 4.1. Since the probability that electron has a signal in TOF and BEMC is correlated signal in TOF was required for the photo-candidate in BEMC matching efficiency calculation.

	TPC cut	TOF cut	TOF matching	BEMC cut	BEMC matching
TPC cut efficiency	×	✓	✓	✓	✓
TOF cut efficiency	✓	×	✓	✓	✓
TOF matching efficiency	✓	×	×	✓	✓
BEMC cut efficiency	✓	✓	✓	×	✓
BEMC matching efficiency	✓	×	×	×	×

Table 4.1: Overview of requirements applied on studied photonic electron candidates.

In order to remove non-photonic contributions from the studied sample, the like-sign background photonic electron pairs were subtracted from the unlike-sign pairs and the photonic electrons from subtracted sample were studied. This is illustrated in Figure 4.3 where invariant mass spectrum of photonic electron candidates with momenta $(0.4 - 0.6)$ GeV/c (from unlike-sign, like-sign and subtracted pairs) used for TPC cut efficiency calculation are shown.

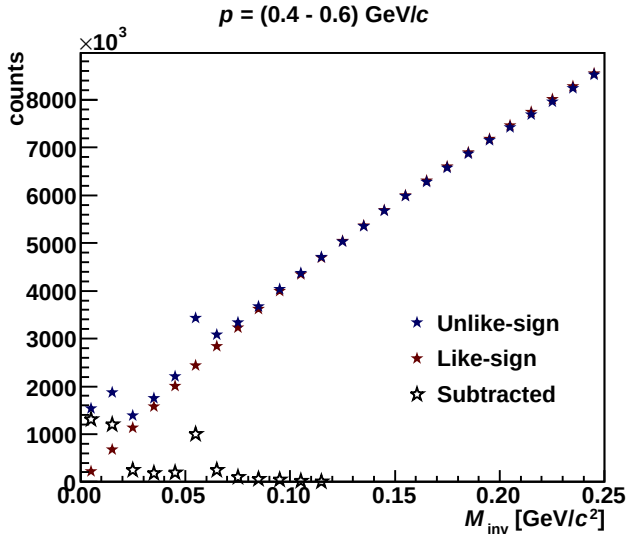

Figure 4.3: The invariant mass spectra of photonic electron pairs with momenta $(0.4 - 0.6)$ GeV/c used for TPC cut efficiency calculation.

TPC cut efficiency

TPC cut efficiency $\epsilon_{\mathrm{TPCcut}}$ estimates the fraction of photonic electron candidates satisfying the $n\sigma_{\mathrm{e}}$ cut used in the analysis, $-1.5 < n\sigma_{\mathrm{e}} < 2.0$. The $n\sigma_{\mathrm{e}}$ distributions of photonic electrons were fitted with Gaussian function in each momentum bin in the range $-2.0 < n\sigma_{\mathrm{e}} < 3.0$ (this range was chosen due to the residual contamination from other particles, mostly pions). Left panel of Figure 4.4 shows the $n\sigma_{\mathrm{e}}$ distribution of electrons in the momentum range $(0.4 - 0.6)$ GeV/c with Gaussian fit applied.

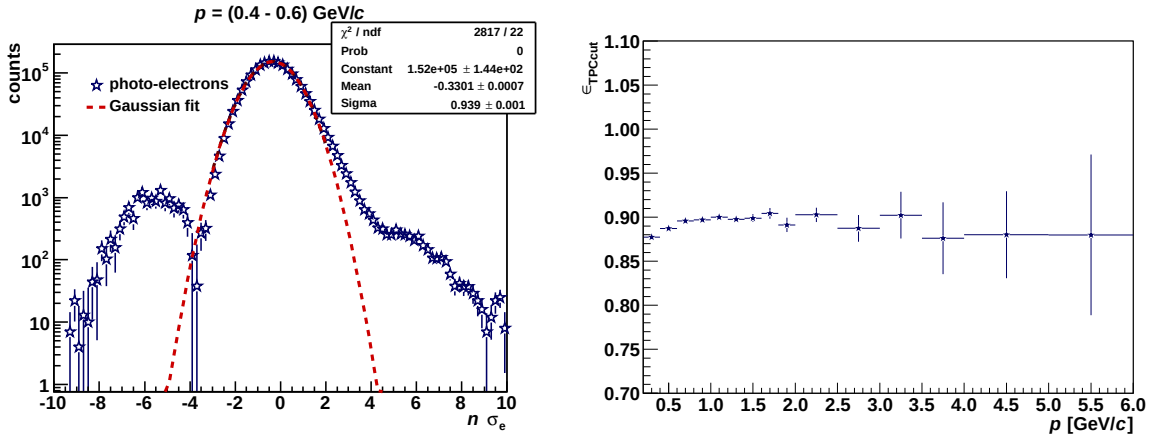

Figure 4.4: Left: $n\sigma_{\mathrm{e}}$ distribution for photonic electrons with momenta $(0.4 - 0.6)$ GeV/c. Right: TPC cut efficiency $\epsilon_{\mathrm{TPCcut}}$ given as a function of photonic electron momentum p.

The TPC cut efficiency was then calculated as the ratio of the area under the Gaussian curve in the cut range $-1.5 < n\sigma_{\mathrm{e}} < 2.0$ and the area under the Gaussian curve in its whole range. Resulting TPC cut efficiency given as a function of photonic electron momentum can be seen in the right panel of Figure 4.4. To remove the y-dependence of TPC cut efficiency, TPC cut efficiency was weighted by the rapidity distribution of J/ψ in studied momentum bins and so included in further calculations.

TOF cut efficiency

The TOF cut efficiency was calculated as the ratio of the number of photonic electron candidates satisfying $1/\beta$ cut used in the analysis, $0.970 < 1/\beta < 1.025$, to the number of photonic electron candidates satisfying wider cut, $0.93 < 1/\beta < 1.07$, which should be wide enough to cover all the electron candidates.

Left panel of Figure 4.5 shows $1/\beta$ distribution of photonic electron candidates in momentum bin $(0.4 - 0.6)$ GeV/c. Resulting TOF cut efficiency as a function of electron momentum is shown in the right panel of Figure 4.5. As can be seen, the TOF cut efficiency shows constant trend as a function of momentum and is almost 99% what indicates that the $1/\beta$ cut used in the analysis is wide enough to cover practically all electrons (positrons).

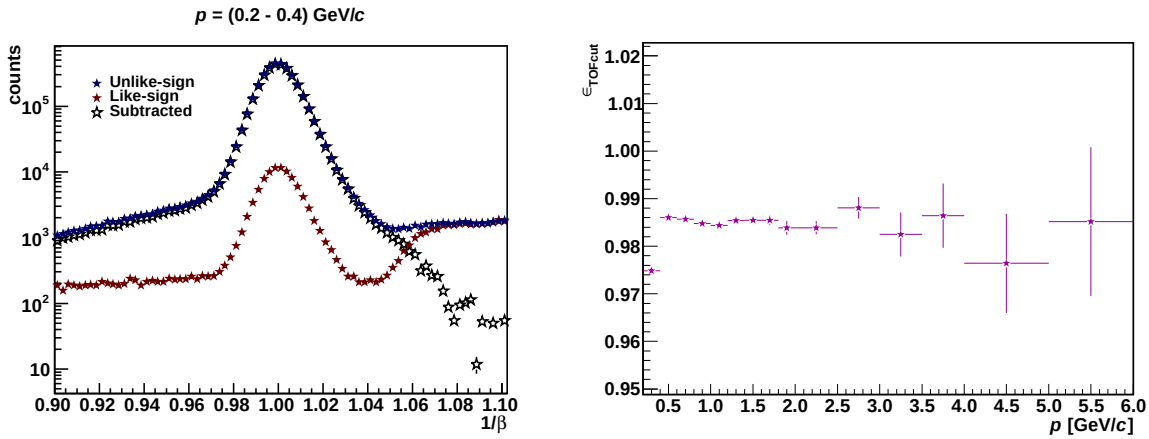

Figure 4.5: Left: $1/\beta$ of photonic electron candidates with momenta $(0.4 - 0.6)$ GeV/c. Right: TOF cut efficiency ϵ_{TOFcut} as a function of photonic electron momentum p.

TOF matching efficiency

TOF matching efficiency was calculated as the ratio of the number of photonic electron candidates with valid TOF signal (defined in Section 1.5.2) to all photonic electron candidates. The Figure 4.6 shows resulting TOF matching efficiency as a function of electron momentum.

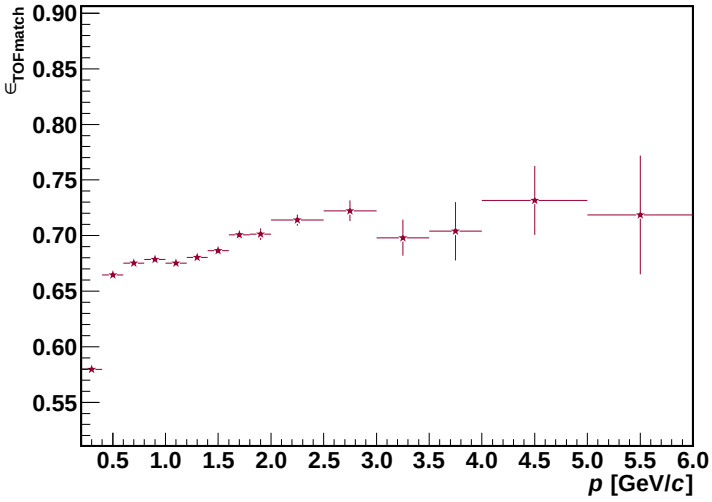

Figure 4.6: TOF matching efficiency $\epsilon_{\mathrm{TOFmatch}}$ as a function of photonic electron momentum p.

BEMC cut efficiency

The BEMC cut efficiency was calculated as the ratio of photonic electrons candidates satisfying the BEMC cut $0.7 < pc/E < 2.0$ (in terms of E/pc: $0.5 < E/pc \lesssim 1.43$) to those with pc/E in the wider range,$0.0 < pc/E < 5.0$, which should be wide enough to

cover all photonic electron candidates.

Left panel of Figure 4.7 shows E/pc of photonic electron candidates in one momentum bin ($1.8 < p < 2.0$ GeV/c). Unlike-sign photonic electron candidates, like-sign background and subtracted data sample are shown. Resulting BEMC cut efficiency as a function of electron momentum is in the right panel of Figure 4.7.

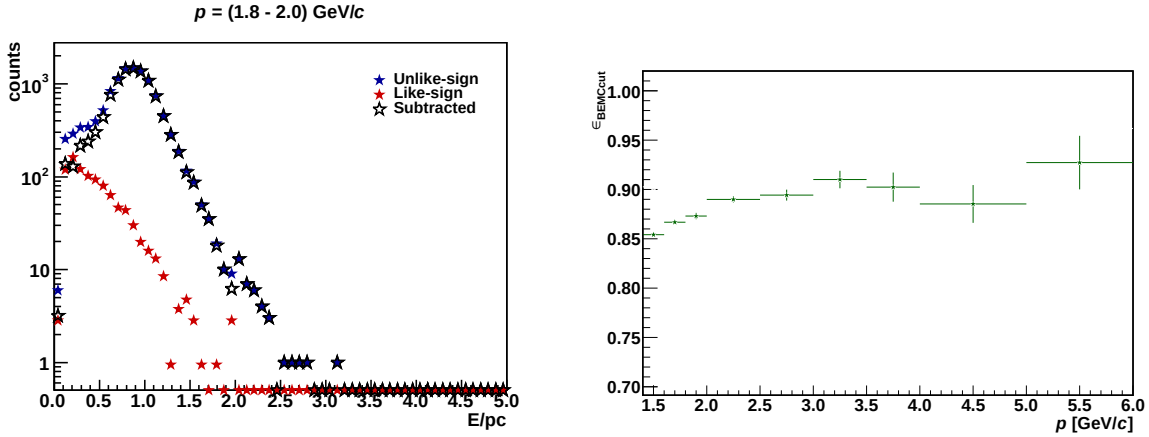

Figure 4.7: Left: pc/E distribution of photonic electron candidates in the momentum bin $1.8 < p < 2.0$ GeV/c. Right: BEMC cut efficiency $\epsilon_{\mathrm{BEMCcut}}$ as a function of electron momentum p.

BEMC matching efficiency

Similarly to the TOF matching efficiency, the BEMC matching efficiency was calculated as the ratio of the number of photonic electron candidates with valid BEMC signal and all photonic electron candidates. Here the valid BEMC signal means that there is a hit recorded in the BEMC tower to which the track from TPC projects. Figure 4.8 shows resulting BEMC matching efficiency as a function of photonic electron momentum.

Resulting single electron identification efficiency

Figure 4.9 shows the resulting single electron identification efficiency as a function of momentum calculated using 4.4. The efficiency observed in the first p bin is systematically lower than in other momentum bins, this applies not only for the single electron identification efficiency but also for track and matching efficiencies described above. The effect is most significant for TOF matching efficiency. It is expected that this decrease in efficiency is caused by very slow particles. It takes them a long time to reach the detector or they do not even reach the detector. Thus their reconstruction efficiency is lower. Figure 4.9 also shows step around $p = 1.4$ GeV/c which is caused by the change of the selection criteria on electron candidates.

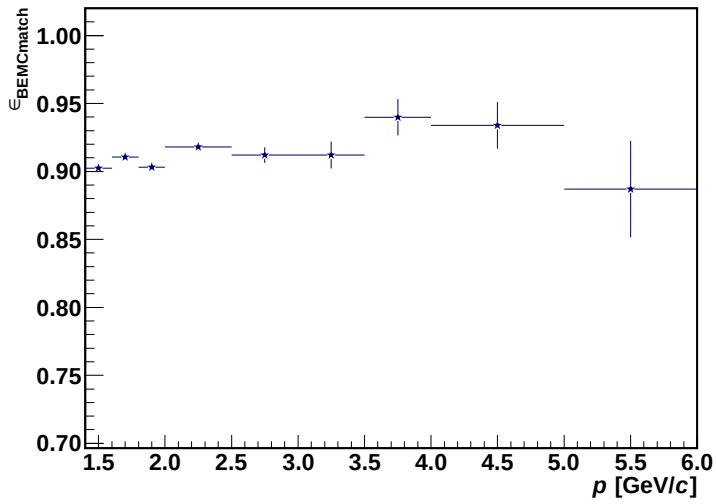

Figure 4.8: BEMC matching efficiency $\epsilon_{BEMCmatch}$ as a function of photonic electron momentum p.

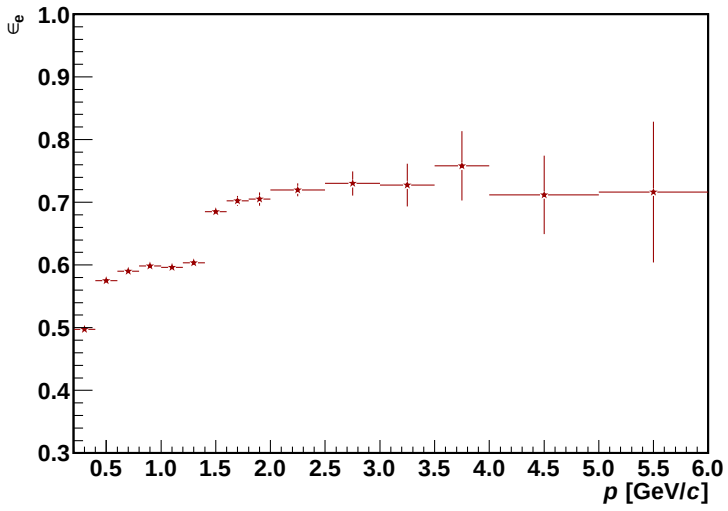

Figure 4.9: Resulting single electron identification efficiency ϵ_e as a function of electron momentum p.

4.1.3 Resulting folded J/ψ reconstruction efficiency

Resulting folded J/ψ reconstruction efficiency ϵ_{folded} was caculated according to Equation 4.2. Weighting factor, TPC tracking efficiency and geometrical acceptance $\epsilon_{\text{geomxacc}}$ and single electron identification efficiency needed for ϵ_{folded} extraction have been described in previous sections. Resulting folded J/ψ reconstruction efficiency can be seen in Figure 4.10.

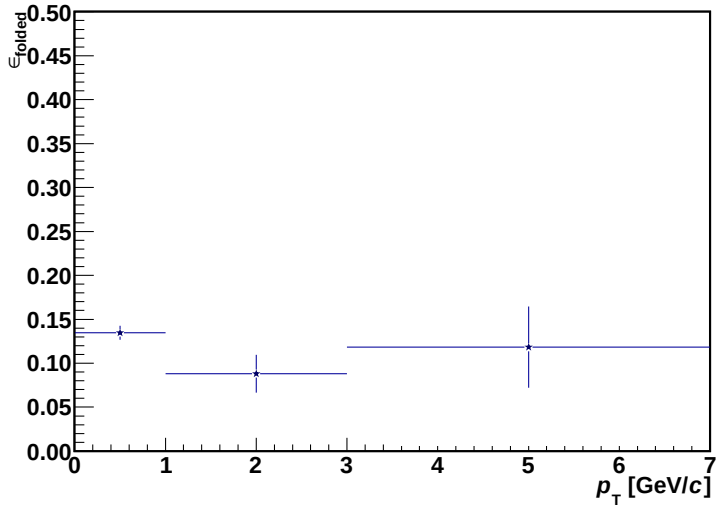

Figure 4.10: Folded J/ψ reconstruction efficiency in three studied transverse momentum bins p_{T}.

4.2 Signal counting correction

J/ψ signal was calculated by the bin-counting method in the region of electron-positron invariant mass $(2.9, 3.2)$ GeV/c^2. However, due to the detector effects not all of J/ψ are reconstructed in this invariant mass range. The signal counting correction was estimated from the embedding where the simulated J/ψ invariant mass spectra were scaled to the signal peak of the measured spectra as can be seen in Figure 4.11 and the fraction of J/ψ with invariant mass outside the range $(2.9, 3.2)$ GeV/c^2 was calculated. This fraction was then estimated to be $\sim 10\%$ and increases towards higher p_{T}.

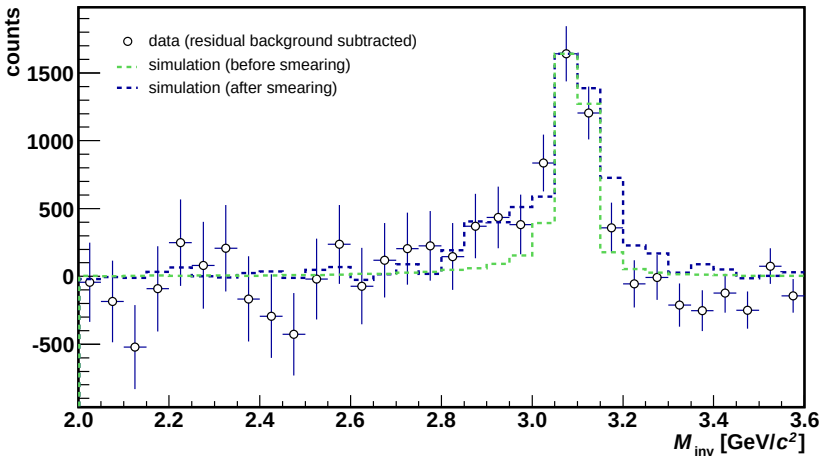

Figure 4.11: J/ψ invariant mass spectrum from data compared to simulation for J/ψ p_{T} integrated.

To improve the agreement between the data and the simulation, the correction to the simulated spectra was performed by smearing the momentum resolution of daughter

electrons (positrons). The momentum resolution is defined as

$$\delta p_{\mathrm{T}} = \frac{p_{\mathrm{T}}^{MC} - p_{\mathrm{T}}^{reco}}{p_{\mathrm{T}}^{MC}} \tag{4.5}$$

where p_{T}^{MC} denotes simulated and p_{T}^{reco} reconstructed transverse momentum of J/ψ daughter electrons. Left panel of Figure 4.12 shows δp_{T} as a function of p_{T} for electrons and positrons from J/ψ decay obtained from simulation. Influence of detector effects can be seen from higher occupancy of electrons in the area of $\delta p_{\mathrm{T}} > 0$ than on the other side denoting lower reconstructed transverse momentum than simulated. Values of δp_{T} are distributed around the mean value $\sim$ 0.01-0.02 which is illustrated is in the right panel of Figure 4.12 for p_{T} = 1-2 GeV/c. As already indicated, for better agreement between the simulated di-electron invariant mass spectrum and the one from data, additional Gaussian smearing of electron transverse momentum with mean $\delta p_{\mathrm{T}} = 0$ and width A . p_{T} was applied to the momentum resolution. Parameter A was determined from the best value of χ^2/ndf for invariant mass shape data vs. embedding in the range $2.9 - 3.2$ GeV/c^2. A was varied in the range 0.00 - 0.01 and the best $\chi^2/ndf \sim 1.21$ for J/ψ p_{T} integrated was achieved for A = 0.78%. This value of A was used for all J/ψ p_{T} bins.

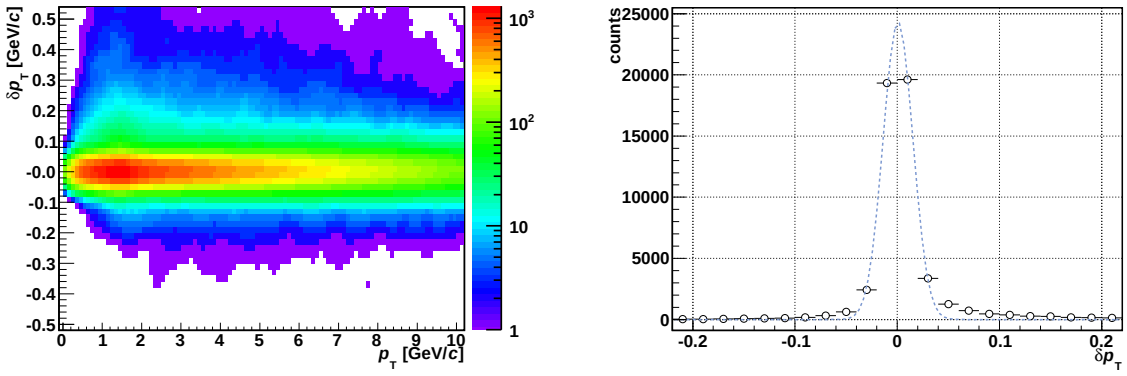

Figure 4.12: Left: Transverse momentum resolution of electrons δp_{T} as a function of p_{T} from simulated data. Right: δp_{T} for p_{T} = 1-2 GeV/c. Gaussian fit is shown.

4.3 Overall J/ψ reconstruction efficiency

Resulting J/ψ reconstruction efficiency ϵ_{reco} was calculated using the formula 4.1 and using the calculated efficiency factors from previous sections. ϵ_{reco} as a function of J/ψ p_{T} is shown in the Figure 4.13. As can be seen the overall reconstruction efficiency is on the level of 10 %.

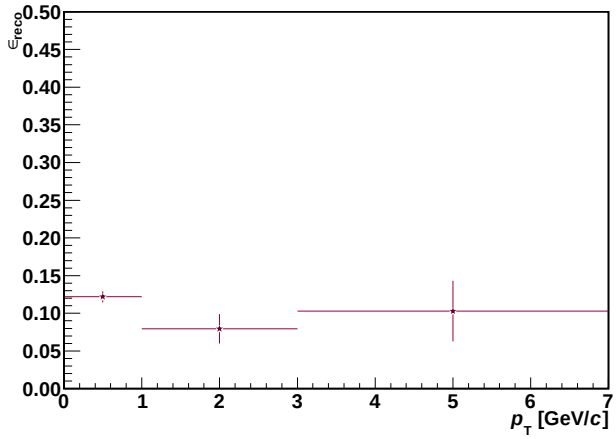

Figure 4.13: Resulting J/ψ reconstruction efficiency in three bins of J/ψ p_{T}.

Chapter 5

Systematic uncertainties

In this chapter the main sources of systematic uncertainties in J/ψ analysis in central U+U data are described. Systematic uncertainties of J/ψ invariant yield coming from the extraction of J/ψ raw yield, simulation and efficiency calculation are evaluated.

Since no J/ψ embedding for central U+U collisions has been ready at the time of finishing this thesis, the embedding data from 2011 Au+Au collisions at the centrality class 0 - 5 % were used in this analysis. Results presented here are thus not final and give the first estimate (upper limit) of systematic uncertainties. In the nearest future they will be calculated using U+U embedding data.

5.1 Yield extraction

The J/ψ raw yield was obtained by the bin counting method. First, the combinatorial background was subtracted from the electron-positron invariant mass spectrum. Then, the invariant mass distribution was fitted with the Crystal-Ball function to describe the signal shape and with the linear function to describe the residual background in the range 2.0 - 3.6 GeV/c^2. The uncertainties associated with this method of signal extraction are described below.

Range of bin-counting

One of the contributions to the uncertainty of the yield comes from the choice of the range in which J/ψ signal was counted. The J/ψ raw yield was obtained by counting the number of entries in the electron-positron mass spectrum in the range $2.9 < m_{\mathrm{inv}} < 3.2$ GeV/c^2 after the combinatorial and residual background subtraction. The number of counts was corrected using the fraction of J/ψ outside of this mass range which was determined using the smeared signal shape from simulation.

In order to estimate uncertainty from the range of the bin counting J/ψ raw yield was counted in larger mass window, $2.7 < m_{\mathrm{inv}} < 3.3$ GeV/c^2. Afterwards it was corrected the same way as in the case of smaller range discussed in more detail in Section 4.2 and the difference in the yields was accounted as a systematic uncertainty. It varies in the range 2.8 - 8.1 % depending on p_{T}.

Residual background fitting

Linear function was used to describe the residual background in the invariant mass window $2.0 < m_{\mathrm{inv}} < 3.6$ GeV/c^2. To calculate the corresponding uncertainty other functions were used for the residual background description such as second and third degree polynomials and exponential function. The range of the fit was also varied ($2.0 < m_{\mathrm{inv}} < 3.6$ GeV/c^2, $2.0 < m_{\mathrm{inv}} < 5.0$ GeV/c^2, $2.6 < m_{\mathrm{inv}} < 3.6$ GeV/c^2). Different descriptions of residual background are illustrated in Figure 5.1. It shows the fit of J/ψ mass peak using the Crystal Ball function combined with the listed functions used to describe the residual background. Change of the fitting functions and range caused the difference of the J/ψ yield of 9.4 - 18.1 % depending on p_{T} which was taken as the systematic uncertainty.

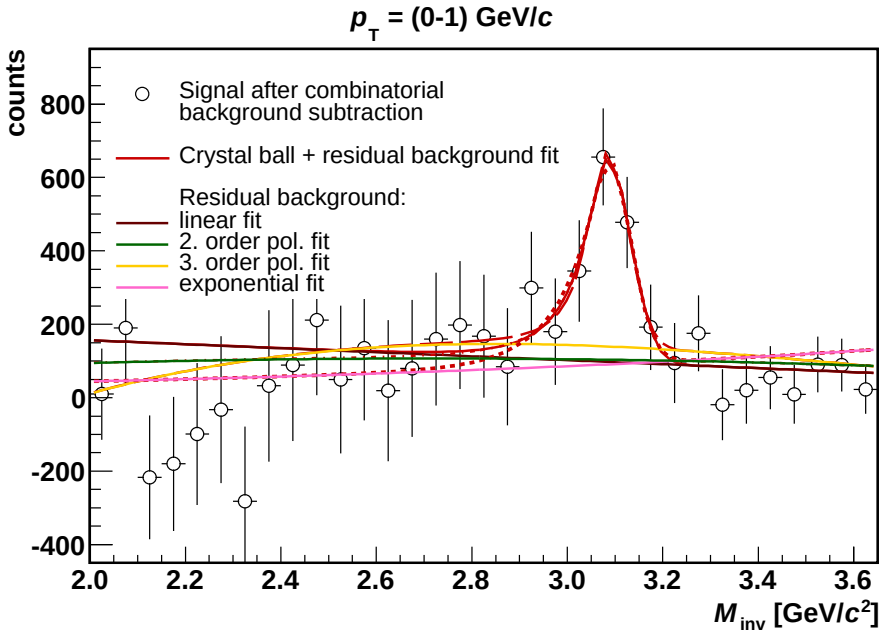

Figure 5.1: Different functions used for the description of the residual background: linear function, second and third degree polynomials and exponential function.

5.2 TPC tracking efficiency and geometrical acceptance

The geometrical tracking efficiency and acceptance was determined by embedding Monte Carlo J/ψ into real data events. J/ψ then decay into daughter electrons and their interaction with the detector material and their acceptance in the detector was studied resulting in the determination of the TPC tracking efficiency and geometrical acceptance (discussed in Section 4.1.1).

The systematic uncertainty connected with TPC tracking efficiency and acceptance was estimated from comparing the distributions of number of fitted hits in TPC from simulation and data. As the data the sample of photonic electrons not affected by the requirement on number of fitted hits was used. The method of systematic uncertainty

extraction was described in [92]. First, both distributions were scaled to unity as can be seen in Figure 5.2 showing the scaled distributions of fitted hits for simulation and data for momentum 4 - 6 GeV/c. . The fraction of photonic electrons satisfying the requirement on the number of fitted hits (nHitsFit > 19) was calculated. Similar fraction was calculated for the embedded data and the ratio of these two fractions was estimated as the relative uncertainty of the number of fitted hits (in each momentum bin). This uncertainty then propagated to the uncertainty of electron identification and, finally, J/ψ yield and was estimated to be 8.3 - 9.1 % depending on the p_{T} of J/ψ.

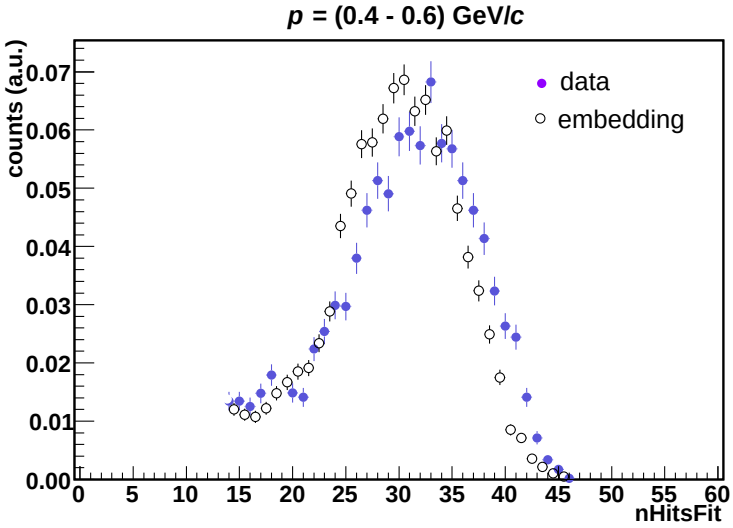

Figure 5.2: The distribution of the number of fitted hits obtained from photonic electrons and from embedding scaled to the unity for momenta $p = 0.4$ - 0.6 GeV/c.

5.3 Electron identification efficiency

The single electron identification efficiency consists of TPC cut efficiency, TOF and BEMC cut and matching efficiencies as described in Chapter 4. The systematic uncertainties of these different contributions are described below.

5.3.1 TPC cut efficiency

The TPC cut efficiency calculation was based on the Gaussian fitting of $n\sigma_e$ distributions of photonic electron candidates and determining the ratio of the area under the fit curve in the range of the TPC cut and the area under the whole electron Gaussian as described in Section 4.1.2.

Fitting procedure - range

Constraints on the range of the Gaussian fit of $n\sigma_e$ distributions were varied to determine the effect on the fitting. The TPC cut efficiency was calculated using different ranges of fitting, $-3.0 < n\sigma_e < 2.0$, $-3.5 < n\sigma_e < 2.5$, $-2.5 < n\sigma_e < 2.0$ and $-4.0 < n\sigma_e < 2.5$.

The difference between the highest and lowest values of efficiency was taken as the systematic uncertainty. This accounted for 1.5 - 2.6 %.

Mean and width of the electron Gaussian

Mean and width of the $n\sigma_e$ distributions of photonic electron candidates, see Figure 5.3, are expected to show no momentum dependence. However, due to some calibration effects or remaining hadron contamination under the electron Gaussian there are some contributions to non-constant trend. These effects are more visible in the dependence of Gaussian mean in Figure 5.3.

To take these effects into account, the mean and width of the electron Gaussian were fitted with the constant function in the range $0.2 < p < 6.0$ GeV/c and constant parameters of these fits were used to calculate the TPC cut efficiency. Change of the final yield of J/ψ using the TPC cut efficiency calculated and the TPC cut efficiency calculated using the constant fit described here was estimated to be 1.4 - 1.9 %, and this was accounted as the systematic uncertainty.

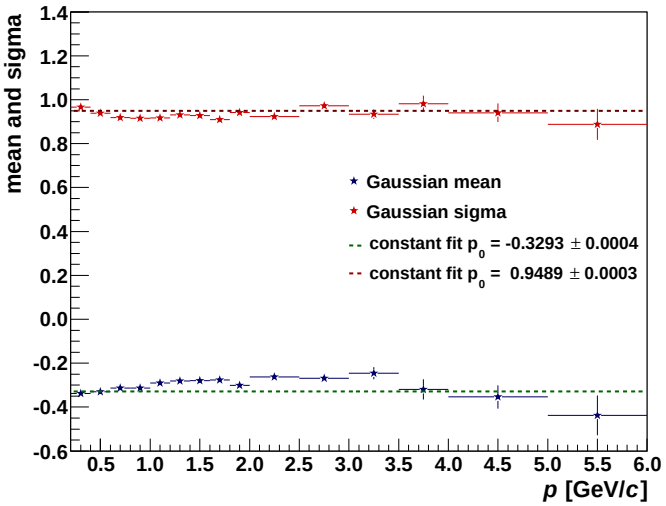

Figure 5.3: Mean and width of the $n\sigma_e$ distributions of photonic electron candidates as a function of photonic electron momentum.

5.3.2 TOF efficiency

TOF cut and matching efficiencies were calculated by comparing the number of photonic electron candidates which satisfied the TOF cut and matching requirements to all of those studied as presented in Section 4.1.2.

TOF matching efficiency

To estimate the systematic uncertainty of the electron TOF matching efficiency, the hadron TOF matching efficiency was calculated. Its momentum dependence was scaled to the calculated electron matching efficiency and the difference between the results of these

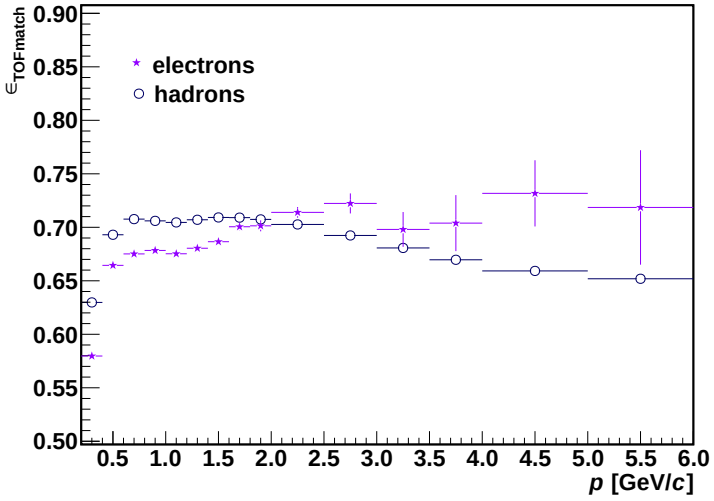

Figure 5.4: TOF matching efficiency for electrons and hadrons as a function of momentum.

two calculations was taken as the systematic uncertainty (1.1 - 1.4 %). Figure 5.4 shows the comparison of TOF matching efficiency obtained from electrons and scaled hadrons. This method of TOF matching efficiency calculation was motivated by work [93]. As can be seen the momentum dependence for electrons shows different trend compared with hadrons and will be object for further studies.

TOF cut efficiency

As in[93, 92] the systematic uncertainty of TOF cut efficiency was estimated by using the Gaussian fit of the electron $1/\beta$ distributions. Gaussian fit was used for $1/\beta$ fitting. The area under the Gaussian fit in the TOF cut range $0.970 < 1/\beta < 1.025$ was calculated as well as the area under Gaussian fit in the range $0.93 < 1/\beta < 1.07$. The TOF cut efficiency was then calculated as the ratio of these two areas. $1/\beta$ distribution with Gaussian fit applied is illustrated in the left panel of Figure 5.5. The TOF cut efficiency extracted from data was compared to that obtained from the Gaussian fit. This can be seen in the right panel of Figure 5.5 showing the $\epsilon_{\mathrm{TOFcut}}$ as a function of momentum extracted from bin counting and from fitting. The difference between them caused the difference in the final yield of 1.1 - 1.4 % which was taken as the systematic uncertainty.

5.3.3 BEMC efficiency

BEMC cut and matching efficiencies were calculated in a similar way as the TOF efficiencies as described in Section 4.1.2. Below the calculations of corresponding systematic uncertainties are described.

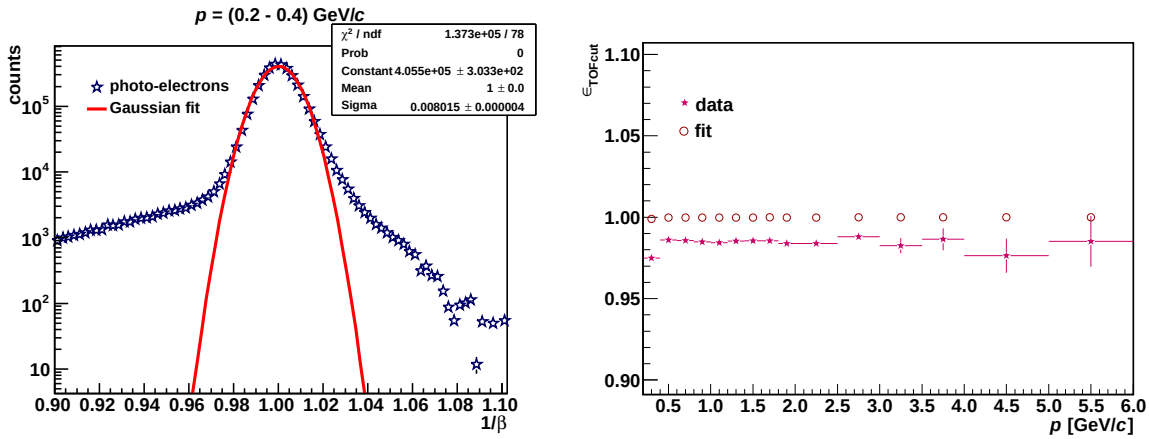

Figure 5.5: Left: $1/\beta$ of photonic electron candidates with momenta 0.4 - 0.6 GeV/c fitted with the Gaussian function. Right: TOF cut efficiency ϵ_{TOFcut} as a function of photonic electron momentum p extracted from data and Gaussian fit.

BEMC matching efficiency

The systematic error of BEMC matching efficiency was obtained from comparing the results from data and from simulation. This is illustrated in the Figure 5.6. As can be seen, results from simulation underestimate results obtained from the data analysis. The difference between simulated BEMC matching efficiency and the matching efficiency extracted from data which is 2.9 - 3.9 % was taken as the systematic uncertainty.

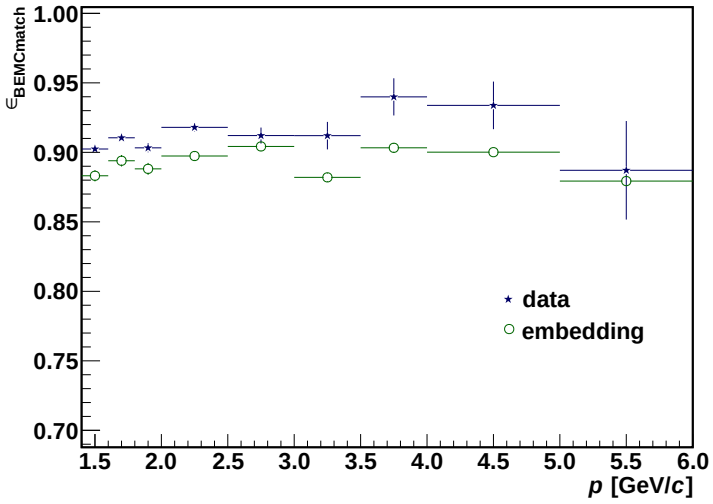

Figure 5.6: BEMC matching efficiency extracted from data and from simulation as a function of electron momentum.

BEMC cut efficiency

Similarly to BEMC matching efficiency, BEMC cut efficiency was extracted from data. To estimate the corresponding systematic error it was compared to the BEMC cut effi-

ciency obtained from simulated data. Figure 5.7 shows the pc/E of photonic electrons compared to simulated data from embedding. As can be seen there is a good agreement between the data and the simulation. The resulting BEMC cut efficiency for real and embedded data can be seen in the right panel of Figure 5.7. The difference between $\epsilon_{\mathrm{BEMCcut}}$ for data and simulation resulted in the systematic uncertainty of the J/ψ yield 2.2 - 4.1 % depending on p_{T}.

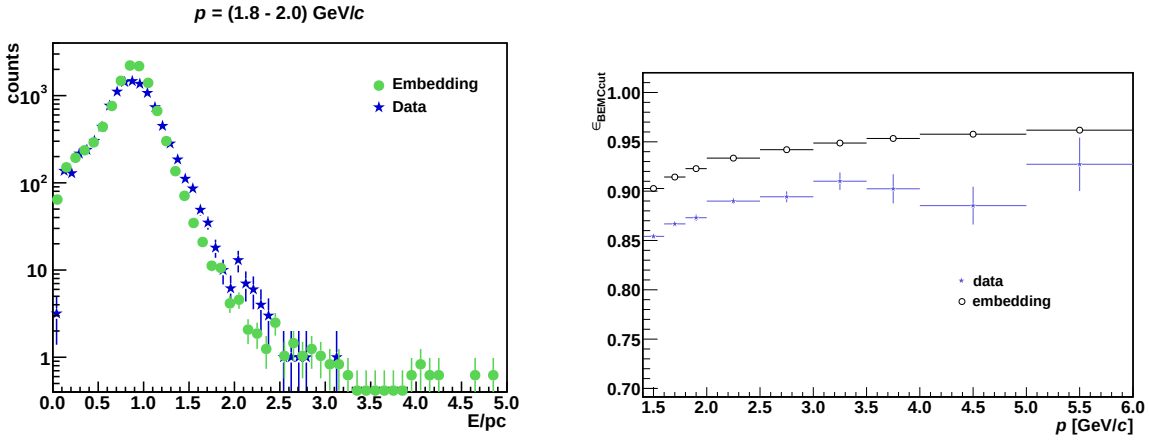

Figure 5.7: Left: pc/E distribution of real and simulated data for electron momentum 1.8 - 2.0 GeV/c. Right: BEMC cut efficiency extracted from data and from simulation as a function of electron momentum.

5.4 Efficiency

Usually, the contributions of single electron identification efficiency are extracted from simulation or estimated as the average between the simulation and data. This method of efficiency calculation enables to reduce statistical fluctuations observed in real data and thus decrease the statistical error of the final results. In the analysis presented in this thesis, the contributions of single electron identification efficiency were, however, calculated from data, since there were no simulated data for U+U collisions available at the time when this analysis was being performed. The closest possible simulated data for Au+Au from year 2011 were temporarily used instead of U+U. However, they are different collision system, do not reach as high multiplicities as central triggered U+U and also there could have been some differences in the experimental setup. Hence, a decision was made to temporarily favor the data in the efficiency studies.

As a consequence the obtained results are significantly affected by large statistical uncertainties of efficiency contributions. These are summarized in the in the overall efficiency uncertainty. It was calculated from statistical uncertainties of the electron (positron) identification efficiencies and J/ψ tracking efficiency shown in Chapter 4. These were combined and resulted in the most significant contribution of systematic uncertainty of the yield which varied from 5.9 to 34.8%.

5.5 Resulting systematic uncertainty

The different contributions to resulting systematic uncertainty of J/ψ in 0-5% central U+U collisions as a function of J/ψ transverse momentum are summarized in Table 5.1. As in [93], for the calculation of the total systematic uncertainty all were added in quadratures. Since some of listed contributions are correlated, the resulting systematic uncertainty gives the upper limit of the uncertainty.

J/ψ p_{T} [GeV/c]	0-1	1-3	3-7
Yield extraction			
Range of bin counting	6.6%	2.8%	8.1%
Residual background fitting	18.1%	17.1%	9.4%
TPC tracking efficiency and acceptance	9.1%	8.4%	8.3%
Electron identification efficiency			
TPC cut efficiency (range of fit)	1.5%	1.9%	2.6%
TPC cut efficiency (mean and width)	1.4%	1.8%	1.9%
TOF matching efficiency	1.1%	1.3%	1.4%
TOF cut efficiency	2.1%	2.4%	2.5%
BEMC matching efficiency	3.0%	2.9%	3.9%
BEMC cut efficiency	2.2%	2.6%	4.1%
Efficiency (statistical uncertainty)	5.9%	22.8%	34.8%
Overall uncertainty	22.6%	30.3%	38.4%

Table 5.1: Overview of different sources of systematic uncertainties for different p_{T} bins. These sources are described in more detail in text. Overall uncertainty includes all uncertainties stated above added in quadratures.

Chapter 6

Results

In this chapter the main results of the analysis of J/ψ in 0 - 5 % central U+U collisions at $\sqrt{s_{\rm NN}} =$ 193 GeV are presented, particularly J/ψ invariant yield and nuclear modification factor.

6.1 Invariant yield

To obtain the invariant yield of J/ψ in 0 - 5 % central U+U collisions the J/ψ raw yield was corrected on the total reconstruction efficiency (Chapter 4) and normalized to the phase space and the number of events analyzed. The invariant J/ψ $p_{\rm T}$ spectrum is defined as

$$B\frac{d^2N}{d\phi p_{\rm T} dp_{\rm T} dy} = \frac{1}{2\pi p_{\rm T}\Delta p_{\rm T}\Delta y}\frac{N_{J/\psi}}{\epsilon_{\rm total}}\frac{1}{N_{\rm ev}} \tag{6.1}$$

where B denotes the branching ratio $J/\psi \rightarrow e^+e^-$, $p_{\rm T}$ is the the mean transverse momentum in a bin of width $\Delta p_{\rm T}$ and the rapidity interval is $\Delta y = 2$ for $|y| < 1$. $N_{J/\psi}$ is the J/ψ raw yield in a given $p_{\rm T}$ bin (Chapter 3), $\epsilon_{\rm total}$ is the total J/ψ reconstruction efficiency discussed in Section 4.3 and $N_{\rm ev}$ is the number of events analyzed satisfying the event cuts (ca. 56 M). Figure 6.1 shows the resulting J/ψ invariant yield as a function of the weighted average of $p_{\rm T}$ in given bin. Statistical and systematic uncertainties are also depicted. The yield decreases towards higher $p_{\rm T}$ and for the highest $p_{\rm T}$ the decrease is the most significant.

6.2 Nuclear modification factor

Nuclear modification factor of J/ψ as a function of $p_{\rm T}$ was calculated according to

$$R_{\rm AA}(p_{\rm T}, y) = \frac{1}{< N_{bin} > 0.964/\sigma^{\rm pp}_{\rm inel}}\frac{d^2N_{\rm AA}/dp_{\rm T}dy}{d^2\sigma_{\rm pp}/dp_{\rm T}dy} \tag{6.2}$$

where $d^2N_{\rm AA}/dp_{\rm T}dy$ denotes J/ψ invariant yield in U+U collisions defined above, $< N_{\rm bin} >$ is the average number of binary nucleon-nucleon collisions in 0–5% central U+U collisions (see Chapter 4). $\sigma^{\rm pp}_{\rm inel}$ is p+p inelastic cross section and U+U collisions 193 GeV and $d^2\sigma_{\rm pp}/dp_{\rm T}dy$ is the invariant cross section of J/ψ production in p+p collisions. The

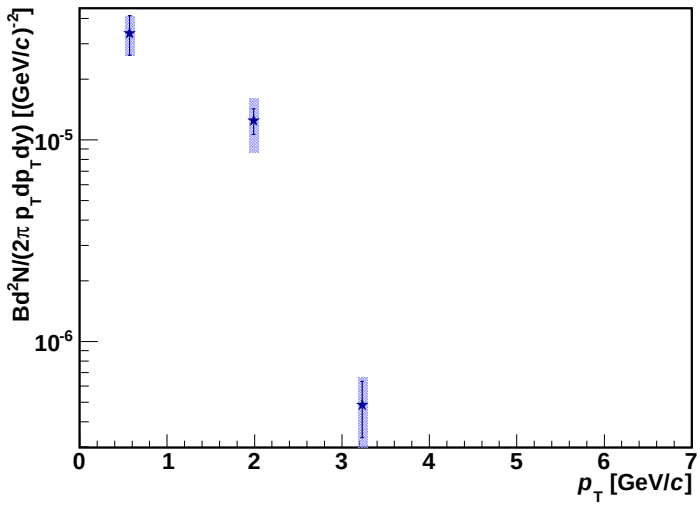

Figure 6.1: J/ψ invariant yield in 0 - 5 % most central U+U collisions according to TOF+ZDC triggers as a function of transverse momentum p_{T}. Shaded band shows systematic uncertainty of the yield.

scaling factor 0.964 was included to account for the difference between the charm cross section in p+p collisions at 200 GeV and 193 GeV.

Since STAR lacks J/ψ low-p_{T} data in p+p collisions, and to make the results of this J/ψ analysis consistent with those from minimum bias U+U collisions, the same p+p reference was used, specifically the data from PHENIX [58] (for $p_{\mathrm{T}} < 2$ GeV/c) and STAR [49] (for $p_{\mathrm{T}} > 2$ GeV/c). However, the PHENIX data are only for $|y| < 0.35$ so it was assumed that the production of J/ψ in that narrower rapidity bin is same as in $|y| < 1$. The p+p reference fitted with the function 4.3 is shown in the Figure 6.2. The fitting function was evaluated in the average p_{T} of each J/ψ p_{T} bin and this value

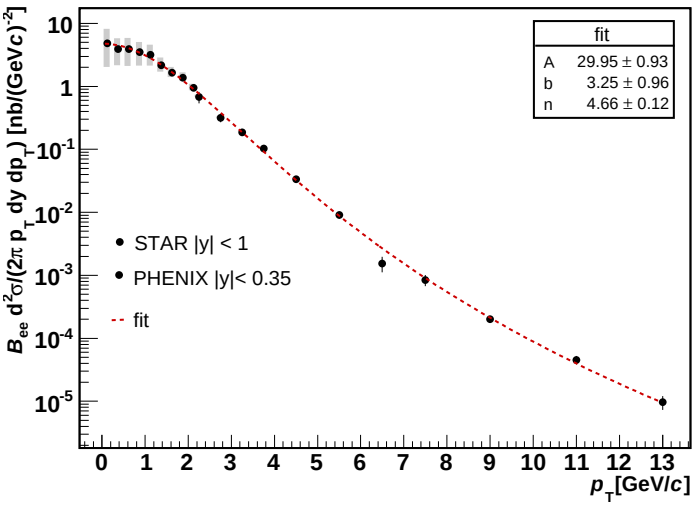

Figure 6.2: Proton+proton reference data from STAR [49] (stars) and PHENIX [58] (circles) fitted with the function 4.3.

was used in formula 6.2. Corresponding error of the p+p reference was included in the calculation of R_{AA} statistical error.

The resulting J/ψ R_{AA} in 0 - 5 % most central U+U collisions at STAR calculated according to equation 6.2 can be seen as the function of p_{T} in Figure 6.3. It shows significant suppression over the whole p_{T} range. For p_{T} below 3 GeV/c the R_{AA} is consistent with results from minimum bias and HT triggered collisions, however, the value of R_{AA} at $p_{\mathrm{T}} \approx 3$ GeV/c shows notable suppression. It should be noted here that in the p_{T} bin 3 - 7 GeV/c the least significant signal of J/ψ was observed. It was accompanied by the considerable statistical and systematic error which was significant also in the calculation of J/ψ reconstruction efficiency.

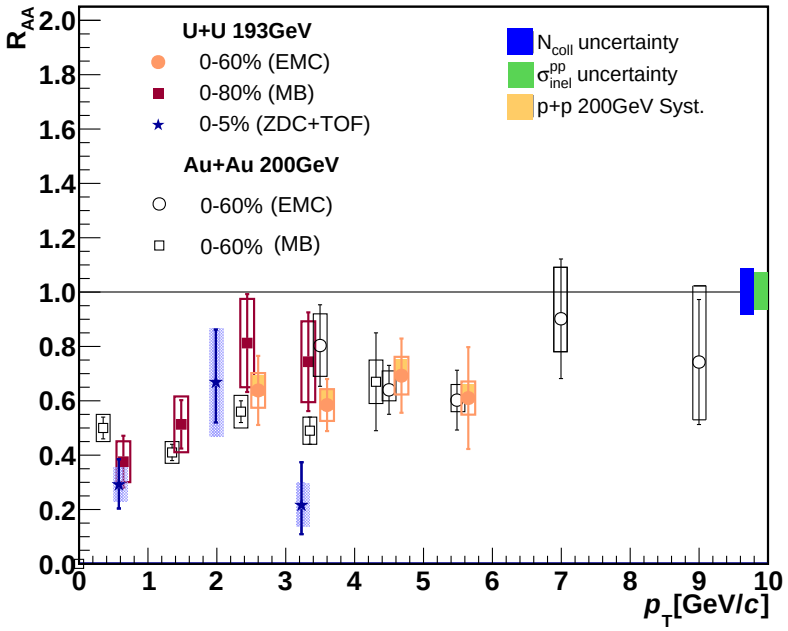

Figure 6.3: J/ψ nuclear modification factor as a function of p_{T} in 0 - 5 % most central U+U collisions. Data are shown together with minimum bias and HT-triggered Au+Au [28, 49] and U+U data [52].

J/ψ R_{AA} as a function of N_{part} is shown in Figure 6.4. U+U central point is compared to results from minimum-bias U+U collisions and results from Au+Au collisions for $p_{\mathrm{T}} <$ 5 GeV/c [49] and $p_{\mathrm{T}} >$ 5 GeV/c [28]. A significant N_{part} uncertainty of J/ψ R_{AA} in central U+U collisions (discussed in Chapter 3) is also illustrated. As can be seen J/ψ R_{AA} in central U+U collisions shows significant suppression which is similar to the suppression observed for low-p_{T} J/ψ in 200 GeV Au+Au collisions of $N_{\mathrm{part}} \approx 350$.

Results presented in this work are not final. First, J/ψ embedding data for U+U collisions will be used in the calculation of J/ψ reconstruction efficiency. Consequently, the systematic uncertainties of the yield will be studied in more detail. As discussed in Section 3.2 N_{bin} and N_{part} for analyzed 0 - 5 % most central U+U data were temporarily estimated by weighting the values from minimum-bias data to the analyzed central triggered multiplicity distribution. These values are very approximate and thus affected by significant systematic uncertainty. Therefore, more precise study of N_{bin} and N_{part} in

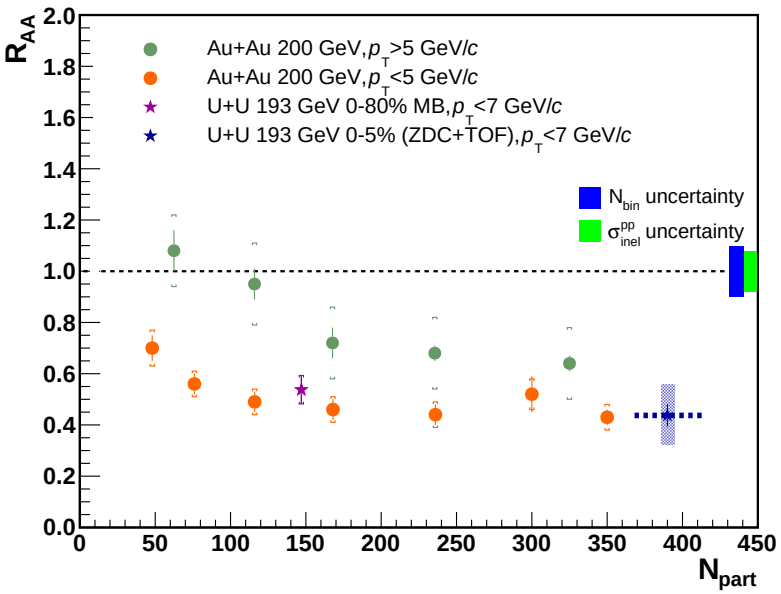

Figure 6.4: J/ψ nuclear modification factor as a function of N_{part} in 0 - 5 % most central U+U collisions (blue star). Shaded band shows systematic uncertainty of the yield and horizontal dashed line shows the systematic uncertainty of N_{part}. Data are compared to results from minimum bias U+U collisions (violet star) and from Au+Au collisions at low p_{T} [49] (orange circle) and high p_{T} [28] (green circle).

central triggered U+U collisions is needed for the correct interpretaion of obtained results.

Conclusions

In this thesis the analysis of J/ψ production via the di-electron decay channel in central triggered 0 - 5 % most central U+U collisions at $\sqrt{s_{\mathrm{NN}}} = 193$ GeV at the STAR experiment was presented.

Suppression of J/ψ production in heavy-ion collisions compared with p+p collisions provides one of the key signatures of the quark-gluon plasma formation. In U+U collisions the effects of the hot medium are expected to be the most significant among all nuclei which have been collided at RHIC until now. Therefore, J/ψ production studies in such colliding system are important.

Basic information about heavy-ion collisions and selected signatures which may refer to the evidence of the quark-gluon plasma (QGP) were briefly described in this thesis. The work focuses in more detail on theoretical background of J/ψ production and its modification in heavy-ion collisions as well as recent heavy quarkonium measurements at RHIC.

One of the foremost heavy-ion experiments, the STAR experiment at RHIC, was presented. Information obtained from three of its main subsystems, the Time Projection Chamber, Time Of Flight detector and Barrel Electromagnetic Calorimeter was used for identification of J/ψ daughter electrons and positrons in central U+U collisions. J/ψ raw yield of significance larger than 8 σ was observed for $p_{\mathrm{T}} < 7$ GeV/c at mid-rapidity. This allowed to divide the signal in three p_{T} bins. Different, either data-driven corrections or corrections based on simulation of J/ψ decay and the interaction of its daughter electrons in the detector were performed. The total J/ψ reconstruction efficiency was estimated to be 8 - 12 % depending on p_{T}. The first estimate of systematic uncertainties was also performed.

Finally, J/ψ invariant yield was calculated and compared to the scaled p+p reference to determine the nuclear modification factor R_{AA}. J/ψ R_{AA} as a function of p_{T} and N_{part} shows significant suppression. J/ψ R_{AA} for $p_{\mathrm{T}} < 3$ GeV/c in central triggered U+U collisions is similar to that observed in minimum bias U+U and Au+Au collisions at 200 GeV at STAR. Our results on J/ψ R_{AA} in central U+U collisions move the centrality studies of J/ψ production in heavy-ion collisions towards higher N_{part}. J/ψ R_{AA} in U+U collisions is consistent with Au+Au results with similar N_{part} indicating possible interplay of dissociation and recombination of heavy quark-antiquark pairs as processes modifying J/ψ production.

Results of J/ψ analysis in central triggered U+U collisions presented in this work are not final. In the future more precise study of J/ψ signal corrections and systematic uncertainties using the simulation for U+U collisions will be performed.

Bibliography

[1] S. Bethke. The 2009 World Average of alpha(s). *Eur. Phys. J.* C **64**, 689-703 (2009).

[2] E. Eichten, K. Gottfried, T. Kinoshita, K. D. Lane, and T. M. Yan. Charmonium: Comparison with experiment. *Phys. Rev.* D **21**, 203–233 (1980).

[3] K.A. Olive *et al.* (Particle Data Group), *Chin. Phys.* C **38**, 090001 (2014) and (2015) update.

[4] A. Y. Potekhin P. Haensel and D. G. Yakovlev. *Neutron Stars 1.* Springer-Verlag New York, New York, 1st edition, 2007.

[5] S. Bushwick. How low can RHIC go? `https://www.bnl.gov/rhic/news2/news.asp?a=1870&t=today`. [online] [04.04.2016].

[6] The STAR Collaboration. Studying the Phase Diagram of QCD Matter at RHIC. `https://drupal.star.bnl.gov/STAR/starnotes/public/sn0598`. [online] [03.04.2016].

[7] H. Satz S. Sarkar and B. Sinha. *The Physics of the Quark-Gluon Plasma A: Introductory Lectures.* Springer, Berlin Heidelberg, 1st edition, 2010.

[8] Z. Del Vecchio. Moti collettivi (flow) in collisioni di ioni pesanti. `http://slideplayer.it/slide/619101/`. [online] [05.04.2016].

[9] T. Schuster M. Kliemant, R. Sahoo and R. Stock. Global properties of nucleus–nucleus collisions. In *The Physics of the Quark-Gluon Plasma*, volume 785 of *Lecture Notes in Physics*, pages 23–103. Springer, Berlin Heidelberg, 2010.

[10] G. Odyniec D. Kikola and R. Vogt. Prospects for quarkonia production studies in U + U collisions. *Phys. Rev.*, C **84**. 054907 (2011).

[11] E. V. Shuryak. High-energy collisions of strongly deformed nuclei: An Old idea with a new twist. *Phys. Rev.*, C **61**. 034905 (2000).

[12] R. Snellings. Elliptic Flow: A Brief Review. *New J. Phys.*, **13**. 055008 (2011).

[13] B.I. Abelev et. al. Centrality dependence of charged hadron and strange hadron elliptic flow from $\sqrt{s_{NN}}$ = 200 GeV Au+Au collisions. *Phys. Rev.*, C **77**. 054901 (2008).

[14] Yuri L. Dokshitzer and D.E. Kharzeev. Heavy quark colorimetry of QCD matter. *Phys.Lett.*, B 519. 199–206 (2001).

[15] A. Stonebraker. Viewpoint: The Stopping Power of Hot Nuclear Matter. `http://physics.aps.org/articles/v7/97`. [online] [02.04.2016].

[16] J. Adams *et.al* (STAR Collaboration). Evidence from $d+$Au measurements for final-state suppression of high-p_T hadrons in Au + Au collisions at rhic. *Phys. Rev. Lett.*, **91**. 072304 (2003).

[17] G. Xie. Nuclear Modification factors of D^0 meson in Au+Au collisions at 200 GeV. Quark Matter 2015.

[18] M. R. Lomnitz. Measurement of D meson azimuthal anisotropy in Au+Au 200 GeV collisions at RHIC. Quark Matter 2015.

[19] L. Adamczyk *et al.* Elliptic flow of non-photonic electrons in Au+Au collisions at $\sqrt{s_{\rm NN}} = 200$, 62.4 and 39 GeV. arXiv 1405.6348 (2014).

[20] T. Matsui and H. Satz. J/ψ Suppression by Quark-Gluon Plasma Formation. *Phys.Lett.*, B **178**. 416 (1986).

[21] P.P. Bhaduri, P. Hegde, H. Satz, and P. Tribedy. An introduction to the spectral analysis of the qgp. In *The Physics of the Quark-Gluon Plasma*, volume 785 of *Lecture Notes in Physics*, pages 179–197. Springer, Berlin Heidelberg, 2010.

[22] H. Fritzsch. Producing heavy quark flavors in hadronic collisions' a test of quantum chromodynamics. *Phys. Lett.*, B **67**(2). 217–221 (1977).

[23] F. Halzen. Cvc for gluons and hadroproduction of quark flavours. 105–108 (1977).

[24] A. D. Frawley, T. Ullrich, and R. Vogt. Heavy flavor in heavy-ion collisions at RHIC and RHIC II. *Phys. Rept.*, **462**. 125–175 (2008).

[25] R. Gastmans, W. Troost, and T. T. Wu. Heavy flavours heavy quarkonia production from gluons. *Nuclear Physics B - Proceedings Supplements*, **1**(2). 259–263 (1988).

[26] E. L. Berger and D. Jones. Inelastic photoproduction of j/ψ and Υ by gluons. *Phys. Rev.*, D **23**, 1521–1530 (1981).

[27] E. Braaten S. Fleming and T.C. Yuan. Production of heavy quarkonium in high-energy colliders. *Ann. Rev. Nucl. Part. Sci.*, **46**. 197–235 (1996).

[28] L. Adamczyk et al. J/ψ production at high transverse momenta in $p+p$ and Au+Au collisions at $\sqrt{s_{NN}} = 200$ GeV. *Phys. Lett.*, B **722**. 55–62 (2013).

[29] L. Kosarzewski. Production of J/ψ in minimum-bias $p+p$ collisions at $\sqrt{s} = 200$ GeV in STAR. *Acta Phys.Polon.* B Vol.5(2), 543 (2012).

[30] L. Adamczyk *et al.* J/ψ production at low transverse momentum in p+p and d+Au collisions at $\sqrt{s_{NN}}$ = 200 GeV. 2016. arXiv 1602.02212 (2016).

[31] A. Adare *et al.* Ground and excited state charmonium production in $p+p$ collisions at $\sqrt{s} = 200$ GeV. *Phys. Rev.*, D **85**. 092004 (2012).

[32] Yan-Qing Ma, Kai Wang, and Kuang-Ta Chao. A complete NLO calculation of the J/ψ and ψ' production at hadron colliders. *Phys. Rev.*, D **84**. 114001 (2011).

[33] P. Artoisenet, J. Campbell, J. P. Lansberg, F. Maltoni, and F. Tramontano. Υ production at fermilab tevatron and lhc energies. *Phys. Rev. Lett.*, **101**. 152001 (2008).

[34] J. Seixas P. Faccioli, C. Lourenco and H. K. Wohri. Towards the experimental clarification of quarkonium polarization. *Eur. Phys. J.*, C **69**, 657–673 (2010).

[35] L. Adamczyk et al. J/ψ polarization in p+p collisions at $\sqrt{s} = 200$ GeV in STAR. *Phys. Lett.*, B **739**. 180–188 (2014).

[36] A. Adare *et al.* Transverse momentum dependence of J/ψ polarization at midrapidity in $p+p$ collisions at $\sqrt{s} = 200$ GeV. *Phys. Rev.*, D **82**. 012001 (2010).

[37] J. P. Lansberg. J/ψ production at sqrt(s)=1.96 and 7 TeV: Color-Singlet Model, NNLO* and polarisation. *J. Phys.*, G **38**. 124110 (2011).

[38] S. Kim H. S. Chung, Ch. Yu and J.Lee. Polarization of prompt j/ψ in proton-proton collisions at rhic. *Phys. Rev.*, D **81**. 014020 (2010).

[39] B. Trzeciak. J/ψ polarization measurements in p+p collisions at $\sqrt{s} = 200$ and 500 GeV with the STAR experiment. *PoS*, EPS-HEP2015, 470 (2015).

[40] A. Mócsy and P. Petreczky. Can quarkonia survive deconfinement? *Phys. Rev.*, D **77**. 014501 (2008).

[41] A. Adare et al. Measurement of $\Upsilon(1S + 2S + 3S)$ production in $p+p$ and Au+Au collisions at $\sqrt{s_{NN}} = 200$ GeV. *Phys. Rev.*, C **91**(2). 024913 (2015).

[42] N.Xu Y. Liu, Z. Qu and P. Zhuang. J/ψ Transverse Momentum Distribution in High Energy Nuclear Collisions at RHIC. *Phys. Lett.*, B **678**, 72–76 (2009).

[43] H. Pereira Da Costa. Charmonium production in Pb-Pb collisions with ALICE at the LHC. arXiv 1512.07610 (2015).

[44] F. Karsch and R. Petronzio. Momentum distribution of J/ψ in the presence of a quark-gluon plasma. *Phys. Lett.*, B **193**(1). 105–109 (1987).

[45] C. Salgado K. J. Eskola, H. Paukkunen and A. Carlos. EPS09 - Nuclear PDFs and Their Uncertainties at NLO. *Nucl. Phys.*, A **830**. 599C-602C (2009).

[46] X. Zhao and R. Rapp. Charmonium in Medium: From Correlators to Experiment. *Phys. Rev.*, C **82**. 064905 (2010).

[47] L. Kluberg and H. Satz. Color Deconfinement and Charmonium Production in Nuclear Collisions. arXiv 0901.3831 (2009).

[48] E. G. Ferreiro. Excited charmonium suppression in protonnucleus collisions as a consequence of comovers. *Phys. Lett.*, B **749**. 98–103 (2015).

[49] L. Adamczyk et al. J/ψ production at low p_T in Au+Au and Cu+Cu collisions at $\sqrt{s_{NN}} = 200$ GeV with the STAR detector. *Phys. Rev.*, C **90**(2), 024906 (2014).

[50] A. Adare *et al.* J/ψ Production vs Centrality, Transverse Momentum, and Rapidity in Au+Au Collisions at $\sqrt{s_{NN}} = 200$ GeV. *Phys. Rev. Lett.*, **98**, 232301 (2007).

[51] L. Adamczyk *et al.* Measurement of J/ψ Azimuthal Anisotropy in Au+Au Collisions at $\sqrt{s_{NN}} = 200$ GeV. *Phys. Rev. Lett.*, **111**(5), 052301 (2013).

[52] W. Zha. Recent measurements of quarkonium production in p+p and A + A collisions from the STAR experiment. *Nucl. Phys.*, A **931**. 596-600 (2014).

[53] S. J. Sanders P. Steinberg M. L. Miller, K. Reygers. Glauber modeling in high energy nuclear collisions. *Ann. Rev. Nucl. Part. Sci.*, **57**, 205–243 (2007).

[54] A. Adare *et al.* Forward J/ψ production in U+U collisions at $\sqrt{s_{NN}}$=193 GeV. *Phys. Rev.*, C **93**(3). 034903 (2016).

[55] B. Mohanty H. Masui and N. Xu. Predictions of elliptic flow and nuclear modification factor from 200 GeV U + U collisions at RHIC. *Phys. Lett.*, B **679**. 440–444 (2009).

[56] Q. Y. Shou, Y. G. Ma, P. Sorensen, A. H. Tang, F. Videbak, and H. Wang. Parameterization of Deformed Nuclei for Glauber Modeling in Relativistic Heavy Ion Collisions. *Phys. Lett.*, B **749**. 215–220 (2015).

[57] L. Ziwei and C.M. Ko. υ absorption in hadronic matter. *Phys. Lett.*, B **503**(12). 104–112 (2001).

[58] A. Adare *et al.* Transverse-momentum dependence of the J/ψ nuclear modification in d+Au collisions at $\sqrt{s_{NN}} = 200$ GeV. *Phys. Rev.*, C **87**. 034904 (2013).

[59] S. Chatrchyan et al. Observation of sequential Υ suppression in pbpb collisions. *Phys. Rev. Lett.*, **109**:222301 (2012).

[60] R. Vogt. Cold Nuclear Matter Effects on J/ψ and Υ Production at the LHC. *Phys. Rev.*, C **81**. 044903 (2010).

[61] L. Adamczyk*et al.* Suppression of Υ production in d+Au and Au+Au collisions at $\sqrt{s_{NN}}$=200 GeV. *Phys. Lett.*, B **735**, 127–137 (2014).

[62] F. Arleo and S. Peigne. Heavy-quarkonium suppression in p-A collisions from parton energy loss in cold QCD matter. *JHEP*, **03**, 122 (2013).

[63] C. Aidala *et al.* Nuclear matter effects on J/ψ production in asymmetric Cu+Au collisions at $\sqrt{s_{NN}} = 200$ GeV. *Phys. Rev.*, C **90**(6), 064908 (2014).

[64] Brookhaven National Laboratory. The STAR experiment at the Relativistic Heavy Ion Collider. `http://www.star.bnl.gov/`. [online] [31.03.2016].

[65] W. Fischer. Run overview ofthe Relativistic Heavy Ion Collider. `http://www.rhichome.bnl.gov/RHIC/Runs/`. [online] [10.04.2016].

[66] Brookhaven National Laboratory. RHIC Facility. `https://www.flickr.com/photos/brookhavenlab/7979381212/in/album-72157613690851651/`. [online] [23.03.2016].

[67] Brookhaven National Laboratory. The RHIC Complex. `https://www.bnl.gov/rhic/complex.asp`. [online] [31.03.2016].

[68] Brookhaven National Laboratory. PHENIX A Physics Experiment At RHIC. `http://www.phenix.bnl.gov/`. [online] [31.03.2016].

[69] M. Anderson, J. Berkovitz, W. Betts, R. Bossingham, F. Bieser, et al. The STAR Time Projection Chamber: A Unique tool for studying high multiplicity events at RHIC. *Nucl. Instrum. Meth.*, A **499**. 659–678 (2003).

[70] The STAR Collaboration. A Proposal for STAR Inner TPC Sector Upgrade (iTPC). `http://indico.cern.ch/event/30248/session/49/contribution/253/material/slides/0.pdf`. [online] [08.06.2015].

[71] H. Bichsel. A method to improve tracking and particle identification in tpcs and silicon detectors. *Nuclear Instruments and Methods in Physics Research Section A: Accelerators, Spectrometers, Detectors and Associated Equipment*, **562**(1). 154–197 (2006).

[72] STAR detector overview. *Nuclear Instruments and Methods in Physics Research Section A: Accelerators, Spectrometers, Detectors and Associated Equipment*, **499**(23). 624–632 (2003).

[73] The STAR TOF Collaboration. Proposal for a Large Area Time of Flight Sytem for STAR. `https://www.star.bnl.gov/public/tof/`, 2004.

[74] M. Shao, O. Barannikova, X. Dong, Y. Fisyak, L. Ruan, et al. Extensive particle identification with TPC and TOF at the STAR experiment. *Nucl.Instrum.Meth.*, A **558**. 419–429 (2006).

[75] T.M. Cormier, A.I. Pavlinov, M.V. Rykov, V.L. Rykov, and K.E. Shestermanov. STAR Barrel Electromagnetic Calorimeter absolute calibration using 'minimum ionizing particles' from collisions at RHIC. *Nucl.Instrum.Meth.*, A **483**. 734–746 (2002).

[76] STAR Collaboration. SketchUp STAR. `https://drupal.star.bnl.gov/STAR/subsys/bemc`. [online] [20.10.2015].

[77] K. Schweda. A Heavy-flavor tracker for STAR. *Nucl.Phys.*, A **774**. 907–910 (2006).

[78] R. Ma and H. Qiu. Hard Probe Highlights. STAR internal presentation, 2015.

[79] M. Szelezniak. Upgrade of the STAR silicon detectors. Vertex 2014.

[80] STAR Collaboration. MTD plots, pictures and photos. `https://drupal.star.bnl.gov/STAR/subsys/mtd/plots-pictures`. [online] [29.09.2015].

[81] C. Yang, X.J. Huang, C.M. Du, B.C. Huang, Z. Ahammed, et al. Calibration and performance of the STAR Muon Telescope Detector using cosmic rays.

[82] L. Ruan, G. Lin, Z. Xu, K. Asselta, H.F. Chen, et al. Perspectives of a Midrapidity Dimuon Program at RHIC: A Novel and Compact Muon Telescope Detector. *J.Phys.*, G **36**. 095001 (2009).

[83] R. Ma. J/ψ and Υ measurements in the di-muon channel in Au+Au collisions at $\sqrt{s_{NN}}$ =200 GeV with STAR experiment. Quark Matter 2015.

[84] The STAR Collaboration. RHIC Beam Use Request for Runs 16 and 17. `https://drupal.star.bnl.gov/STAR/starnotes/public/sn0625`, 2015.

[85] J. P. Whitfield. Level 0 Simulation Analysis, Introduction. `https://www.star.bnl.gov/public/trg/GeneralTrigger/Simulations/level_0/level0_intro.html`.

[86] W.J. Llope, J. Zhou, T. Nussbaum, G.W. Hoffmann, K. Asselta, et al. The STAR Vertex Position Detector. arXiv 1403.6855 (2014).

[87] A. Denisov C. Adler, H. Strobele E. Garcia, M. J. Murray, and S. N. White. The RHIC Zero Degree Calorimeter. *Nucl. Instrum. Meth.*, A **470**, 488–499 (2001).

[88] F.S. Bieser *et al.* The STAR trigger. *Nuclear Instruments and Methods in Physics Research Section A: Accelerators, Spectrometers, Detectors and Associated Equipment*, **499**(2-3). 766–777 (2003).

[89] C. Yang. Performance of the Muon Telescope Detector (MTD) in STAR at RHIC. Quark Matter 2012.

[90] H. Masui, STAR internal presentation, 2013.

[91] S. Chatrchyan et al. Suppression of non-prompt J/ψ, prompt J/ψ, and Y(1S) in PbPb collisions at $\sqrt{s_{NN}} = 2.76$ TeV. *JHEP*, **05**. 063 (2012).

[92] W. Zha. J/ψ production in Au+Au collisions at $\sqrt{s_{\rm NN}}$ = 39, 62.4 and 200 GeV. STAR Analysis note. 2015.

[93] C. B. Powell. J/ψ Production in Heavy Ion Collisions at the STAR Detector at RHIC. PhD Thesis. 2012.

Appendices

Appendix A

List of public presentations and proceedings

1. The European Physical Society Conference on High Energy Physics, Vienna, Austria, 22 29 July 2015 (poster).

2. The European Physical Society Conference on High Energy Physics, Vienna, Austria, 22 29 July 2015 (proceedings).
   Published in Proceedings of Science: PoS EPS-HEP2015 (2015) 204

3. XXXIV Mazurian Lakes Conference on Physics, Piaski, Poland, 6 13 September 2015 (poster). Content of this poster was the same as in attached poster from The European Physical Society Conference on High Energy Physics.

4. XXXIV Mazurian Lakes Conference on Physics, Piaski, Poland, 6 13 September 2015 (proceedings).
   Published in Acta Physica Polonica B: Acta Phys.Polon. B47 (2016) 997

5. 15th Zimanyi Winter School on Heavy Ion Physics, Budapest, Hungary, 7 - 11 December 2015 (presentation).

J/ψ production in U+U collisions at the STAR experiment

Jana Fodorová for the STAR Collaboration

Faculty of Nuclear Sciences and Physical Engineering

Czech Technical University in Prague

Introduction

Quark-gluon plasma (QGP), a novel state of deconfined nuclear matter, has been studied in high-energy heavy-ion collisions at the Relativistic Heavy Ion Collider (RHIC). Due to the color screening of the quark-antiquark potential in the QGP the production of heavy quarkonia (e.g. J/ψ, Υ) is expected to be supressed. However, there are also other effects that may influence the suppression pattern of heavy quarkonia (e.g. secondary production in the QGP, cold-nuclear-matter effects). To understand those effects we need to study production of heavy quarkonia in various colliding systems. We present preliminary results on nuclear modification factor of J/ψ production reconstructed at midrapidity via di-electron decay channel in minimium-bias U+U collisions at $\sqrt{s_{NN}} = 193$ GeV at the STAR experiment and current status of analysis of J/ψ production in central U+U collisions.

Motivation

- In the most central U+U collisions the energy density of the created medium is expected to be higher than in Au+Au collisions [1].

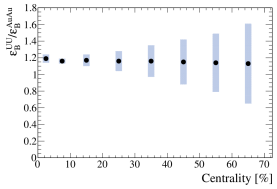

Fig. 1: Estimate of the ratio of energy density in U+U and Au+Au collisions as a function of centrality [1].

- At the STAR experiment, effects of the hot medium on J/ψ production have been studied in Au+Au collisions at $\sqrt{s_{NN}} = 39, 62.4, 200$ GeV and in U+U collisions at $\sqrt{s_{NN}} = 193$ GeV.
- In minimum-bias U+U collisions the nuclear modification factor R_{AA} as a function of p_T is similar to that observed in Au+Au at $\sqrt{s_{NN}} = 200$ GeV.

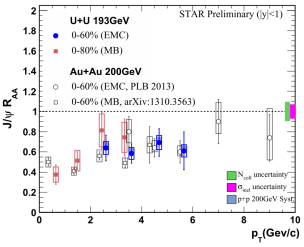

Fig. 2: R_{AA} p_T dependence of J/ψ in minimum bias and high tower triggered Au+Au and U+U collisions [2].

- $0-5$ % most central U+U collisions enable to study the centrality dependence of J/ψ R_{AA}.

STAR Detector

- The Solenoidal Tracker at RHIC (STAR) was designed to investigate the strongly interacting matter by detecting charged particles emerging from collisions.

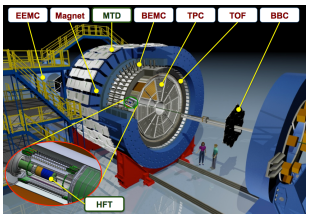

Fig. 3: Layout of the STAR detector.

- STAR excels in tracking and identification of charged particles in midrapidity and 2π in azimuth.
- Most of the subsystems of the experiment are located in 0.5 T of solenoidal magnetic field.
- **Trigger detectors** decide which collisions are suitable for detection and recording.
  - → Centrality triggers: centrality is determined by **Zero Degree Calorimeters** based on measured energy of spectator neutrons combined with multiplicity information from TOF.
- Main subdetectors used for this analysis are:
  - → **Time Projection Chamber** (TPC): main tracking device of STAR, particle identification via their specific energy loss dE/dx.

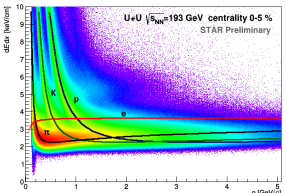

Fig. 4: dE/dx of charged particles.

  - → **Time of Flight** (TOF) detector: $1/\beta$ of the particles, together with TPC: separation of electrons from hadrons up to 1.4 GeV/c.
  - → **Barrel Electromagnetic Calorimeter** (BEMC): electron-hadron separation via p/E at high momentum.

Data analysis in 0-5 % most central U+U collisions

- Data used for this analysis are 115 M of 0-5 % most central U+U collisions at $\sqrt{s_{NN}} = 193$ GeV taken in 2012.
- J/ψ decay electron candidates are selected from good quality tracks satisfying the following criteria:
  - → TPC:
    - $p_T > 1.0$ GeV/c
    - $-1.5 < n\sigma_e < 2.0$
      $n\sigma_e$ is the distance from the expected dE/dx for electrons expressed in terms of standard deviation units
    - required for all particles
  - → TOF:
    - $0.97 < 1/\beta < 1.025$
    - required for $p < 1.4$ GeV/c
    - for $p > 1.4$ GeV/c required only if particle has signal in TOF
  - → BEMC:
    - $E > 0.15$ GeV
      E is energy deposited in the BEMC tower
    - $0.7 < pc/E < 2.0$
    - required for $p > 1.4$ GeV/c

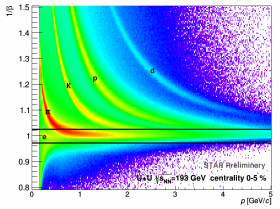

Fig. 5: $1/\beta$ of particles with cut applied on electron candidates (black lines).

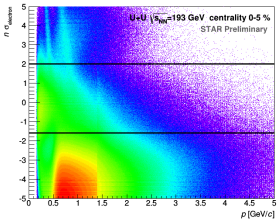

Fig. 6: $n\sigma_e$ of particles satisfying TOF and BEMC cuts, black lines denote $n\sigma_e$ cut.

Results

- J/ψ reconstructed at midrapidity via di-electron decay channel: $J/\psi \rightarrow e^+e^-$ (B.R. 5.9%)
- Combinatorial background reconstructed via the mixed-event background method
- J/ψ yields calculated by the bin counting method in the invariant mass region 2.9-3.2 GeV/c^2
  - → $S = 4960 \pm 580$
  - → significance 8.6 σ
  - → divided into 3 p_T bins

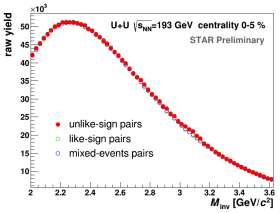

Fig. 7: Invariant mass spectra of unlike-sign, like-sign and mixed-event electron pairs.

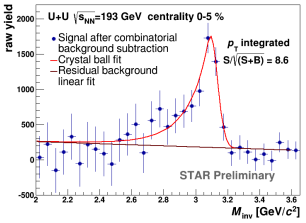

Fig. 8: J/ψ signal for p_T integrated.

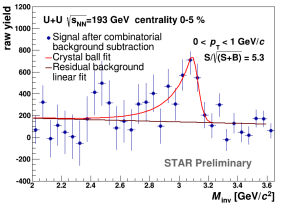

Fig. 9: J/ψ signal with p_T 0-1 GeV/c.

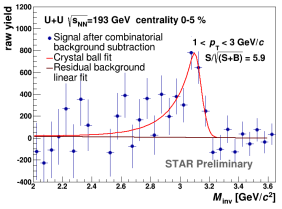

Fig. 10: J/ψ signal with p_T 1-3 GeV/c.

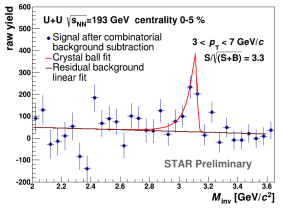

Fig. 11: J/ψ signal with p_T 3-7 GeV/c.

References

[1] D. Kikola et al., Phys.Rev. C84, 054907 (2011).

[2] W. Zha (STAR Collaboration), Nuclear Physics A931, 596-600 (2014).

This work was supported by the grant of the Grant Agency of Czech Republic n.13 – 20841S and by the Grant Agency of the Czech Technical University in Prague, grant No. SGS13/215OHK4/3T/14.

This poster was presented at the European Physical Society Conference on High Energy Physics 2015 in Vienna, Austria.

Conclusions

- Suppression of J/ψ production in minimum-bias U+U collisions at $\sqrt{s_{NN}} = 193$ GeV/c is similar to that observed in $\sqrt{s_{NN}} = 200$ GeV/c Au+Au collisions.
- Significant signal of J/ψ observed in $0-5$% most central U+U collisions. Data analysis to extract R_{AA} is underway.

PROCEEDINGS OF SCIENCE

J/ψ production in U+U collisions at the STAR experiment

Jana Fodorová* **for the STAR Collaboration**
Faculty of Nuclear Sciences and Physical Engineering, Czech Technical University in Prague, Czech Republic
E-mail: fodorjan@fjfi.cvut.cz

Quark-gluon plasma (QGP), a novel state of deconfined nuclear matter, has been studied in high-energy heavy-ion collisions at the Relativistic Heavy Ion Collider (RHIC). Due to the color screening of the quark-antiquark potential in the QGP production of heavy quarkonia (e.g. J/ψ, Υ) is expected to be suppressed. However, there are also other effects that may influence the observed quarkonium yields (e.g. secondary production in the QGP, cold-nuclear-matter effects). To understand those effects we need to study production of heavy quarkonia in various colliding systems. We present preliminary results on nuclear modification factor of J/ψ production at mid-rapidity via the di-electron decay channel in minimum-bias U+U collisions at $\sqrt{s_{\rm NN}} = 193$ GeV at the STAR experiment and the current status of analysis of J/ψ production in central U+U collisions.

The European Physical Society Conference on High Energy Physics
22–29 July 2015
Vienna, Austria

*Speaker.

PoS(EPS-HEP2015)204

1. Introduction

Measurements of heavy quarkonium production in heavy-ion collisions are used to study properties of the QGP. Heavy quarkonium production is expected to be suppressed in the presence of the QGP compared to production in proton+proton (p+p) collisions due to the color screening of the quark-antiquark potential in the deconfined medium. This phenomenon has long been considered as one of the most prominent signatures of the QGP [1].

However, there are other effects that may modify the observed suppression such as cold-nuclear-matter effects, feed down effects, secondary production via coalescence of charm quarks. To understand these different mechanisms it is important to study the heavy quarkonium production in different collisional systems and at different collision energies and centralities.

Modification of heavy quarkonium production in nucleus+nucleus collisions (A+A) compared with p+p collisions is usually quantified by the so-called nuclear modification factor R_{AA}:

$$R_{\mathrm{AA}}(y, p_{\mathrm{T}}) = \frac{1}{< N_{\mathrm{bin}} >} \frac{d^2N_{\mathrm{AA}}/\mathrm{d}p_{\mathrm{T}}\mathrm{d}y}{d^2N_{\mathrm{pp}}/\mathrm{d}p_{\mathrm{T}}\mathrm{d}y}. \tag{1.1}$$

It is defined as the ratio of the number of particles produced in A+A collisions to the number of particles produced in p+p collisions scaled by the average number of binary nucleon-nucleon collisions $< N_{\mathrm{bin}} >$. With no medium effect the yield of heavy quarkonia in heavy-ion collisions should scale with the number of elementary binary collisions and resulting R_{AA} should be equal to unity. As it turns out the medium produced in heavy-ion collisions can modify this scaling resulting in the effect of suppression $R_{\mathrm{AA}} < 1$ or enhancement $R_{\mathrm{AA}} > 1$.

At the STAR experiment, effects of the hot medium on J/ψ production have been studied in Au+Au collisions at $\sqrt{s_{\mathrm{NN}}} = 39,\ 62.4,\ 200$ GeV [2, 3, 4]. STAR has also collected data on U+U collisions at $\sqrt{s_{\mathrm{NN}}} = 193$ GeV. Since U nuclei are larger than Au nuclei, it is expected that in the U+U collisions the energy density of the created medium is higher than in Au+Au collisions [5]. This applies particularly for the most central U+U collisions in which the achievable energy density is expected to be up to $\sim 20\%$ larger relative to Au+Au collisions. Thus they allow for further testing of the color screening hypothesis [5].

2. Data analysis in U+U collisions

The Solenoidal Tracker at RHIC (STAR) [6] is a multi-purpose detector composed of various subsystems. It excels in tracking and identification of charged particles at mid-rapidity and with full coverage in azimuth.

At the STAR experiment, heavy quarkonia have been studied via their di-electron decay channels, e.g. $J/\psi \to e^+e^-$ with a branching ratio $B_{\mathrm{ee}} = 5.9$ %. In the analyses presented here the STAR Time Projection Chamber (TPC) [7], Time of Flight (TOF) [8] detector and Barrel Electromagnetic Calorimeter (BEMC) [9] are used for electron identification. The TPC is the main tracking device of STAR and provides particle identification via their specific energy loss $\mathrm{d}E/\mathrm{d}x$, the TOF detector measures $1/\beta$ of the particles and together with TPC enables separation of electrons from hadrons up to 1.4 GeV/c. The BEMC measures energies of electromagnetic showers produced by high-p_{T} particles and enables electron-hadron separation by pc/E cut, where E is

the energy deposited in the BEMC and p is the momentum of the track. For electron candidates $pc/E \sim 1$ while for hadrons $pc/E > 1$. It is also used to trigger on high-p_T electrons. This is called the High Tower (HT) trigger. Minimum bias (MB) data are triggered by the Vertex Position Detectors (VPD) and the 0-5% central data are triggered by Zero Degree Calorimeters based on measured energy of spectator neutrons combined with track multiplicity information from TOF.

3. R_{AA} in minimum bias U+U collisions

To quantify the hot medium effects on J/ψ production, nuclear modification factor in minimum bias Au+Au and U+U collisions has been measured [2, 3, 4]. Figure 1 (left panel) shows the nuclear modification factor in minimum bias and HT triggered U+U collisions [2]. R_{AA} as a function of p_T is similar to that observed in Au+Au at $\sqrt{s_{NN}} = 200$ GeV [2]. In the right panel of Figure 1 the nuclear modification factor of J/ψ is presented as a function of the number of nucleons participating in collision N_{part}. Results are shown for different colliding energies $\sqrt{s_{NN}} = 200$ (black), 62.4 (red) and 39 (blue points) GeV in Au+Au collisions [2] and for $\sqrt{s_{NN}} = 193$ GeV in minimum bias U+U collisions. U+U data is consistent with Au+Au results with similar N_{part}, within errors.

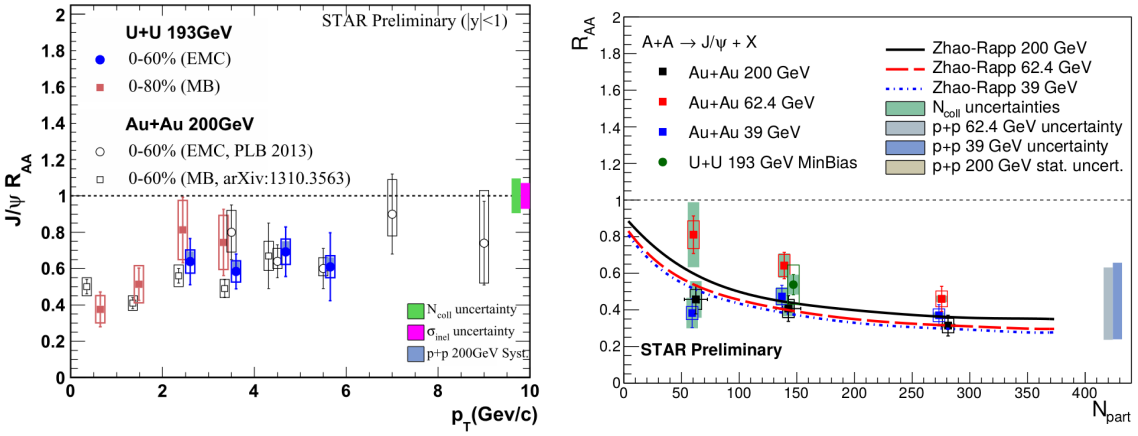

Figure 1: Left:J/ψ R_{AA} as a function of p_T in minimum bias and HT triggered Au+Au and U+U collisions [2]. Right: J/ψ R_{AA} as a function of N_{part} in Au+Au collisions at $\sqrt{s_{NN}} = 200$ (black), 62.4 (red) and 39 (blue points) GeV [2] and compared with model predictions [10] and in minimum bias U+U collisions at $\sqrt{s_{NN}} = 193$ GeV.

4. Analysis status of 0-5% most central U+U collisions

In the analysis presented here 115 M of 0-5% most central U+U collisions collected in 2012 at $\sqrt{s_{NN}} = 193$ GeV were used. J/ψ signal was reconstructed via the di-electron decay channel ($J/\psi \to e^+e^-$). Electron candidates were selected from tracks with transverse momenta $p_T > 1.0$ GeV/c which satisfied selection criteria on TPC, TOF and BEMC signals: $n\sigma_e^{TPC}$, the difference from the expected $ln\ (dE/dx)$ for electrons expressed in terms of standard deviation units, was required to be in the range (-1.5, 2.0) for all electron candidates. For particles with momenta

$p < 1.4$ GeV$/c$ we required $0.970 < 1/\beta^{\mathrm{TOF}} < 1.025$, for $p > 1.4$ GeV$/c$ the energy E deposited in the BEMC tower had to be larger than 0.15 GeV and the ratio pc/E^{BEMC} to be in the range (0.7, 2.0). The cut on $1/\beta^{\mathrm{TOF}}$ for $p > 1.4$ GeV$/c$ was used if particles had a signal in TOF. Figure 2 shows $1/\beta^{\mathrm{TOF}}$ and $n\sigma_{\mathrm{e}}^{\mathrm{TPC}}$ distributions and application of corresponding cuts.

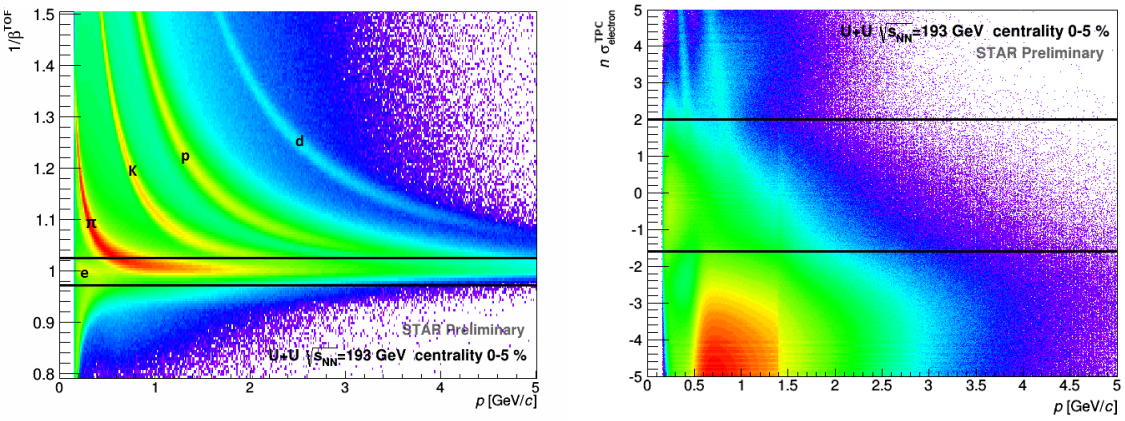

Figure 2: Left: $1/\beta^{\mathrm{TOF}}$ of particles with depicted cut for electron candidates (black lines). Right: $n\sigma_{\mathrm{e}}^{\mathrm{TPC}}$ of particles satisfying TOF and BEMC cuts. Black lines denote the $n\sigma_{e}^{\mathrm{TPC}}$ cut.

Combinatorial background of the J/ψ signal was estimated by the mixed-event background method. Left panel of Figure 3 shows signal before the combinatorial background subtraction. After the combinatorial background subtraction the invariant mass distribution of di-electron pairs was fitted with a crystal ball function to describe the signal while the residual background was fitted with a linear function. The right panel of Figure 3 shows signal after combinatorial background subtraction and fits for the signal and the background. The J/ψ yield calculated by the bin counting method in the invariant mass region (2.9, 3.2) GeV$/c^2$ was 4960 ± 580 with a significance of 8.6 σ.

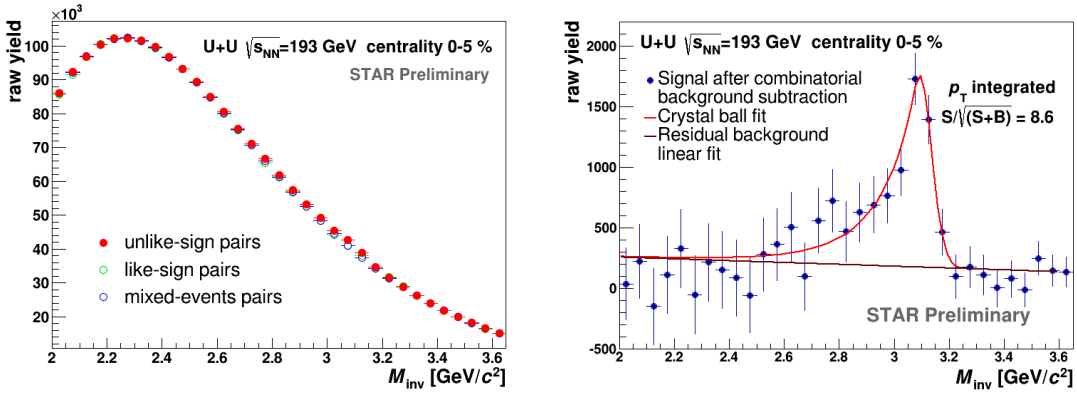

Figure 3: Left: Invariant mass spectra of unlike-sign, like-sign and mixed-event electron pairs. Right: J/ψ signal after combinatorial background subtraction fitted with a crystal ball function together with a linear function used to describe the residual background.

5. Summary

In this work we have presented preliminary results on nuclear modification factor for J/ψ production in minimum-bias U+U collisions at $\sqrt{s_{\rm NN}} = 193$ GeV at the STAR experiment and the current status of J/ψ production analysis in 0-5% most central U+U collisions. Suppression of J/ψ production in minimum-bias U+U collisions is similar to that observed in $\sqrt{s_{NN}} = 200$ GeV Au+Au collisions. In 0-5% most central U+U collisions a strong signal of J/ψ of significance 8.6 σ has been observed.

Data analysis leading to the extraction of J/ψ nuclear modification factor in 0-5% most central U+U collisions is underway. Results of this analysis will extend our knowledge about J/ψ production modification in U+U collisions at the highest achievable energy density at RHIC and enable us to better understand interactions of J/ψ with hot and dense nuclear matter.

Acknowledgments

This work was supported by the grant of the Grant Agency of Czech Republic n.13-20841S and by the Grant Agency of the Czech Technical University in Prague, grant No. SGS 13/215 OHK 4/3 T/14.

References

[1] T. Matsui and H. Satz, *J/ψ Suppression by Quark-Gluon Plasma Formation, Phys.Lett.* **B178** (1986) 416.

[2] **STAR** Collaboration, W.M. Zha, *Recent measurements of quarkonium production in p+p and A+A collisions from the STAR experiment*, *Nuclear Physics* **A931** (2014) 596-600.

[3] **STAR** Collaboration, L. Adamczyk et al., *J/ψ production at low p_T in Au+Au and Cu+Cu collisions at $\sqrt{s_{NN}} = 200$ GeV at STAR, Phys.Rev.* **C90** (2014) 024906, [arXiv:1310.3563].

[4] **STAR** Collaboration, L. Adamczyk et al., *J/ψ production at high transverse momenta in p+p and Au+Au collisions at $\sqrt{s_{NN}} = 200$ GeV, Phys.Lett.* **B722** (2013) 55-62, [arXiv:1208.2736].

[5] D. Kikola, G. Odyniec, and R. Vogt, *Prospects for quarkonia production studies in U+U collisions, Phys.Rev.* **C84** (2011) 054907, [arXiv:1111.4693].

[6] **STAR** Collaboration, K. Ackermann et al., *STAR detector overview, Nucl.Instrum.Meth.* **A499** (2003) 624-632.

[7] M. Anderson, J. Berkovitz, W. Betts, R. Bossingham, F. Bieser, et al., *The Star time projection chamber: A Unique tool for studying high multiplicity events at RHIC, Nucl.Instrum.Meth.* **A499** (2003) 659-678, [nucl-ex/0301015].

[8] **STAR** Collaboration, W. Llope, *Multigap RPCs in the STAR experiment at RHIC, Nucl.Instrum.Meth.* **A661** (2012) 110-113.

[9] **STAR** Collaboration, M. Beddo et al., *The STAR barrel electromagnetic calorimeter, Nucl.Instrum.Meth.* **A499** (2003) 725-739.

[10] X. Zhao and R. Rapp, *Charmonium in Medium: From Correlators to Experiment, Phys.Rev.* **C82** (2010) 064905, [arXiv:1008.5328].

J/ψ PRODUCTION IN U+U COLLISIONS AT THE STAR EXPERIMENT*

Jana Fodorová

for the STAR Collaboration

Faculty of Nuclear Sciences and Physical Engineering
Czech Technical University in Prague, Czech Republic

(Received November 25, 2015)

Quark–gluon plasma (QGP), a novel state of deconfined nuclear matter, has been studied in high-energy heavy-ion collisions at the Relativistic Heavy Ion Collider (RHIC). Due to the color screening of the quark–antiquark potential in the QGP, production of heavy quarkonia (*e.g.* J/ψ, Υ) is expected to be suppressed. However, there are also other effects that may influence the observed quarkonium yields (*e.g.* secondary production in the QGP, cold-nuclear-matter effects). To understand those effects, we need to study production of heavy quarkonia in various colliding systems. We present preliminary results on nuclear modification factor of J/ψ production at mid-rapidity via the di-electron decay channel in minimum bias U+U collisions at $\sqrt{s_{NN}} = 193$ GeV at the STAR experiment and the current status of analysis of J/ψ production in central U+U collisions.

DOI:10.5506/APhysPolB.47.997

1. Introduction

Measurements of heavy quarkonium production in heavy-ion collisions are used to study properties of the QGP. Heavy quarkonium production is expected to be suppressed in the presence of the QGP compared to production in $p + p$ collisions due to the color screening of the quark–antiquark potential in the deconfined medium. This phenomenon has long been considered as one of the most prominent signatures of the QGP [1].

However, there are other effects that may modify the observed suppression such as cold-nuclear-matter effects, feed down effects, secondary production via coalescence of charm quarks. To understand these different

* Presented at the XXXIV Mazurian Lakes Conference on Physics, Piaski, Poland, September 6–13, 2015.

mechanisms it is important to study the heavy quarkonium production in different collision systems and at different collision energies and centralities.

Modification of heavy quarkonium production in nucleus+nucleus collisions ($A + A$) compared with $p + p$ collisions is usually quantified by the so-called nuclear modification factor R_{AA}. It is defined as the ratio of the number of particles produced in $A + A$ collisions to the number of particles produced in $p + p$ collisions scaled by the average number of binary nucleon–nucleon collisions $\langle N_{\text{bin}} \rangle$. With no medium effect, the yield of heavy quarkonia in heavy-ion collisions should scale with the number of elementary binary collisions and the resulting R_{AA} should be equal to unity. As it turns out, the medium produced in heavy-ion collisions can modify this scaling resulting in the effect of suppression $R_{AA} < 1$ or enhancement $R_{AA} > 1$.

At the STAR experiment, effects of the hot medium on J/ψ production have been studied in Au+Au collisions at $\sqrt{s_{NN}} = 39,\ 62.4,\ 200$ GeV [2–4]. STAR has also collected data on U+U collisions at $\sqrt{s_{NN}} = 193$ GeV. Since U nuclei are larger than Au nuclei, it is expected that in the U+U collisions, the energy density of the created medium is higher than in Au+Au collisions [5]. This applies particularly for the most central U+U collisions in which the achievable energy density is expected to be up to $\sim 20\%$ larger relative to Au+Au collisions. Thus, they allow for further testing of the color screening hypothesis [5].

2. Data analysis

The Solenoidal Tracker at RHIC (STAR) [6] is a multi-purpose detector composed of various subsystems. It excels in tracking and identification of charged particles at mid-rapidity and with full coverage in azimuth.

In the analyses presented here, J/ψ was studied in 377 M of minimum bias and 115 M of 0–5% most central U+U collisions collected in 2012 at $\sqrt{s_{NN}} = 193$ GeV at STAR. J/ψ signal was reconstructed via the di-electron decay channel ($J/\psi \to e^+e^-$) with a branching ratio $B_{ee} = 5.9\%$. Electron candidates were selected from tracks which satisfied selection criteria on signals in the STAR Time Projection Chamber (TPC) [7], Time-of-Flight (TOF) [8] detector and Barrel Electromagnetic Calorimeter (BEMC) [9]. The TPC provides particle tracking and identification via their specific energy loss dE/dx. $n\sigma_e^{\text{TPC}}$, the difference from the expected $\ln(dE/dx)$ for electrons expressed in terms of standard deviation units, was required to be in the range of $(-1.5, 2.0)$ for all electron candidates. The TOF detector measures velocity β^{TOF} of the particles and together with TPC enables separation of electrons from hadrons up to 1.4 GeV/c. For particles with momenta lower than stated, we required $0.970 < 1/\beta^{\text{TOF}} < 1.025$. The cut on $1/\beta^{\text{TOF}}$ for $p > 1.4$ GeV/c was used if particles had a signal in TOF.

The BEMC measures energies of high-p_{T} particles. Its fast response allows to trigger on high-p_{T} electrons. This is called the High Tower (HT) trigger. Since electrons are expected to deposit all of their energy in the detector while hadrons not, the BEMC is used for electron–hadron separation by pc/E^{BEMC} cut, where E^{BEMC} is the energy deposited in the BEMC and p is the momentum of the track. For particles with $p > 1.4$ GeV/c, we required $E^{\mathrm{BEMC}} > 0.15$ GeV and $0.5 < pc/E^{\mathrm{BEMC}} < 2.0$ in minimum bias and $0.7 < pc/E^{\mathrm{BEMC}} < 2.0$ in 0–5% most central collisions. Figure 1 shows $1/\beta^{\mathrm{TOF}}$ and $n\sigma_e^{\mathrm{TPC}}$ distributions and application of corresponding cuts in 0–5% most central collisions.

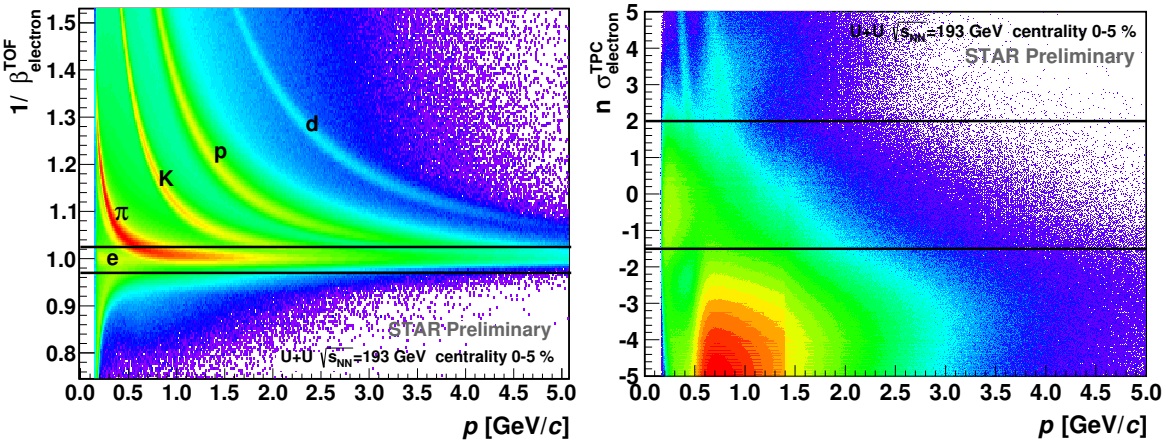

Fig. 1. Left: $1/\beta^{\mathrm{TOF}}$ of particles with depicted cut for electron candidates (black lines). Right: $n\sigma_e^{\mathrm{TPC}}$ of particles satisfying TOF and BEMC cuts, black lines denote the $n\sigma_e^{\mathrm{TPC}}$ cut.

3. Results

J/ψ signal was reconstructed from the invariant mass distributions of the e^+e^- pairs. Combinatorial background of the J/ψ signal was estimated by the like-sign in minimum bias and mixed-event background method in 0–5% central data. After the combinatorial background subtraction, the invariant mass distribution of di-electron pairs was fitted with a crystal ball function to describe the signal, while the residual background was fitted with a linear function. Figure 2 shows J/ψ signal after combinatorial background subtraction and fits for the signal and the background in minimum bias (left panel) and 0–5% central (right panel) U+U collisions. The J/ψ yield calculated by the bin counting method in the invariant mass region (2.9, 3.2) GeV/c^2 was 9440 ± 640 with a significance of 12.9σ in minimum bias and 4960 ± 580 with a significance of 8.6σ in 0–5% central U+U data.

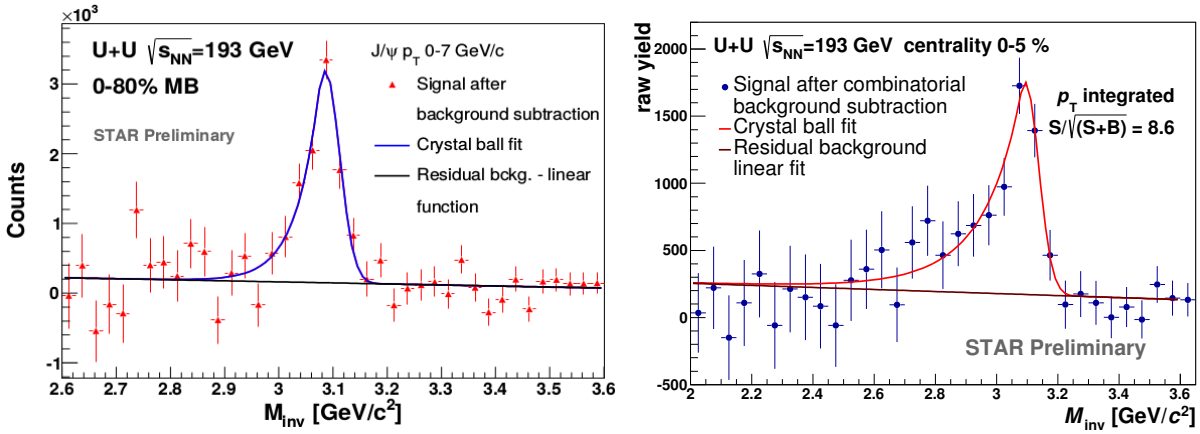

Fig. 2. J/ψ signal after combinatorial background subtraction fitted with a crystal ball function together with a linear function used to describe the residual background in minimum bias (left) and 0–5% central (right) U+U collisions.

Figure 3 (left panel) shows STAR preliminary results on J/ψ invariant yield in minimum bias and HT triggered U+U collisions. To quantify the hot medium effects on J/ψ production, nuclear modification factor in minimum bias Au+Au and U+U collisions has been measured [2–4]. The right panel of figure 3 shows the nuclear modification factor in minimum bias and HT triggered U+U collisions [2]. R_{AA} as a function of p_{T} is similar to that observed in Au+Au at $\sqrt{s_{NN}} = 200$ GeV [2].

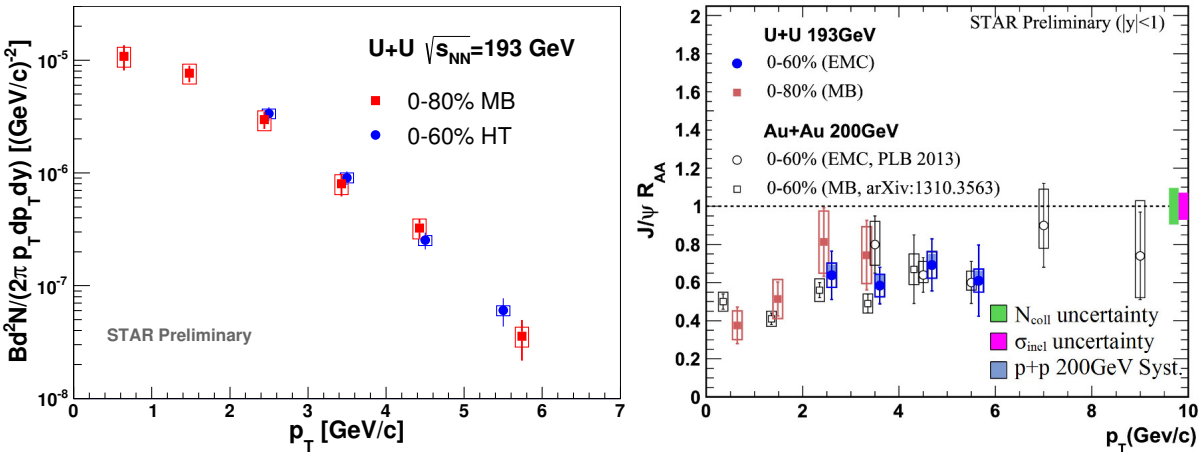

Fig. 3. Left: J/ψ invariant yield *versus* transverse momentum in minimum bias and HT triggered U+U collisions. Right: J/ψ R_{AA} as a function of p_{T} in minimum bias and HT triggered Au+Au and U+U collisions [2].

4. Summary

In this work, we have presented preliminary results on nuclear modification factor for J/ψ production in minimum bias U+U collisions at $\sqrt{s_{NN}} =$ 193 GeV at the STAR experiment and the current status of J/ψ produc-

tion analysis in 0–5% most central U+U collisions. Suppression of J/ψ production in minimum bias U+U collisions is similar to that observed in $\sqrt{s_{NN}} = 200$ GeV Au+Au collisions. In 0–5% most central U+U collisions, a strong signal of J/ψ of significance 8.6σ has been observed.

Data analysis leading to the extraction of J/ψ nuclear modification factor in 0–5% most central U+U collisions is underway. Results of this analysis will extend our knowledge of J/ψ production modification in U+U collisions at the highest achievable energy density at RHIC.

This work was supported by the grant of the Grant Agency of Czech Republic No. 13-20841S and by the Grant Agency of the Czech Technical University in Prague, grant No. SGS 13/215 OHK 4/3 T/14.

REFERENCES

[1] T. Matsui, H. Satz, *Phys. Lett. B* **178**, 416 (1986).

[2] W.M. Zha [STAR Collaboration], *Nucl. Phys. A* **931**, 596 (2014).

[3] L. Adamczyk *et al.* [STAR Collaboration], *Phys. Rev. C* **90**, 024906 (2014) [arXiv:1310.3563 [nucl-ex]].

[4] L. Adamczyk *et al.* [STAR Collaboration], *Phys. Lett. B* **722**, 55 (2013) [arXiv:1208.2736 [nucl-ex]].

[5] D. Kikola, G. Odyniec, R. Vogt, *Phys. Rev. C* **84**, 054907 (2011) [arXiv:1111.4693 [nucl-ex]].

[6] K. Ackermann *et al.* [STAR Collaboration], *Nucl. Instrum. Methods A* **499**, 624 (2003).

[7] M. Anderson *et al.*, *Nucl. Instrum. Methods A* **499**, 659 (2003) [arXiv:nucl-ex/0301015].

[8] W. Llope [STAR Collaboration], *Nucl. Instrum. Methods A* **661**, 110 (2012).

[9] M. Beddo *et al.* [STAR Collaboration], *Nucl. Instrum. Methods A* **499**, 725 (2003).

[10] X. Zhao, R. Rapp, *Phys. Rev. C* **82**, 064905 (2010) [arXiv:1008.5328 [hep-ph]].